Some Advances in Computational Geophysics: Seismic Wave and Inverse Geodynamic Modeling

Thesis by
Dunzhu Li

In Partial Fulfillment of the Requirements for the
degree of
Doctor of Philosophy

CALIFORNIA INSTITUTE OF TECHNOLOGY
Pasadena, California

2016
Defended May 10, 2016

Dunzhu Li
ORCID: 0000-0003-3149-0236

ACKNOWLEDGEMENTS

First and foremost, I would like to thank my advisors. They provided me with chances to work on different projects, a freedom may only be possible in Seismolab. Prof. Rob Clayton is the first faculty I contacted before I came to Caltech. He introduced me to many projects that I have enjoyed, such as using GPU programming for accelerating simulation, and processing a huge amount of data from dense arrays. The skills I gained from these projects are continuing to benefit me. His insight to signals and the ability to make apparently complex procedures simpler helped my research greatly. Prof. Don Helmberger introduced me to seismology. He always has so many new research ideas, more than the figures he asked me to plot, and seismology is full of "low-hanging fruit" for him. Although it turns out that I did not produce "a bunch of papers" as he wished, his passions in research always inspire me. With Prof. Mike Gurnis, I have been working on the adjoint mantle convection inversion. This may be the hardest project I've ever done, because of the uncertainties we face in the method and the results. Mike's intuition and experience in mantle convection, his rigorous pursuit of "realistic" models, along with many practical tricks, make the progress in this project possible. My thanks also go to Prof. Georg Stander at the Courant Institute in NYU. His mathematical insight and enormous experience in PDE constrained optimization helped me solve many hard problems.

I also want to thank Prof. Mark Simons for being on my committee. His experience and insightful comments on the inversion problem helped me understand the limits and further direction of my research. My sincerely gratitude also goes to other faulty members in Seismolab. I learned a lot from their classes and their research.

I am also very grateful to Evelina Cui, Donna Mireles, Rosemary Miller, Viola Carter, Kim Baker-Gatchalian, Priscilla McLean, Julia Zuckerman, Mike Black, Ken Ou, and many other staff in Seismolab, for helping me in many ways.

Seismolab has attracted so many talented students and postdocs, many of whom are now professors. My special thanks go to Risheng Chu and Shengji Wei for teaching me many softwares in seismology at the early stage of my research. I am also very gratitude for the fruitful collaborations with Daoyuan Sun, Fan-Chi Lin, and Zhongwen Zhan, for their amazing scientific interests and insights. My thanks also go to the members in Rob's and Mike's weekly group meeting, whose discussions

and suggestions helped my research a lot.

My thanks also go to the current and previous graduate students in Seismolab, who have made my six years' stay enjoyable. In particular, I want to thank my officemates, Junle Jiang, Vishagan Ratnaswamy, Xiaolin Mao, Minyan Zhong, and Jack Muir, who often are the first people I looked for help. Also I want to thank YoungHee Kim, Francisco Ortega, and Daniel Bower for help on some technique problems in research. I am especially grateful for the help and fun in these years from Ting Chen, Xiangyan Tian, Lingsen Meng, Dongzhou Zhang, Yihe Huang, Yingdi Luo, Semechah Lui, Kangchen Bai, Voon Hui Lai, and many others.

Special thanks to Zhihong Tan and Xi Zhang for their help during my first year at Caltech, to Han Yue for much help and tutoring in workout, to Daiqi Linghu, Yingrui Chang, and Sinan Zhao for help in my job searching, to my former roommate Yiyang Liu, and to members of CaltechC tennis club.

I'm deeply thankful to those people that have helped me find and fulfill two internships, through which I have broadened my horizons. I want to thank Shen Wang and Yunqing Shen for their recommendations, so that I can have the chance of doing a summer intern at ConocoPhillips, a focused three months' research on seismic imaging. My mentor Feng Chen, who is versatile in so many aspects of science and technology, helped me a lot during my internship. I am also very fortunate to have had Yu Zhang as my manager, not only for his worldly known expertise in seismic imaging, but also for his superb skills in presentation which I hope I could have learned more. My second intern at Morgan Stanley was also extremely enjoyable thanks to the guidance and help from managers Chang-Soon Park and Gangqiang Xia, who provided me a lot of opportunities to present my project. My thanks also go to many old and new friends in Houston and New York, for making life outside work a great time during the two summers.

I also want to thank my teachers back in China, especially Prof. Qinghua Huang, Prof. Zengxi Ge, and Prof. Xiaofei Chen for their teachings, and recommendations which led me to Caltech.

My deepest thanks go to my fiancée Yiran Ma, for her love, support, understanding, and guidance in various important moments of my life. I can imagine how miserable my life would be without having met her. Finally, I want to thank and dedicate this thesis to my parents and my late grandparents for their unconditional love.

ABSTRACT

In this thesis I develop computational methods that link theory with geophysical observations, with one part devoted to the development of forward models of seismic wave propagation through the mantle and core and a second part devoted to the inversion of viscous flow in the mantle.

First order seismic structure of the earth has been well described radially since the PREM model was introduced. With the help of seismic tomography methods, many large-scale heterogeneous structures have become well imaged. Based on this progress, the information in seismic waveforms, which provides extra constraints, is becoming more important in determination of the detailed structure within the earth's interior. However, 3-D modeling of seismic wave propagation remains computationally expensive, especially at high frequency, because the computing cost scales with fourth power of frequency. Thus 2-D modeling is often used, and in many cases is sufficient for the problem. To use 2-D modeling in global seismology, several issues need to be considered: how to handle the differences in geometric spreading between 2-D and 3-D modeling, how to incorporate earthquake sources into a 2-D code, and how to handle the spherical geometry of the earth. In the first part of my thesis, we solve all three problems, using a 2-D staggered finite difference method with a post-processing step. The post-processing automatically corrects the geometric spreading difference between 2-D and 3-D wave propagation; the earthquake sources are added to the 2-D finite difference simulation using a momentum source and transparent box approaches; the earth-flattening is discussed, especially for the density transformation. Benchmarks of the new method against with 1-D and 3-D code demonstrates the the accuracy of the method.

We then use the new code in a study of the interface between outer and inner core. Inner Core Boundary (ICB) is thought to be crucial in estimating the energy released in generating the geomagnetic field. One direct constraint on ICB properties is using reflected P wave from ICB, the PKiKP phase. Due to its small amplitude, near distance PKiKP is seldom observed. However, we find several events beneath Central American as having good set of PKiKP recordings from the USArray seismic network, as well as other core phases like P wave reflection with Core Mantle Boundary (CMB). The amplitude of the phases display large scatters across the stations, which are potentially caused by many factors, including site effects of the stations, upper mantle inhomogeneity, or a bumpy structure along either the

CMB or ICB. After comparing amplitude ratio of between PKiKP and PcP phase, analyzing how this ratio changes for different nearby events, and computing forward models using our new method that investigate different factors influence the PKiKP phases, we attribute a stacked amplitude pattern as caused by ICB structure, in which PKiKP phase amplitude rapidly changes within a small range. Finally, we model this observed seismic pattern as a small dome-like anomalies above ICB, where the material changes from that of the outer core to that of inner core gradually.

The final part of my thesis is on a geodynamic inversion problem for mantle convection. Mantle convection is an important process that determines plate motions and subduction. Numerous forward models indicate that the constitute relation (viscosity law) is of key importance for mantle convection. Despite substantial effort attempting to determine the viscosity structure of the mantle, either through forward and inverse geophysical models or through laboratory work, many first order questions remain. We assume the realistic viscosity structure, which is temperature and strain-rate dependent, can be parameterized using a set of scalar parameters. Given this set of viscosity parameters and an initial temperature, the mantle evolves following a set of partial differential equations (PDEs). Our goal with the inverse problem is to recover the viscosity parameters and initial temperature by fitting the observational data, which here includes plate motion history and the present day temperature distribution of the mantle. We formulate this inversion problem following a PDE constrained optimization framework. We first define the cost function we want to minimize; then, the derivative of the cost function with respect to viscosity parameters and initial temperature is calculated following the discrete adjoint equations; finally, a gradient-based optimization method, limited memory Broyden-Fletcher-Goldfarb-Shanno (LBFGS) approach is used to find the minimum. To accelerate the optimization process, we modified the traditional LBFGS by adding a preconditioner, and achieve a more rapid convergence. To test our method, we use two synthetic cases: a sinking cylinder within a viscous layer and a realistic subduction model. We find that in the initial temperature-only inversion, the initial temperature can be recovered well; in the joint inversion of initial temperature and viscosity parameters, the temperature, as well as effective viscosity, can also be recovered reasonably, but there are trade offs between viscosity parameters. Presumably, the trade off in viscosity parameters is related to the ill-posedness of the problem.

PUBLISHED CONTENT AND CONTRIBUTIONS

Li, Dunzhu and Helmberger, Don and Clayton, Robert W and Sun, Daoyuan (2014). "Global synthetic seismograms using a 2-D finite-difference method". In: *Geophysical Journal International*. DOI: 10.1093/gji/ggu050.

Li, Dunzhu and Sun, Daoyuan and Helmberger, Don (2014). "Notes on the variability of reflected inner core phases". In: *Earthquake Science* 27, pp. 441–468. DOI: 10.1007/s11589-014-0093-9.

Lin, Fan-chi and Li, Dunzhu and Clayton, Robert W and Hollis, Dan (2013). "High-resolution 3D shallow crustal structure in Long Beach , California : Application of ambient noise tomography on a dense seismic array". In: *Geophysics* 78.4, Q45–Q56. DOI: 10.1190/geo2012-0453.1.

Ma, Yiran and Clayton, Robert W and Li, Dunzhu (2016). "Higher-mode ambient-noise Rayleigh waves in sedimentary basins". In: *Geophysical Journal International* submitted.

Sun, Daoyuan and Miller, Meghan S and Piana, Nicola and Asimow, Paul D and Li, Dunzhu (2014). "High frequency seismic waves and slab structures beneath Italy". In: *Earth and Planetary Science Letters* 391, pp. 212–223. ISSN: 0012-821X. DOI: 10.1016/j.epsl.2014.01.034.

Zhan, Zhongwen and Helmberger, Donald V and Li, Dunzhu (2014). "Imaging subducted slab structure beneath the Sea of Okhotsk with teleseismic waveforms". In: *Physics of the Earth and Planetary Interiors* 232, pp. 30–35. ISSN: 0031-9201. DOI: 10.1016/j.pepi.2014.03.008.

TABLE OF CONTENTS

LIST OF ILLUSTRATIONS

LIST OF TABLES

Chapter 1

INTRODUCTION

Many important issues including the origin of natural resources, earthquake hazards, and long-term climate change, have their roots in the current structure and evolution of the earth system. Having only access to the top several kilometers of the earth, we have determined many details concerning the earth's distinct past and its deep interior through detective-like work. Geophysicists contribute to this endeavor through studies in seismology, geodesy, mineral physics and geodynamics. Concurrently, a flood of data is being generated from dense networks of seismometers and GPS stations, earth-orbiting satellites, and laboratory experiments on the material properties on earth materials. Interpretation of this flood of data requires ever more complex models, more powerful computers, and more efficient algorithms. My thesis contributes to two aspect of computational geophysics: seismic wave modeling and geodynamic inversion.

Seismic waves, owing to their relatively short wavelength and low attenuation, are the main tools to probe earth's interior structure. They allow for the construction of images of the interior in terms of seismic velocity anomalies and discontinuities. Seismic tomography, initially based on travel time information from seismic ray theory, has greatly advanced our knowledge of the structure of the earth (see e.g., Su and Dziewonski 1991; Grand et al. 1997; Ritsema et al. 2011). However, because of the limitation of ray coverage, and approximation in ray theory, tomographic images may smooth the true anomalies and recover smaller amplitudes of anomalies. Seismic waveform modeling, based on the wave equation, can potentially use more information in a seismogram, such as the amplitude and multipathing of phases, and lead to the discrimination of important attributes, such as a low-velocity zone atop 410km discontinuity (Song et al. 2004) and post-perovskite phase transition near core mantle boundary (Helmberger et al. 2005). Traditionally, 1-D synthetic methods based on analytical or semi-analytical solution of the wave equation, for example, general ray theory (Helmberger and Harkrider 1977) and frequency wavenumber summation (Zhu and Rivera 2002), are often used. As the 1-D seismic structure of the earth has been progressively refined, lateral velocity variation becomes more important, and 1-D synthetics are often no longer suitable. Currently, 3-D synthetics, like those based on the 3-D spectral element method (Komatitsch and Tromp 1999)

and the 3-D finite difference method (Graves 1996), are often used in long period global synthetics and in local ground motion studies. But since the computing cost scales with the fourth power of frequency in 3-D, high frequency synthetics using 3-D methods at a global scale remain a challenge. Thus 2-D synthetics are often used. Moreover, the available data may not be sufficient to constrain a 3-D model. For example, the anomalies in waveforms may appear only on small regions of a network, and may be mainly influenced by velocity structure near the great circle propagation plane from the source to these stations. In such a case, 3-D modeling at a global scale for all stations may be not be a wise use of computational resources.

In the next Chapter, I propose an efficient method to generate global synthetic seismograms, using 2-D code and a post-processing correction step. This work fills the gap between fast 1-D analytic synthetics and time-consuming full 3-D synthetics in global seismic waveform modeling. Because seismic waves have different geometric spreadings between 2-D and 3-D simulations, a correction is required to convert 2-D synthetic seismograms to 3-D synthetics. We proposed a new formulation for the correction, which automatically estimates the horizontal ray parameters of difference phases in the seismogram, and then corrects the phase amplitude based on these horizontal ray parameters. All of the correction is done as a post-processing step of the recorded synthetic seismograms. The new formulation removes the late-time drift appearing in a previous but similar method (Vidale and Helmberger 1987). In order to apply the new method to modeling real earthquakes at global scales, we also discussed how to interface the method with earthquake source descriptions. Many complex source descriptions, like down-going only wave, S only wave, etc., are supported by an extended, transparent box approach to the staggered finite difference grid. Finally, we discussed several issues conscernin the earth-flattening, which converts spherical to Cartesian geometry. The code is implemented using staggered finite difference grids on a graphic processing unit (GPU) architecture, but the method should be applicable to other 2-D methods, like 2-D spectral elements.

In Chapter 3, as a case study of seismic waveform modeling, I present my research on the Inner Core Boundary (ICB). The solidification process at this boundary between liquid outer core and solid inner core strongly influences the geomagnetic field, and is of key importance to the geodynamo. Laboratory experiments indicate that a thin mushy layer forms at the boundary between a fluid and the growing solid, and Shimizu et al. (2005) suggest that such a zone should exist at the ICB

depending on the properties of the light element present. Such a layer is likely to be highly variable given the dynamic circulation involved. Thus, seismologists have been addressing properties of this interface with an array of interesting observations, e.g., Poupinet et al. (1983), Cormier and Choy (1986), Wen and Niu (2002), and Cao et al. (2007). The near distance PKiKP phase, which is the reflection of a P wave off the ICB, provides a direct constraint on ICB properties. Due to its weak amplitude, and coverage limitation of stations, PKiKP at near distances has rarely been observed in the past. We find several recent events beneath Central American which produced excellent sets of PKiKP observations recorded by USArray at high frequency. Other core phases, like PcP (reflection of P wave from core mantle boundary,CMB), phases are also well recorded. We observe that the amplitude of this phase displays considerable scattering across stations, with a factor of 6 or more. Such amplitude variation can potentially be caused by many factors, like site effects of stations, upper mantle inhomogeneity, or a bumpy structure along the CMB or ICB. By considering the amplitude ratio between PKiKP and PcP phase, and how this ratio changes for different nearby events, we are able to isolate an amplitude pattern, which shows a rapid change of PKiKP amplitude within a small range, and attribute this pattern to deep structure, i.e. CMB or ICB. Then through modeling, we find that CMB influence on PKiKP phase is much smaller than that of ICB influence, allowing us to attribute the amplitude pattern to ICB. Finally, using seismic wave modeling, we find this pattern can be explained by small dome-like anomalies above the ICB, where the material changes from that of the outer core to that of inner core gradually.

Seismic images from tomography and waveform modeling give us a snapshot of the present velocity structure of the mantle, for example, the large low velocity provinces and ultra low velocity zones above CMB, the high-velocity anomalies associated with a subducting slab. Such seismic anomalies are used as a constraint on the temperature anomalies, specifically with low velocity province interpreted as as hot, upwelling plumes , the high velocities in subduction zones as cool slabs. But the scaling between seismic anomalies and temperature anomalies is is not perfectly known. A geodynamic model of the mantle, combining seismic observation with other available data, like plate motion history and topography, can potentially give a better understanding of the origin and evolutionary history of these structures.

Computations of mantle convection are now being used to interpret a wide range of phenomena, such as plate motions, rifting, subduction, basin formation, continental

delamination, and sea level change. Forward computational models in particular have become more and more detailed and realistic. In these studies, the constitutive relation (viscosity law) is found to play a first order role in such models. For example, Billen and Hirth (2007) shows the rheological controls on slab dynamics. Despite substantial effort attempting to determine the viscosity structure of the mantle, either through forward or inverse geophysical models or through laboratory work, many first order questions remain. For example, although global geophysical flow models have suggested that the strength of lateral viscosity variations might be small (about an order of magnitude) (e.g. Moucha et al. (2007) and Yang and Michael Gurnis (2016)), global forward (Stadler et al. 2010) and local inverse models (Baumann and Kaus 2015) suggest that the lateral variations in viscosity associated with plate tectonics may be many orders of magnitude ($> 10^3$). In addition, as has been long evident in forward models (Mckenzie et al. 1974; Lenardic 2003) and plate tectonic reconstructions (see review by Seton et al. (2012)), mantle convection is highly time-dependent. This implies that it is essential that we find ways to constrain the time-dependent viscosity structure. Some progress along these lines has been made with global forward models (e.g. Bunge et al. (2009) and Bower et al. (2015)) and inverse models (e.g. Spasojevic et al. (2009) and Moucha and Forte (2011)). Although there has been some attempt to use variable viscosity in such inverse models meant to recover mantle structure in the past (Liu et al. 2008), they have not, arguably, approached realistic variations in viscosity consistent with the dynamics.

To recover the viscosity and initial condition for mantle convection, casting the problem as an inverse is most promising. Such inversions begin by defining a cost function, a function of unknown viscosity parameters and initial temperature, consisting of the misfit between model results and data. Then gradient based optimizing method is used to minimize the cost function. Because of the large number of unknowns, the adjoint method is an efficient way to obtain the gradient cost cost function with respect to unknowns. Bunge et al. (2003) advanced an adjoint method where the viscosity is assumed known, and only initial temperature is to be recovered. Liu and Gurnis (2008) proposed an inversion of both viscosity parameters are initial temperature for models with temperature and velocity dependent viscosity, but its derivation of adjoint equation ignored such dependency, resulting in suboptimal gradient. Worthen et al. (2014) and Ratnaswamy et al. (2015) instead studied instantaneous Stokes flow problem, and recovered viscosity parameters assuming initial temperature is known.

In the last chapter of my thesis, based on these previous studies, we derive and test adjoint inversion for a mantle convection problem where the unknowns include both the initial temperature and scalar viscosity parameters of the mantle. A realistic rheology, which includes both temperature- and strain rate-dependent terms, and yielding, is used. We then derive the discrete gradient of the cost function in a "Discretize then Optimize" fashion. This totally discrete fashion, as opposed to many previous "Optimize then Discretize" approach, allows us to verify the correct implementation of the adjoint equation, and makes full convergence of the inversion possible. In the gradient based inversion, we adopt the limited memory Broyden-Fletcher-Goldfarb-Shanno (LBFGS) approach. We find in this optimizing problem with a field variable for temperatures unknown, a preconditioner to LBFGS is crucial for faster convergence. Using traditional LBFGS, the optimization often fails before the cost function can be reduced substantially. Using proposed preconditioned LBFGS, all inversions explored achieve substantial reduction of cost function.

Finally, we use two synthetic cases, a sinking cylinder and a realistic subduction model, to test our inversion method. The first model can be viewed as a simplified version of the subduction dynamics problem, while the second model is motivated by the evolution off of the west coast of North America, where Farallon-Pacific ridge moved toward the subduction below the continent during the Cenozoic. We find that in the inversion where only initial temperature is unknown, the initial temperature can be recovered well; in the joint inversion of initial temperature and viscosity parameters, the temperature, as well as effective viscosity, can also be recovered reasonably well, but there are trade offs between viscosity parameters. Presumably, the trade off in viscosity parameters is related to the ill-posedness of the problem.

In summary, both lines of my work in this thesis, seismic wave modeling and adjoint geodynamic inversion, are important tools that link geophysical theory with observational data, which in turn leads to a better understanding of the earth system. For the seismic wave modeling, many extensions of the method may have some practical application. For example, the automatic estimation of ray parameter may be used for real seismic recordings; the transparent box may be used for interfacing a coarse grid global simulation with a dense grid local simulation, increasing simulation efficiency. For the adjoint geodynamic inversion, more work is need to extent the method to a global-scale problem. I think a module-like implementation, like those modules in deep learning, will be useful for more seamless implementations, potentially allowing one to try different viscosity laws, different time march scheme,

and different observational data.

References

Baumann, T.S. and Boris J.P. Kaus (2015). "Geodynamic inversion to constrain the non-linear rheology of the lithosphere". In: *Geophysical Journal International* 202.2, pp. 1289–1316. ISSN: 0956-540X. DOI: 10.1093/gji/ggv201 (cit. on p. 4).

Billen, Magali I. and Greg Hirth (2007). "Rheologic controls on slab dynamics". In: *Geochemistry, Geophysics, Geosystems* 8.8, n/a–n/a. ISSN: 15252027. DOI: 10.1029/2007GC001597 (cit. on p. 4).

Bower, Dan J., Michael Gurnis, and Nicolas Flament (2015). "Assimilating lithosphere and slab history in 4-D Earth models". In: *Physics of the Earth and Planetary Interiors* 238, pp. 8–22. ISSN: 00319201. DOI: 10.1016/j.pepi.2014.10.013 (cit. on p. 4).

Bunge, Hans Peter, C. R. Hagelberg, and B. J. Travis (2003). "Mantle circulation models with variational data assimilation: Inferring past mantle flow and structure from plate motion histories and seismic tomography". In: *Geophysical Journal International* 152.2, pp. 280–301. ISSN: 0956540X. DOI: 10.1046/j.1365-246X.2003.01823.x (cit. on p. 4).

Bunge, Hans-peter et al. (2009). "Time Scales and Heterogeneous Structure in Geodynamic Earth Models Time Scales and Heterogeneous Structure in Geodynamic Earth Models". In: *Science* 91.1998, pp. 91–95. ISSN: 00368075. DOI: 10.1126/science.280.5360.91 (cit. on p. 4).

Cao, Aimin, Yder Masson, and Barbara Romanowicz (2007). "Short wavelength topography on the inner-core boundary." In: *Proceedings of the National Academy of Sciences of the United States of America* 104.1, pp. 31–35. ISSN: 0027-8424. DOI: 10.1073/pnas.0609810104 (cit. on p. 3).

Cormier, Vernon F. and George L. Choy (1986). "A search for lateral heterogeneity in the inner core from differential travel times near PKP-D and PKP-C". In: *Geophysical Research Letters* 13.13, pp. 1553–1556 (cit. on p. 3).

Grand, Stephen P., Rob D. van der Hilst, and Sri Widiyantoro (1997). "Global Seismic Tomography: A Snapshot of Convection in the Earth". In: *GSA Today* 7.4, pp. 1–7. ISSN: 10525173. DOI: 10.1130/1052-5173-19.1.40 (cit. on p. 1).

Graves, Robert W (1996). "Simulating seismic wave propagation in 3D elastic media using staggered-grid finite differences". In: *Bulletin of the Seismological Society of America* 86.4, pp. 1091–1106 (cit. on p. 2).

Helmberger, Don and David Harkrider (1977). "Modeling earthquakes with generalized ray theory". In: *Modern problems in elastic wave propagation*. New York: John Wiley & Sons, pp. 479–518 (cit. on p. 1).

Helmberger, D et al. (2005). “Deep mantle structure and the postperovskite phase transition”. In: *Proceedings of the National Academy of Sciences of the United States of America* 102.48, pp. 17257–17263. DOI: DOI10.1073/pnas.0502504102 (cit. on p. 1).

Komatitsch, Dimitri and Jeroen Tromp (1999). “Introduction to the spectral element method for three-dimensional seismic wave propagation”. In: *Geophysical Journal International* 139, pp. 806–822 (cit. on p. 1).

Lenardic, a. (2003). “Longevity and stability of cratonic lithosphere: Insights from numerical simulations of coupled mantle convection and continental tectonics”. In: *Journal of Geophysical Research* 108.B6, pp. 1–15. ISSN: 0148-0227. DOI: 10.1029/2002JB001859 (cit. on p. 4).

Liu, Lijun and Michael Gurnis (2008). “Simultaneous inversion of mantle properties and initial conditions using an adjoint of mantle convection”. In: *Journal of Geophysical Research: Solid Earth* 113.8, pp. 1–17. ISSN: 21699356. DOI: 10.1029/2007JB005594 (cit. on p. 4).

Liu, Lijun, Sonja Spasojevic, and Michael Gurnis (2008). “Reconstructing Farallon plate subduction beneath North America back to the Late Cretaceous.” In: *Science (New York, N.Y.)* 322.5903, pp. 934–938. ISSN: 0036-8075. DOI: 10.1126/science.1162921 (cit. on p. 4).

Mckenzie, D. P., J. M. Roberts, and N. O. Weiss (1974). “Convection in the earth’s mantle: towards a numerical simulation”. In: *Journal of Fluid Mechanics* 62, p. 465. ISSN: 0022-1120. DOI: 10.1017/S0022112074000784 (cit. on p. 4).

Moucha, R and A M Forte (2011). “Changes in African topography driven by mantle convection”. In: *Nature Geoscience* 4.10, pp. 707–712. ISSN: 1752-0894. DOI: 10.1038/ngeo1235 (cit. on p. 4).

Moucha, R. et al. (2007). “Lateral variations in mantle rheology: Implications for convection related surface observables and inferred viscosity models”. In: *Geophysical Journal International* 169.1, pp. 113–135. ISSN: 0956540X. DOI: 10.1111/j.1365-246X.2006.03225.x (cit. on p. 4).

Poupinet, G., R. Pillet, and A. Souriau (1983). “Possible heterogeneity of the Earth’s core deduced from PKIKP travel times”. In: *Nature* 305, pp. 204–206 (cit. on p. 3).

Ratnaswamy, V., G. Stadler, and M. Gurnis (2015). “Adjoint-based estimation of plate coupling in a non-linear mantle flow model: theory and examples”. In: *Geophysical Journal International* 202.2, pp. 768–786. ISSN: 0956-540X. DOI: 10.1093/gji/ggv166 (cit. on p. 4).

Ritsema, J. et al. (2011). “S40RTS: A degree-40 shear-velocity model for the mantle from new Rayleigh wave dispersion, teleseismic traveltime and normal-mode splitting function measurements”. In: *Geophysical Journal International* 184.3, pp. 1223–1236. ISSN: 0956540X. DOI: 10.1111/j.1365-246X.2010.04884.x (cit. on p. 1).

Seton, M. et al. (2012). "Global continental and ocean basin reconstructions since 200Ma". In: *Earth-Science Reviews* 113.3-4, pp. 212–270. ISSN: 00128252. DOI: 10.1016/j.earscirev.2012.03.002 (cit. on p. 4).

Shimizu, H., J.P. Poirier, and J.L. Le Mouël (2005). "On crystallization at the inner core boundary". In: *Physics of the Earth and Planetary Interiors* 151.1-2, pp. 37–51. ISSN: 00319201. DOI: 10.1016/j.pepi.2005.01.001 (cit. on p. 2).

Song, Teh-Ru Alex, Don V Helmberger, and Stephen P. Grand (2004). "Low-velocity zone atop the 410-km seismic discontinuity in the northwestern United States". In: *Nature* 427.6974, pp. 530–533. ISSN: 0028-0836. DOI: 10.1038/nature02231 (cit. on p. 1).

Spasojevic, Sonja, Lijun Liu, and Michael Gurnis (2009). "Adjoint models of mantle convection with seismic, plate motion, and stratigraphic constraints: North America since the Late Cretaceous". In: *Geochemistry, Geophysics, Geosystems* 10.5. ISSN: 15252027. DOI: 10.1029/2008GC002345 (cit. on p. 4).

Stadler, Georg et al. (2010). "The dynamics of plate tectonics and mantle flow: from local to global scales." In: *Science (New York, N.Y.)* 329.5995, pp. 1033–1038. ISSN: 1095-9203. DOI: 10.1126/science.1191223 (cit. on p. 4).

Su, Wei-jia and Adam M Dziewonski (1991). "Predominance of long-wavelength heterogeneity in the mantle". In: *Nature* 352.6331, pp. 121–126. ISSN: 0028-0836. DOI: 10.1038/352121a0 (cit. on p. 1).

Vidale, John E and Donald V Helmberger (1987). "Path effects in strong motion seismology". In: *Seismic strong motion synthetics*. Ed. by Bruce A. Bolt. London: Academic Press Inc (cit. on p. 2).

Wen, Lianxing and Fenglin Niu (2002). "Seismic velocity and attenuation structures in the top of the Earth's inner core". In: *Journal of Geophysical Research* 107.B11, p. 2273. ISSN: 0148-0227. DOI: 10.1029/2001JB000170 (cit. on p. 3).

Worthen, Jennifer et al. (2014). "Towards adjoint-based inversion for rheological parameters in nonlinear viscous mantle flow". In: *Physics of the Earth and Planetary Interiors* 234, pp. 23–34. ISSN: 00319201. DOI: 10.1016/j.pepi.2014.06.006 (cit. on p. 4).

Yang, Ting and Michael Gurnis (2016). "Dynamic topography, gravity and the role of lateral viscosity variations from inversion of global mantle flow". In: *Geophysical Journal International* submitted, pp. 1–51 (cit. on p. 4).

Zhu, Lupei and Luis a. Rivera (2002). "A note on the dynamic and static displacements from a point source in multilayered media". In: *Geophysical Journal International* 148, pp. 619–627. ISSN: 0956540X. DOI: 10.1046/j.1365-246X.2002.01610.x (cit. on p. 1).

Chapter 2

GLOBAL SYNTHETIC SEISMOGRAMS USING A 2D FINITE-DIFFERENCE METHOD

Li, Dunzhu and Helmberger, Don and Clayton, Robert W and Sun, Daoyuan (2014). "Global synthetic seismograms using a 2-D finite-difference method". In: *Geophysical Journal International*. DOI: 10.1093/gji/ggu050.

Two-dimensional (2D) finite-difference synthetics, which fill the gap between fast 1D analytic synthetics and time-consuming full 3D synthetics in our ability to model seismograms, have been used in many studies. We address several issues involving 2D finite-difference methods in generating global synthetic seismograms. These include (1) interfacing point source excitation for earthquakes with 2D finite difference methods; (2) out-of-plane spreading corrections; and (3) reducing the spherical earth to the flattened models. The first issue is tackled using two methods, a "transparent source box" approach and a moment tensor excitation approach, where each has its own advantages. Moreover, our "source box" excitation does not have the late time drift problem that occurred in previous studies. The out-of-plane geometric spreading correction is accounted for by estimating the ray parameter and applying a post-simulation filter to 2D synthetics. Finally, parameters of the earth-flattening transformation are discussed and validated. The effectiveness of this method is demonstrated by comparing our synthetics with frequency-wavenumber summation, normal-mode, and 3D spectral-element synthetics.

2.1 Introduction

Our knowledge of the structure of the Earth has been greatly improved through the development of global seismic tomography. These models are routinely used in global centroid moment tensor (GCMT) solutions (globalCMT.org) and, more recently, in synthetic seismogram predictions, such as the Spectral-Element Method (SEM) (Komatitsch and Tromp 1999; Tromp et al. 2010). Here, as a motivation for our study, we compare how well the tomographic model works for a deep (578km) earthquake beneath the Russian-China border. The geometry is illustrated in Fig. 2.1a with a typical tomographic model shown in Fig. 2.1b. A tangential record section from USArray aligned on the S phase is constructed by stacking the data every 0.8° in dis-

tance, shown in Fig. 2.1c. Synthetic predictions are shown in Fig. 2.2 as downloaded from the Shake Movie website (http://global.shakemovie.princeton.edu). The synthetics have been stacked in the same way as in the data and filtered to the accurate band for synthetics (17 s and longer in this case). When stacked, we can easily detect secondary arrivals that are reflected by the upper mantle discontinuities, as shown in Fig. 2.1c. A comparison of 1D and 3D synthetics indicates that the waveform shapes for most arrivals are similar as shown in Fig. 2.3. In short, 1D synthetics agree with the 3D SEM tomographic model synthetics better than either model fits the data. Thus the tomographic models can be refined by adding waveform modeling.

Synthetic seismograms are the main tools in modeling the complexities in the seismic body waves. In 3D wave simulations, the space-time discretization leads to a scaling of computational cost with the 4th power of seismic frequency, which makes simulations especially challenging for high resolution. Moreover, the available data may not be enough to constrain a 3D model. And sometimes the 2D model assumption, which assumes the elastic parameters are invariant in the direction perpendicular to the great circle propagation plane, is a good approximation for many problems. Thus 2D media assumption is often used in waveform modeling, which later can be checked against the SEM results as in Chen et al. (2007).

To compare synthetics with data, the point dislocation earthquake source and out-of-plane spreading, which are 3D features, need to be considered. There are many existing methods for the so called "2.5D simulation problem", for example, 2D finite difference in Cartesian coordinates (with a correction operator for out-of-plane spreading) (Vidale and Helmberger 1987); 2D pseudospectral method in cylindrical coordinates (with out-of-plane spreading correction) (Furumura et al. 1998; Wang et al. 2001); axisymmetric finite difference (Jahnke et al. 2008); axisymmetric SEM (Nissen-Meyer et al. 2007). The axisymmetric modeling takes into account the out-of-plane spreading automatically, and by coupling P-SV system and SH system, and using Fourier expansion in transverse direction, axisymmetric modeling can also handle non-axisymmetric momentum tensor (Toyokuni and Takenaka 2006). However, if we are interested in a non-axisymmetric model, such as a slab near the source region, axisymmetric methods may not be suitable.

Here, we will focus on the 2D finite-difference (FD) simulation in Cartesian coordinates, a method which has been studied extensively. To interface with an earthquake source in 2D simulation, Vidale and Helmberger (1987) used a source box approach, which was first proposed by Alterman and Karal (1968), but the synthetics have ar-

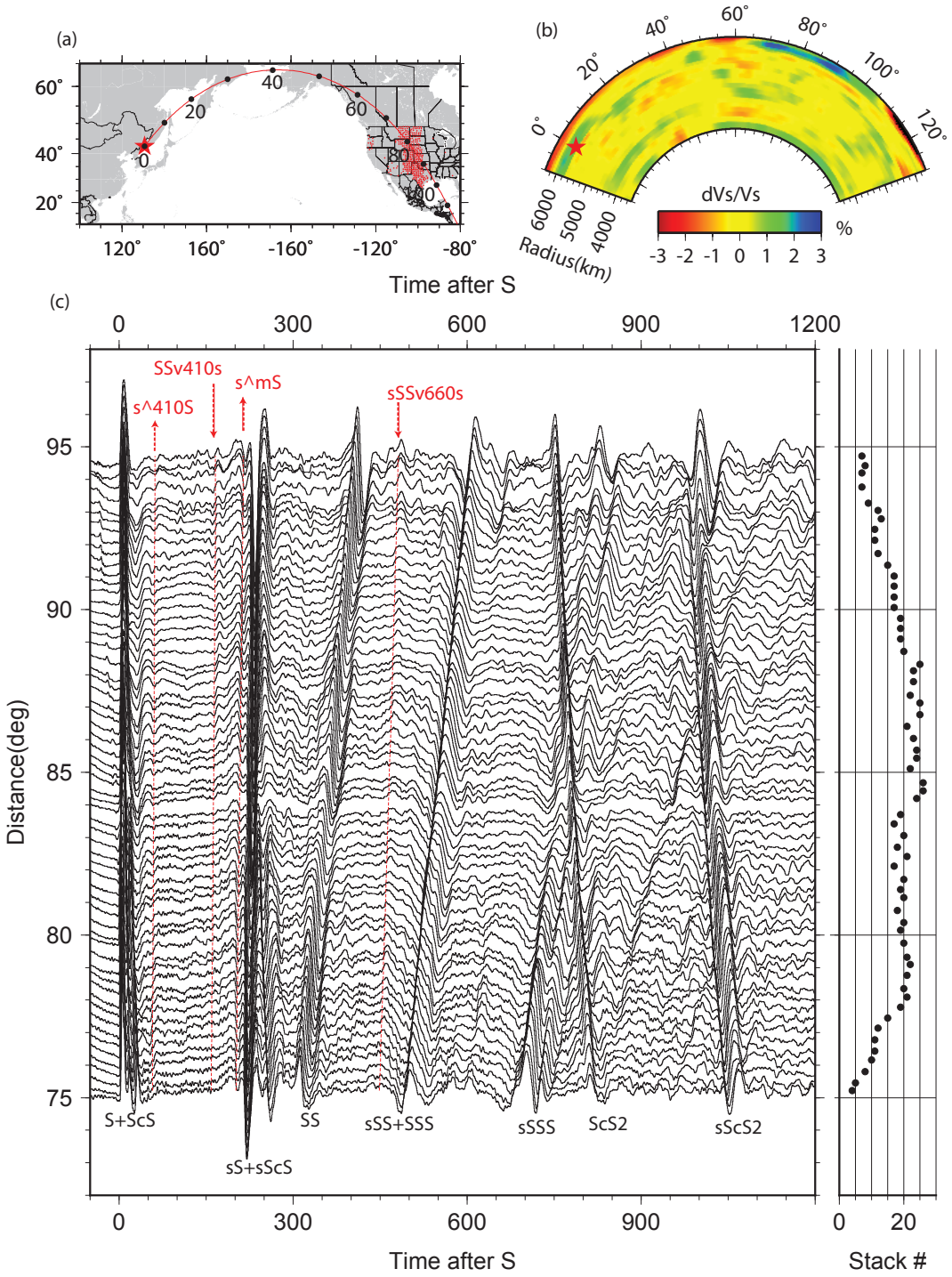

Figure 2.1: A USArray SH stacked record section from a deep earthquake. (a) The 20100218 event (red star) was recorded by the USArray (red dots). The red line indicates one great-arc path (azimuth = 37°) and the numbers indicates the distance in degrees. (b) GyPSuM S-wave tomography model (Simmons et al. 2010) along this path. (c) Stacking of the SH displacement seismogram aligned on the S phase. The bin size is 0.8°with a 0.4 °overlap, and the number of traces with each bin is dotted on the right panel. The main phases are labelled at the bottom. Several clear minor phases interacting with 410 km or 660 km discontinuity are labeled red at the top. Note that s^410S is the precursor of sS phase, and SSv410S is the pegleg of SS phase, following the name convention of Taup Toolkit (Crotwell et al. 1999).

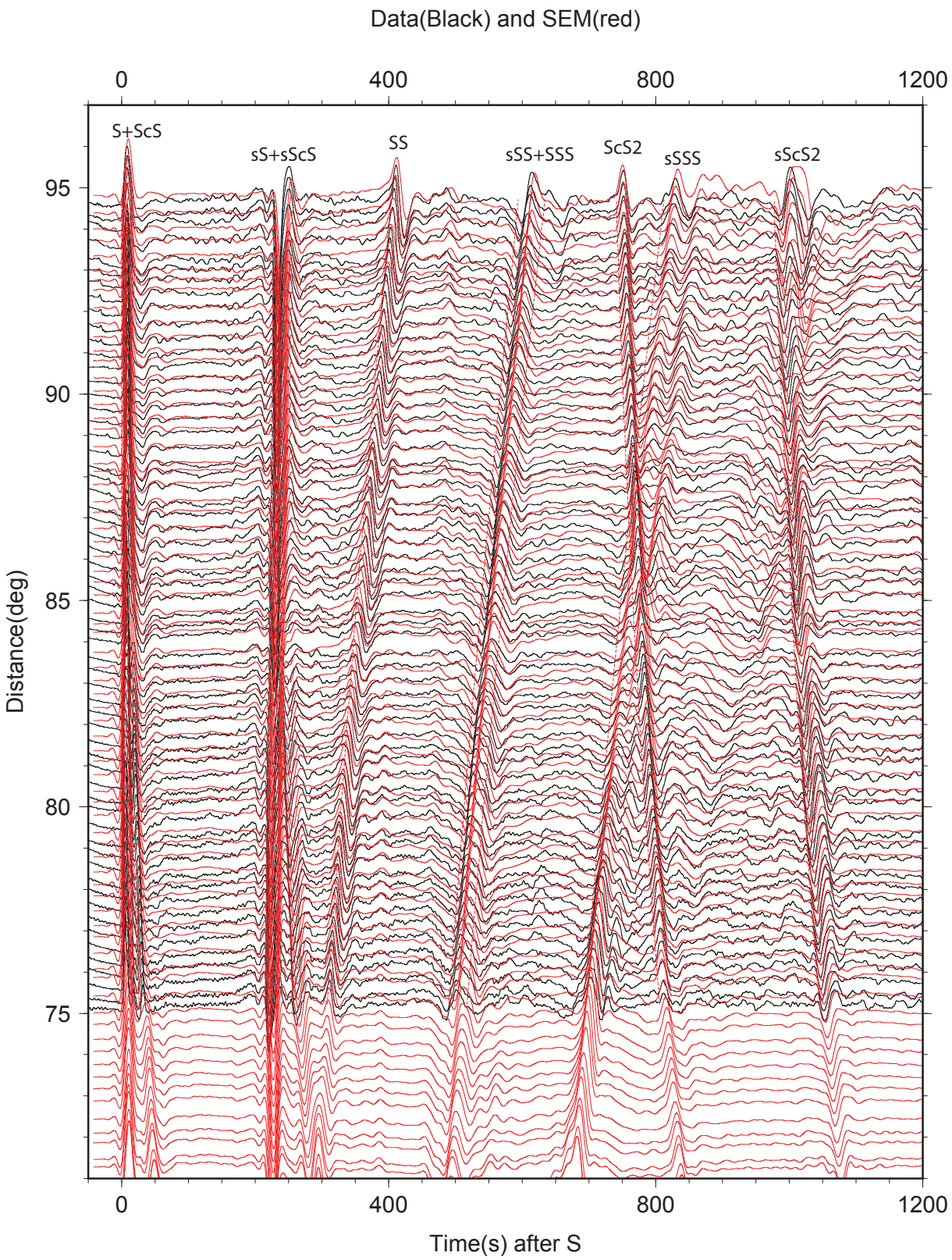

Figure 2.2: Comparison of data (black) and SEM synthetics (red) for the SH displacement. The data is the same as shown in Fig.2.1. The SEM synthetics are stacked the same way as the data.

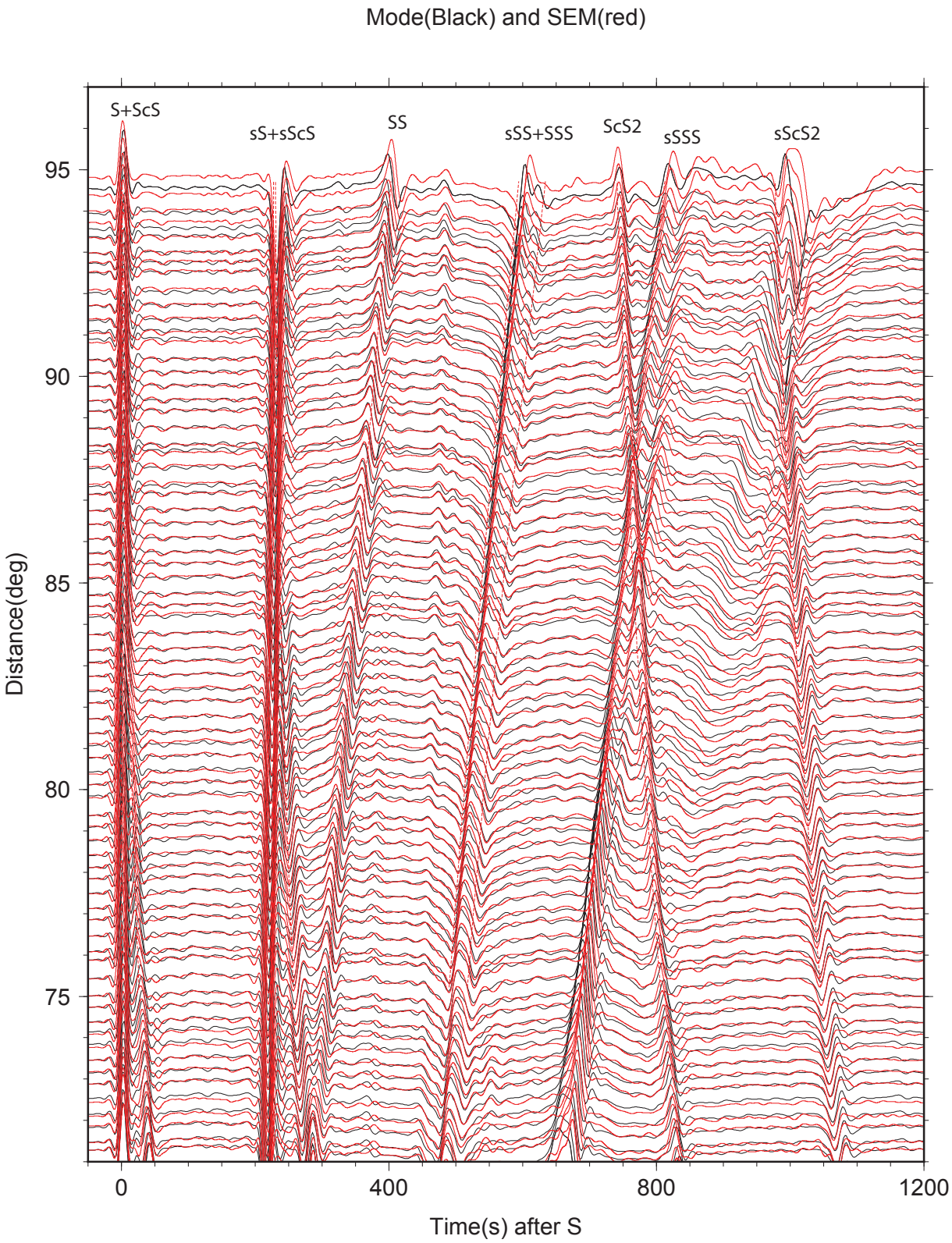

Figure 2.3: Comparison of the 1D mode summation synthetics (black) and the SEM synthetics (red) for the SH displacement. The mode synthetics are stacked the same way as the data.

tificial late-time drifts. Coutant et al. (1995) used a momentum approach, which is not compatible with double-couple solution normally assumed in modeling earthquakes. To address these source excitation issues, we first consider the relationship between 2D and 3D simulations (the out-of-plane spreading). Next we show some improvements and detailed analysis of two source excitation methods.

Our approach involves several approximations with the far field assumption, the out-of-plane spreading correction, and the application of earth-flattening transformation for non-layering spherical media. A comparison of our synthetics with data from the above event is shown in Fig. 2.4. The travel time fits well, but because of the lack of attenuation in our current code, the amplitude and waveform of upper mantle phases (e.g., sSSS) become difficult to compare. However, in many applications, convolving with a t^* operation or changing the sourcetime function can take into account the effective attenuation for a particular phase quite well.

Our goal is not to include all the complexity generally attributed to the earth, but to develop a pragmatic tool in waveform modeling of global bodywave seismograms, in particular some waveform segments. We show that our approach is sufficient for many waveform modeling applications.

2.2 Methods

3D spreading

The relationship between point source and line source seismograms has been discussed in detail in recent textbooks, e.g., Chapman (2004). We will illustrate this using an explosion source in a fluid whole space.

For a point source at the origin, the solution (denoted as V_{3D}) follows the usual form

$$V_{3D}(x, y, z, t) = \frac{1}{R_3}\delta\left(t - R_3/\alpha\right) \tag{2.1}$$

where α is P wave velocity, and $R_3 = \sqrt{x^2 + y^2 + z^2}$ is the source receiver distance, and δ is Dirac delta function.

Following Aki and Richards (1980, p. 226), a line source (along y direction) solution (denoted as V_{2D}) can be obtained by integrating point source solutions along this

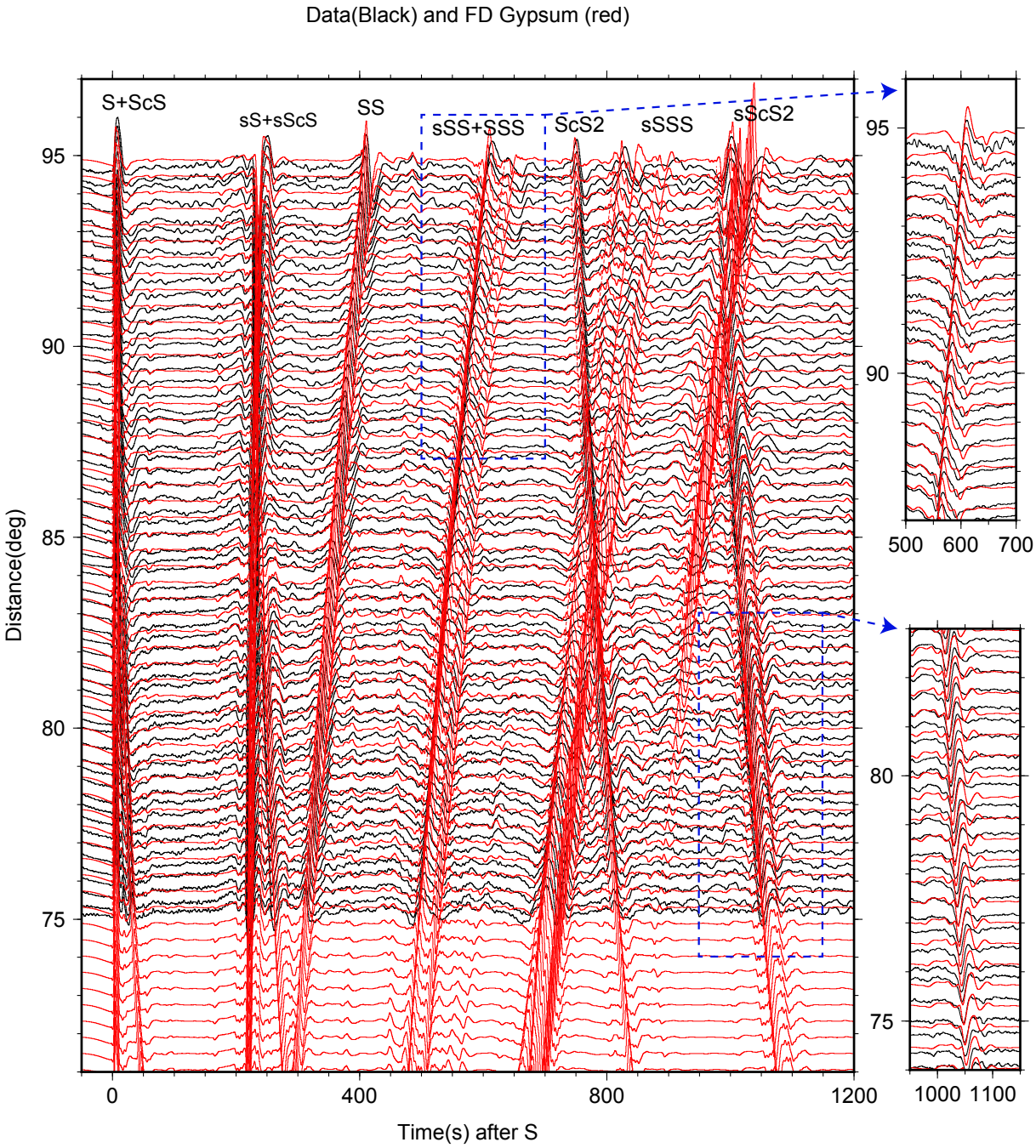

Figure 2.4: Comparison of data (black) and the finite-difference synthetics (red) for the SH displacement. Without of attenuation in the current FD code, the waveform difference is substantial especially for the late phases. To account for attenuation, we apply a t^* of 8s to the FD synthetics (shown in the right two subplots for sSS and sScS2 phases), and obtain better fits with the data.

line

$$\begin{aligned} V_{2D}(x,z,t) &= \int_{-\infty}^{\infty} V_{3D}(x,y,z,t)dy \\ &= \frac{2H\left(t-R/\alpha\right)}{\sqrt{t^2-R^2/\alpha^2}} \\ &= \frac{2H\left(t-R/\alpha\right)}{\sqrt{t+R/\alpha}\sqrt{t-R/\alpha}} \\ &\approx \sqrt{\frac{2\alpha}{R}}\frac{H\left(t-R/\alpha\right)}{\sqrt{t-R/\alpha}} \end{aligned} \tag{2.2}$$

where $R = \sqrt{x^2+z^2}$ is the distance for the two dimensional problem, H is the Heaviside step function, and the last approximation holds because the main contribution to V_{2D} is from the singularity at P arrival time $t = R/\alpha$.

Thus, if we have a line source seismogram, we can obtain point source seismogram at the same position by

$$V_{3D}\left(x,0,z,t\right) = \frac{1}{\pi}\sqrt{\frac{p}{2x}}\frac{d}{dt}\left[\frac{1}{\sqrt{t}} * V_{2D}\left(x,z,t\right)\right] \tag{2.3}$$

where $p = x/R\alpha$ is the geometric ray parameter for the P arrival.

For a general 2D media, a similar result for each individual arrival can be obtained by ray theory (Cerveny 2001)

$$V_{3D}\left(x,0,z,t\right) = \frac{1}{\pi}\sqrt{\frac{1}{2F}}\frac{d}{dt}\left[\frac{1}{\sqrt{t}} * V_{2D}\left(x,z,t\right)\right] \tag{2.4}$$

where the factor $F = \int_{ray} v\ ds$ is an integration of wave traveling velocity v along the ray path ds. In a layered media, Eq. 2.4 reduces to Eq. 2.3 because

$$F = \int_{ray} v\ ds = \int_{ray} \frac{v}{\sin\theta}\ \sin\theta ds = \int_{ray} \frac{1}{p}\ dx = \frac{x}{p} \tag{2.5}$$

where θ is the incident angle, and p is constant along the ray by Snell's law.

But note that on one seismogram, $p = p(t)$ is different for the various seismic phases. Miksat et al. (2008) showed that using ray tracing to calculate the F factor for each phase, line source seismogram can be corrected to obtain the point source seismogram, phase by phase. However, ray tracing is complicated and processing phase by phase is cumbersome. Instead, we assume Eq. 2.5 holds for typical global simulations, with p the ray parameter observed at receiver side. This is a good approximation if the velocity perturbation is small (typical tomographic model), or

the strong heterogeneity is far from receivers and is small in size. Then Eq. 2.3 will hold. We will show that the correction $\sqrt{p(t)}$ in Eq. 2.3 can be constructed automatically without using ray tracing. This allows the correction of a whole seismogram without using different windows for the various arrivals.

To construct $\sqrt{p}$, we first estimate the ray parameter $p(t)$. Because

$$p = \frac{\mathrm{i}k_x}{\mathrm{i}\omega} \tag{2.6}$$

in the frequency (ω) and wavenumber(k_x) domain, where $\mathrm{i} = \sqrt{-1}$, $\mathrm{i}k_x$ corresponds to a differential operator in the x direction, and $1/\mathrm{i}\omega$ corresponds to an integral operator in time, thus operationally

$$p(t)[\ldots] \rightarrow -\frac{d}{dx}\int [\ldots]dt. \tag{2.7}$$

Indeed, applying this to V_{2D} in previous example

$$-\frac{d}{dx}\int \left[\frac{H\,(t - R/\alpha)}{\sqrt{t - R/\alpha}}\right] dt = \frac{x}{R\alpha}\left[\frac{H\,(t - R/\alpha)}{\sqrt{t - R/\alpha}}\right] = p\left[\frac{H\,(t - R/\alpha)}{\sqrt{t - R/\alpha}}\right]. \tag{2.8}$$

Therefore, if we generate the line source seismograms $V_{2D}(x, z, t)$ along a horizontal profile, we can process adjacent traces using Eq. 2.7 to obtain $p(t)V_{2D}(x, z, t)$. Next, by taking the square root of the product of $V_{2D}(x, z, t)$ and $p(t)V_{2D}(x, z, t)$, and paying attention to the sign, we obtain

$$\sqrt{p(t)}V_{2D}(x, z, t) = sgn(V_{2D})\sqrt{|V_{2D} \times p(t)V_{2D}|}. \tag{2.9}$$

By convolving with the remaining part in Eq. 2.3, we can then obtain the point source seismogram at a particular receiver. This procedure works very well when comparing results with other methods as demonstrated in this paper later.

Moment tensor source

In 2D simulation, we can simulate only line sources. We show that by correcting the 3D spreading, we can transfer line source seismograms to point source seismograms. Now we will discuss how a point dislocation source (an earthquake with 3D radiation pattern) is handled in 2D finite difference code. The first method uses the moment tensor approach, which the 3D case is discussed in detail in Graves (1996).

Note that, in global modeling, receivers are distributed at different azimuths. The azimuth variation is thus due to both variation of material properties and earthquake

radiation pattern. The former one can only be accounted for by conducting 2D simulation at each azimuth of interest. Such kind of scaling of computing cost with the number of azimuth is inevitable. However, in the azimuth bins of interest, if we assume material properties do not change with azimuth, then the azimuth variation is purely due to earthquake radiation pattern. This kind of azimuth variation is equivalent to the case where receivers are at one azimuth but earthquake itself changes its strike. Since earthquake moment tensor is combination of several elementary tensors, then by combination of synthetics for these elementary moment tensor, we can account for azimuth variation in the latter case at no extra simulations.

In Cartesian coordinates shown in Fig. 2.5, the earthquake source is at the origin, Z points downwards and X points to receiver azimuth ϕ. All material properties are assumed invariant in Y direction. For a double couple source (strike ϕ_s, rake λ, dip δ), the elementary moment components are (Aki and Richards 1980)

$$\begin{aligned}
M_{xx} &= -(\sin\delta\cos\lambda\sin 2\Phi + \sin 2\delta\sin\lambda\sin^2\Phi),\\
M_{xy} &= \sin\delta\cos\lambda\cos 2\Phi + 1/2\sin 2\delta\sin\lambda\sin 2\Phi,\\
M_{xz} &= -\left(\cos\delta\cos\lambda\cos\Phi + \cos 2\delta\sin\lambda\sin\Phi\right),\\
M_{yy} &= \sin\delta\cos\lambda\sin 2\Phi - \sin 2\delta\sin\lambda\cos^2\Phi,\\
M_{yz} &= -\left(\cos\delta\cos\lambda\sin\Phi - \cos 2\delta\sin\lambda\cos\Phi\right),\\
M_{zz} &= \sin 2\delta\sin\lambda,
\end{aligned} \tag{2.10}$$

where $\Phi = \Phi_s - \phi$ is the effective strike in this coordinate system.

In 2D simulation, we can not simulate all six components, but fortunately we do not need to. The far field radiation for P-SV and SH is after Chapman (2004, p. 123)

$$\begin{aligned}
P(M;\phi_1,\phi_2) &= (M_{xx}\cos^2\phi_1 + M_{yy}\sin^2\phi_1 + M_{xy}\sin 2\phi_1)\sin^2\phi_2,\\
&\quad + M_{zz}\cos^2\phi_2 + (M_{zx}\cos\phi_1 + M_{yz}\sin\phi_1)\sin 2\phi_2,\\
SV(M;\phi_1,\phi_2) &= 1/2\left(M_{xx}\cos^2\phi_1 + M_{yy}\sin^2\phi_1 - M_{zz} + M_{xy}\sin 2\phi_1\right)\sin 2\phi_2,\\
&\quad + \left(M_{zx}\cos\phi_1 + M_{yz}\sin\phi_1\right)\cos 2\phi_2,\\
SH(M;\phi_1,\phi_2) &= (1/2(M_{yy} - M_{xx})\sin 2\phi_1 + M_{xy}\cos 2\phi_1)\sin\phi_2,\\
&\quad + (M_{yz}\cos\phi_1 - M_{zx}\sin\phi_1)\cos\phi_2.
\end{aligned} \tag{2.11}$$

Here ϕ_1, ϕ_2 are the spherical coordinate azimuth angle and inclination angle, re-

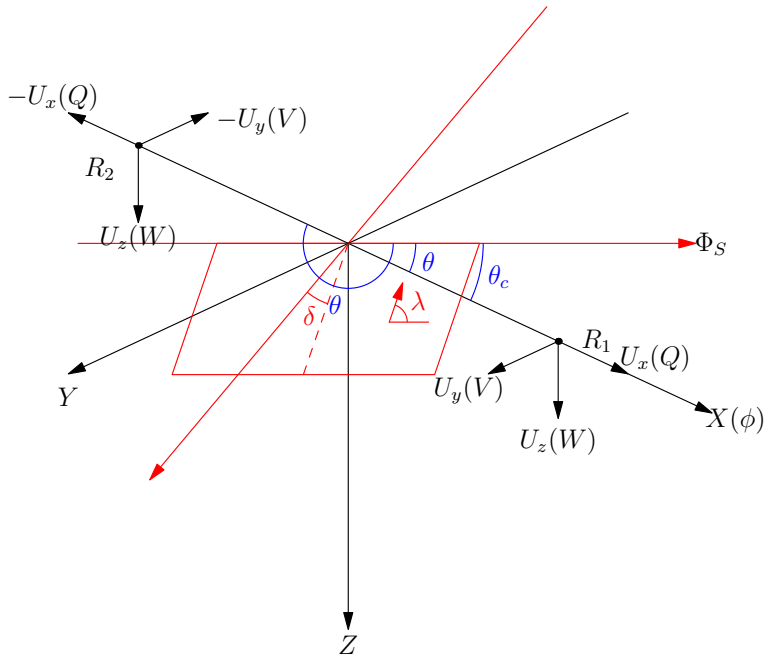

Figure 2.5: Coordinates systems. The dislocation source is at the origin, with the following fault parameters: strike Φ_s, rakeλ, dip δ. The receiver R_1 is at azimuth ϕ, R_2 is at azimuth $\phi + \pi$. In cylindrical coordinate (θ, r, z), θ is the clockwise angle from the strike to the receiver. The direction for SH displacement (V) and P-SV displacement(Q and W) is also shown. In Cartesian coordinate, X points to the receiver direction, Z points downward. The displacement for P-SV is (U_x, U_z), for SH is U_y. Define $\theta_c = \phi - \Phi_s$, the clockwise angle from strike (Φ_s) to positive X direction (ϕ). In the FD source injection, we need to know the displacement in a box surrounding the point dislocation. Note that for the $x \geq 0$ region, $r = x, \theta = \theta_c, U_x = Q, U_y = V, U_z = W$; and for the $x < 0$ region, $r = -x, \theta = \theta_c + \pi, U_x = -Q, U_y = -V, U_z = -W$.

spectively. Thus in the XZ plane we choose, $\phi_1 = 0$, then

$$\begin{aligned} P(M;\phi_2) &= M_{xx}\sin^2\phi_2 + M_{zz}\cos^2\phi_2 + M_{zx}\sin 2\phi_2, \\ SV(M;\phi_2) &= 1/2\,(M_{xx} - M_{zz})\sin 2\phi_2 + M_{zx}\cos 2\phi_2, \\ SH(M;\phi_2) &= M_{xy}\sin\phi_2 + M_{yz}\cos\phi_2. \end{aligned} \tag{2.12}$$

So only M_{xx}, M_{zz}, M_{xz} contribute to the far field PSV system in the XZ plane, and only M_{xy}, M_{yz} contribute to the far field SH system in the XZ plane. And for these components, we can interface them in 2D FD code.

We followed the approach of Coutant et al. (1995) to insert the moment tensors into

the 2D FD code via the velocity-stress formulation of elastodynamics equation

$$\begin{aligned} \rho \frac{\partial \dot{u}_i}{\partial t} &= T_{ij,j}, \\ \frac{\partial T_{ij}}{\partial t} &= c_{ijkl}\dot{u}_{k,l} - \dot{m}_{ij}, \end{aligned} \tag{2.13}$$

where $\dot{u}_i$ is the velocity, T_{ij} the stress, subscript $_{,j}$ differentation, c_{ijkl} the elastic parameter, and m_{ij} seismic moment density. For a point dislocation source $m_{ij} = M_{ij} f(t)\delta(\boldsymbol{x} - \boldsymbol{x}_s)$, where $f(t)$ is the seismic source time function,$\boldsymbol{x}$ is 2D spatial coordinate, and $\boldsymbol{x}_s$ is the source location . In the finite difference simulation, $\delta(\boldsymbol{x} - \boldsymbol{x}_s)$ is replaced by $1/(\Delta h)^2$, an average over the grid cell, where Δh is the finite difference grid size. Then at every time step, the source injection is done by updating the stress components at the source grid points

$$T_{ij} \leftarrow T_{ij} - \Delta t M_{ij} \dot{f}(t)/(\Delta h)^2 \tag{2.14}$$

Transparent source box

The momentum approach is simple and compact in space. However, a classic approach discussed in this section has the advantage of modeling some complex sources.

Here, we follow the transparent box approach used by Alterman and Karal (1968) and Vidale et al. (1985) to add the source into the FD. This procedure becomes more complicated in staggered grid FD. The basic idea is to divide the elastic wavefield A into two parts, one of which is the known analytical source part S, and the other is the unknown part R that accounts for interactions with the structure, so $A = S + R$. Conceptually we will conduct two FD simulations. One is within the source region and only updates R, the other is outside the source box and updates A. The two simulations exchange information through the boundary.

In Fig. 2.6, the FD grids are divided into four parts, where part (1)(2) is the region where we update A, and part (3)(4) is the region where we update R.

In the first FD simulation that updates A, we need to know A at part (3) as a boundary condition. In part (3) we only know R from the second FD simulation at previous time step, but we can use $A = R + S$ to obtain A at region (3), provided that we can calculate S analytically. Similarly, in the second FD simulation that updates R, we need R in part (2) as a boundary condition. We only know A in part (2) from the first simulation at previous time step, but we can obtain R from $R = A - S$.

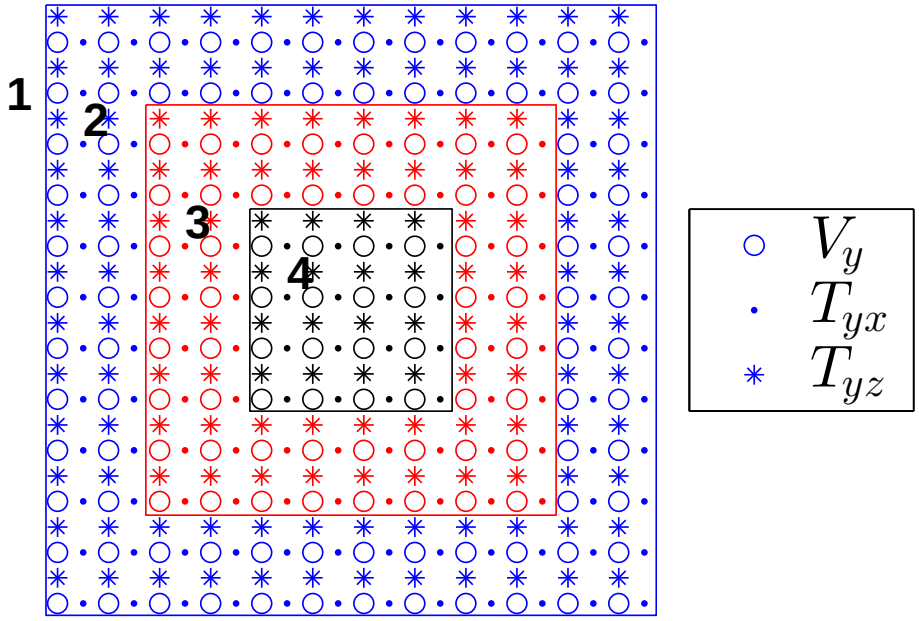

Figure 2.6: The source box for a staggered-grid finite difference for the SH case. Part (1)(2) is the region for updating A. Part (3)(4) is the region for updating R. We need to compute source wavefield S analytically at part (2)(3). Note that as a boundary condition for simulation of R in (3), the width of part (2) should be larger enough to accommodate the width of FD stencil centered on part (3). Similarly, width of part (3) should be larger enough to accommodate the width of FD stencil centered on part (2). Here, the finite difference stencil width is 4 grid points (two points on each side), so we choose width of region (2) and (3) to be 2 grid points. There is no limit on how large part (4) can be, as long as it's large enough to accommodate the width of FD stencil in part (3).

In detail, for either PSV or SH system, one FD step for updating stress T and velocity V requires:

1. $V_A^n = V_R^n + V_S^n$ in region (3)
2. $(T_A^{n-1/2}, V_A^n) \rightarrow T_A^{n+1/2}$ in regions (1) and (2)
3. $V_R^n = V_A^n - V_S^n$ in region (2)
4. $(T_R^{n-1/2}, V_R^n) \rightarrow T_R^{n+1/2}$ in regions (3) and (4)
5. $T_A^{n+1/2} = T_R^{n+1/2} + T_S^{n+1/2}$ in region (3)
6. $(V_A^n, T_A^{n+1/2}) \rightarrow V_A^{n+1}$ in regions (1) and (2)
7. $T_R^{n+1/2} = T_A^{n+1/2} - T_S^{n+1/2}$ in region (2)

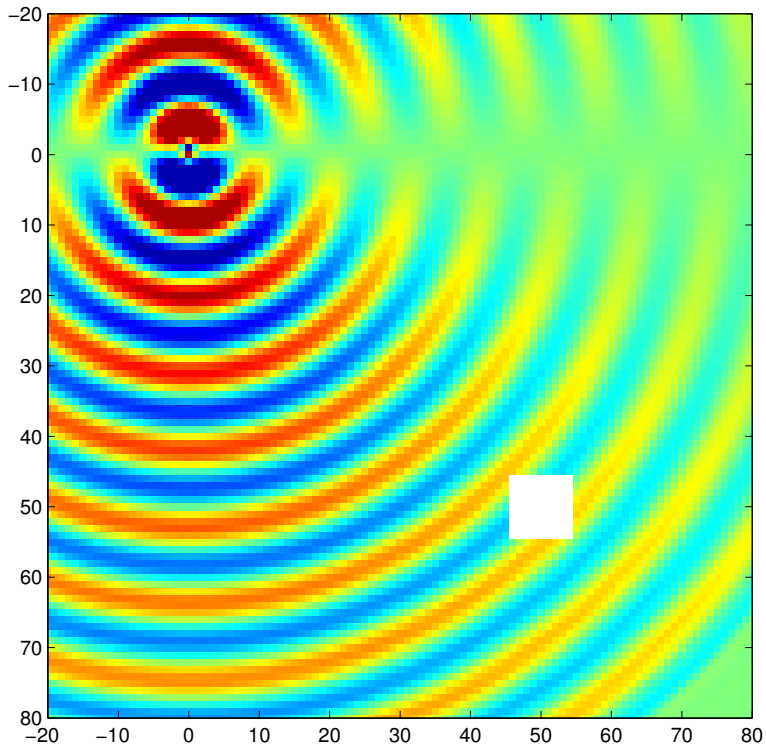

Figure 2.7: The wavefields radiated from a monotone source outside of the box (white region). Although there is no explicit updating of the total wavefield inside the box, the wavefield passes the box smoothly as if it does not exist.

8. $(V_R^n, T_R^{n+1/2}) \rightarrow V_R^{n+1}$ in regions (3) and (4)

This approach allows the scattered wavefields to pass the source box as if the box does not exist, which is termed "transparent source box" (Aki and Richards 1980), see Fig. 2.7.

Vidale et al. (1985) and Helmberger and Vidale (1988) proposed an approach widely used to interface the 2D FD method with Cagniard-de Hoop source description that accounts for the 3D earthquake radiation pattern. But their approach produces a late-time drift, which obscures late arrivals like surface waves. To understand the cause of drift, we take a point dislocation source (pure strike-slip) in homogeneous media as an example. In their approach, using cylindrical coordinates (Fig. 2.5), the vertical displacement at position (θ, r, z) in homogeneous media will be (see Appendix for details)

$$W = W_\alpha + W_\beta, \tag{2.15}$$

where α, β denote the P and S contribution respectively. In detail

$$\begin{aligned} W_\alpha &= \frac{M_0}{4\pi\rho}\frac{2}{\pi}A(\theta,\lambda,\delta)\frac{d}{dt}\left[\frac{1}{\sqrt{2r}}\frac{1}{\sqrt{t}} * Im\left[(-p^2)\frac{\sqrt{p}}{\eta_\alpha}(-\varepsilon\eta_\alpha)\frac{dp}{dt}\right]\right], \\ W_\beta &= \frac{M_0}{4\pi\rho}\frac{2}{\pi}A(\theta,\lambda,\delta)\frac{d}{dt}\left[\frac{1}{\sqrt{2r}}\frac{1}{\sqrt{t}} * Im\left[(-\varepsilon p\eta_\beta)\frac{\sqrt{p}}{\eta_\beta}(p)\frac{dp}{dt}\right]\right], \end{aligned} \tag{2.16}$$

where M_0 is the seismic moment, ρ is the density, r is the horizontal distance between source and receiver, ε is the sign of Z coordinate of the receiver, $A(\theta,\lambda,\delta)$ is a function depending on earthquake focal mechanism (strike assumed at 0, rake λ, dip δ) and azimuth of the receiver θ, and

$$\begin{aligned} p &= \frac{r}{R^2}t + \mathrm{i}\left(t^2 - \frac{R^2}{v^2}\right)^{1/2}\frac{|z|}{R^2} \\ \eta_v &= \frac{|z|}{R^2}t - \mathrm{i}\left(t^2 - \frac{R^2}{v^2}\right)^{1/2}\frac{r}{R^2}, \quad v = \alpha, \beta \end{aligned} \tag{2.17}$$

with $\mathrm{i} = \sqrt{-1}$.

Because of the singularity at $t = R/v$ for the term

$$\frac{1}{\eta}\frac{dp}{dt} = \frac{\mathrm{i}}{(t^2 - R^2/v^2)^{1/2}} \tag{2.18}$$

the most contribution comes from the time when phase first arrives. Eq. 2.17 then becomes $p \approx r/Rv = p_0$, and thus the term in Eq. 2.16 can be simplified

$$Im\left[\sqrt{p}(\cdots)\frac{1}{\eta}\frac{dp}{dt}\right] \approx Im\left[\sqrt{p_0}(\cdots)\frac{1}{\eta}\frac{dp}{dt}\right] = \sqrt{p_0}Im\left[(\cdots)\frac{1}{\eta}\frac{dp}{dt}\right] = \sqrt{p_0(t)}W_{2D}. \tag{2.19}$$

Then it can be verified that the W_{2D} part is indeed a line source solution and satisfies the 2D wave equation. Thus it can be interfaced with 2D FD to propagate to further distance from the source. Note p_0 (the geometric ray parameter) is the same as p in Eq. 2.3.

The above $W_{2D} = W_{2D,\alpha} + W_{2D,\beta}$ consists of the P and S part, respectively. It can be shown that $W_{2D,\alpha}$ and $W_{2D,\beta}$ each individually goes into infinity as $t \to \infty$, but their summation W_{2D} does not. For example, wavefield snapshots of W_{2D}, $W_{2D,\alpha}$, and $W_{2D,\beta}$ generated using the "transparent box approach" are shown in Fig. 2.8abc respectively. Note that the drift terms appear around source box in Fig. 2.8bc, but they are of opposite sign and are cancelled as shown in Fig. 2.8a.

In Vidale and Helmberger (1987), however, the authors approximated $\sqrt{p_0(t)/r}$ using $\sqrt{1/R\alpha}$ for W_α part, and $\sqrt{1/R\beta}$ for W_β part. They then interfaced 2D FD

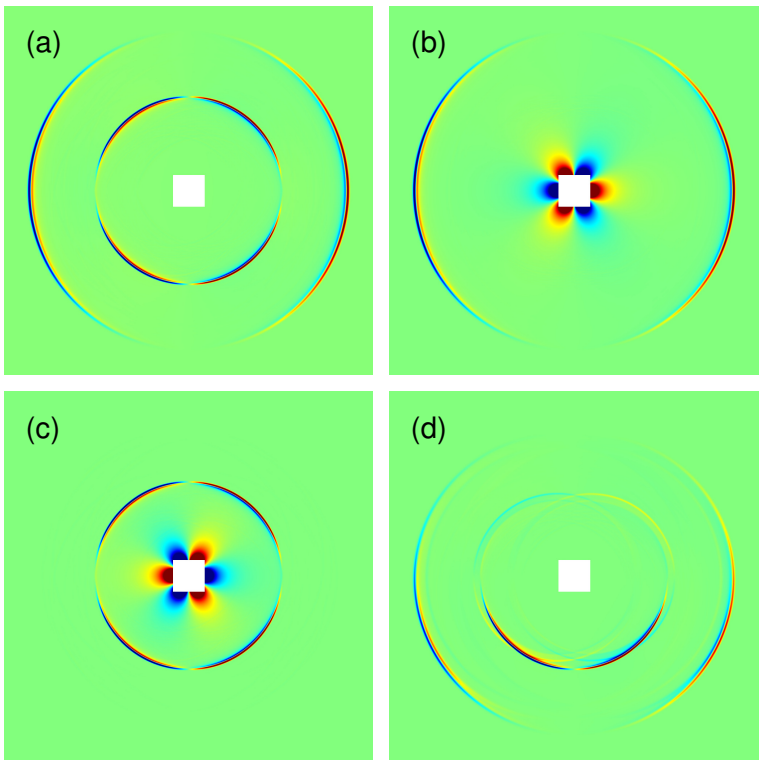

Figure 2.8: Demonstration of box sources for: (a) a dislocation source; (b) its P wave component; (c) its S wave component; (d) its downgoing component. The white box is the source region. Note that the P and S components seperately are unstable, but their sum (a) is stable.

with a source $W^*_{2D} = \sqrt{1/\alpha} W_{2D,\alpha} + \sqrt{1/\beta} W_{2D,\beta}$. In this way, the drifting term will not be cancelled, and $W^*_{2D} \to \infty$ as $t \to \infty$. The seismograms generated using the original formulation (old source) and the new one are compared in Fig. 2.9. Although the drift is of low frequency and can be mitigated using a high-pass filter, it becomes large in amplitude at late-time, and contaminates the late arrivals, making it difficult to use in global modeling. The new source approach does not have this problem.

The source box approach has the advantage that it can be used to represent some complex sources. For example, in Fig. 2.8bc, we show that we can interface with only the P part or the S part of the wavefield. Note that the seperate P and S part each individually has the correct radiation pattern, which is hard to obtain using the moment tensor approach. We can also simulate only the downgoing wavefield by nullifying the wavefield in the upper half of the source box, as shown in Fig. 2.8d. Although the separation of downgoing part is not perfect, such flexibility proves useful in some studies, such as studies involving directivity (Saikia and Helmberger

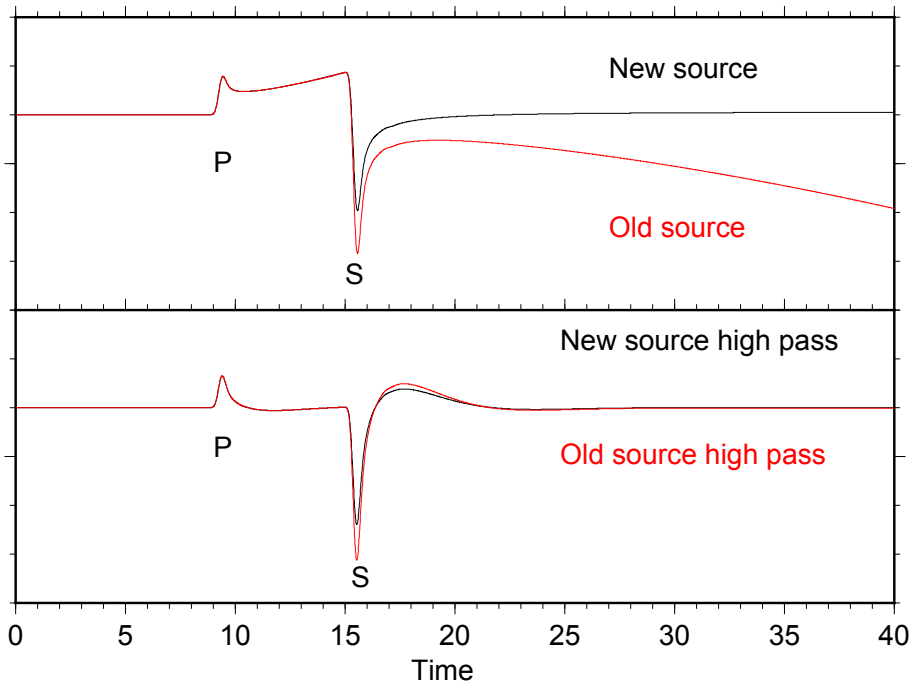

Figure 2.9: The old source box has the low-frequency late-time drift and can be mitigated using a high pass filter. The new source box does not have the drift. Note that the S phase amplitude of the old source is bigger because of an extra $\sqrt{\alpha/\beta}$ factor compared with that of the new source.

1997), and the identification of depth phases.

While the above 2D approaches are equivalent to an asymptotic double-couple solution (the so-called far-field solution), they may break down at very long periods, which proves useful as demonstrated below.

Earth Flattening Transform

Since global models are sensitive to the earth's curvature, in Cartesian coordinate simulation, the treatment of earth flattening becomes essential. A particularly simple transformation was proposed by Müller (1971),

$$\begin{aligned} z &= a \log \frac{a}{r}, \\ \alpha_f &= \alpha_s \frac{a}{r}, \\ \beta_f &= \beta_s \frac{a}{r}, \end{aligned} \tag{2.20}$$

where z,α_f, β_f are the depth and velocities in the flat model, r, α_s, β_s are the radius and velocities in the spherical model, and a is the radius of the earth. This earth flattening transform gives the correct kinetics of wave propagation for a layered

earth. To obtain the correct amplitude, we also need a transform for density, which usually takes the following form

$$\rho_f(z) = \rho_s \left(\frac{r}{a}\right)^{m+2}, \tag{2.21}$$

where m is to be determined.

For an SH system in layered media, Biswas and Knopoff (1970) show that an exact earth flattening transformation is achieved by setting $m = 3$. However, an exact earth flattening transformation does not exist for the P-SV system, and m from -3 to 3 have been considered (Chapman 1973). A $m = -3$ appears to be optimal in a layered fluid, which has the same transformation of density as that used for velocities (Helmberger 1973). Another commonly used value is $m = -2$, which keeps $\rho_f(z) = \rho_s(r)$ (Müller 1971).

Given the same seismic moment in Cartesian code, the absolute amplitude of the body wave increases as m increases (which means a decrease in ρ_f). Our numerical tests show that, at distance of 90°, a unit increase of m value results in an increase of 5% in the P wave amplitude. But as shown in Fig. 2.10a, the relative amplitude and waveform complexity of body wave changes little as we change m, and the largest differences between the results are in the fundamental Rayleigh wave phase. The fundamental Rayleigh wave has a very long-period and is sensitive to earth's curvature and density (Dahlen and Tromp 1998). A search for the appropriate m value shows that $m = 0$ fits the Rayleigh wave better than other integer m, although at these periods self-gravitation, and the Earth's rotation become important issues, and because these are already embedded in the SEM, it is the preferred method at these periods.

As discussed in Gilbert and Helmberger (1972), transferring the synthetics from flattened earth model to spherical earth model needs another amplitude correction

$$U^{(s)} \approx \sqrt{\Delta / \sin \Delta} U^{(f)}, \tag{2.22}$$

where Δ is the epicentral distance in degrees.

The above earth flattening transform is for a 1D spherical earth. For a lateral varying tomographic model, we apply earth flattening transform to each vertical profile, as in many previous studies. A demonstration of the transformation with several ray paths is shown in Fig. 2.11; see Helmberger (1973) for details.

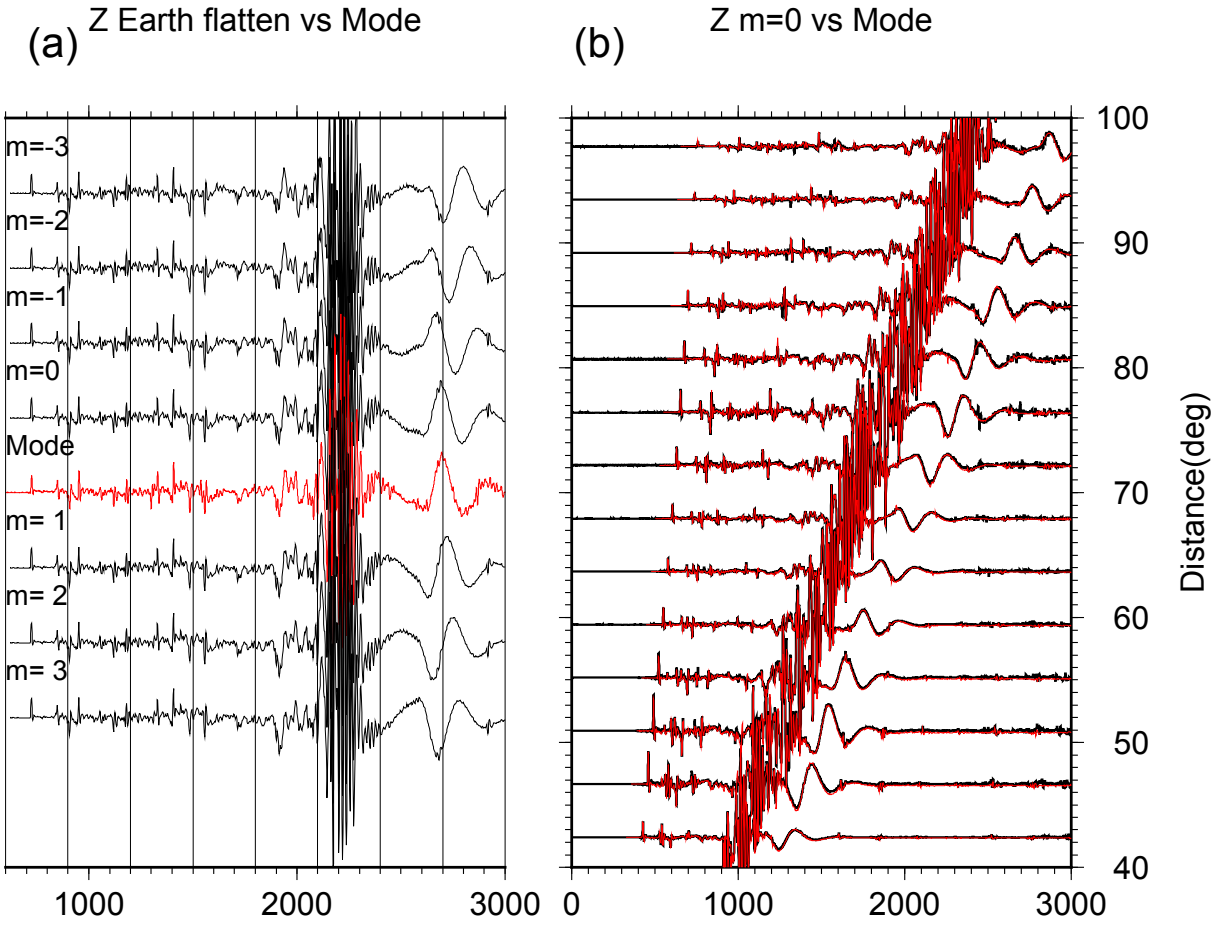

Figure 2.10: (a) Comparison of vertical displacement seismograms at $90°$ for the PREM using different m with mode summation synthetics. It appears that $m = 0$ best fits the fundamental Rayleigh around 2700s in these cases. (b) m=0 synthetics (red) fits mode summation Rayleigh wave(black) at other distances as well.

FD implementation

Finite difference methods in seismology have been discussed by many authors. In our implementation, we use the staggered grid velocity-stress scheme (Virieux 1984; Levander 1988), which can account for solid-fluid interface automatically. For the SH system, the free surface is implemented using stress imaging method; for PSV system, we use the method in Mittet (2002). For absorbing boundary condition, we use the parameter in Zhang and Shen (2010). The code is written using CUDA (Micikevicius 2009) and parallelized using pthread on three GPUs within one computing node, which for our 2D case has a speedup around 100 compared with a single CPU.

To reduce spatial dispersion caused by discretization, we use 8th order central difference in space. Second order central difference is used for time discretization in

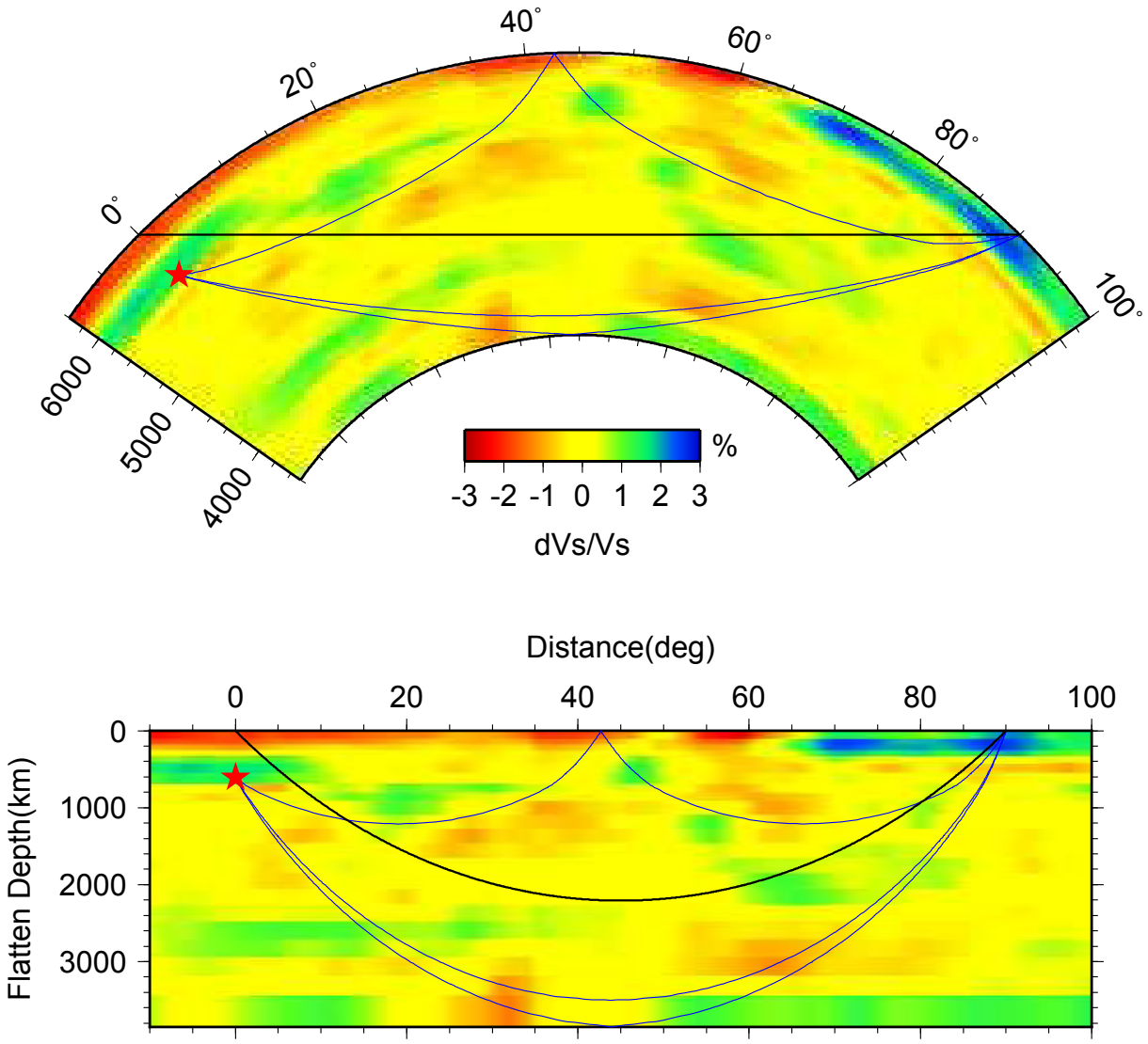

Figure 2.11: The tomography model in the spherical earth (upper panel) and its earth flattened version (lower panel). The ray paths for S, ScS, and SS are shown as blue lines. The black line indicates the geometric ray path for a homogeneous whole space.

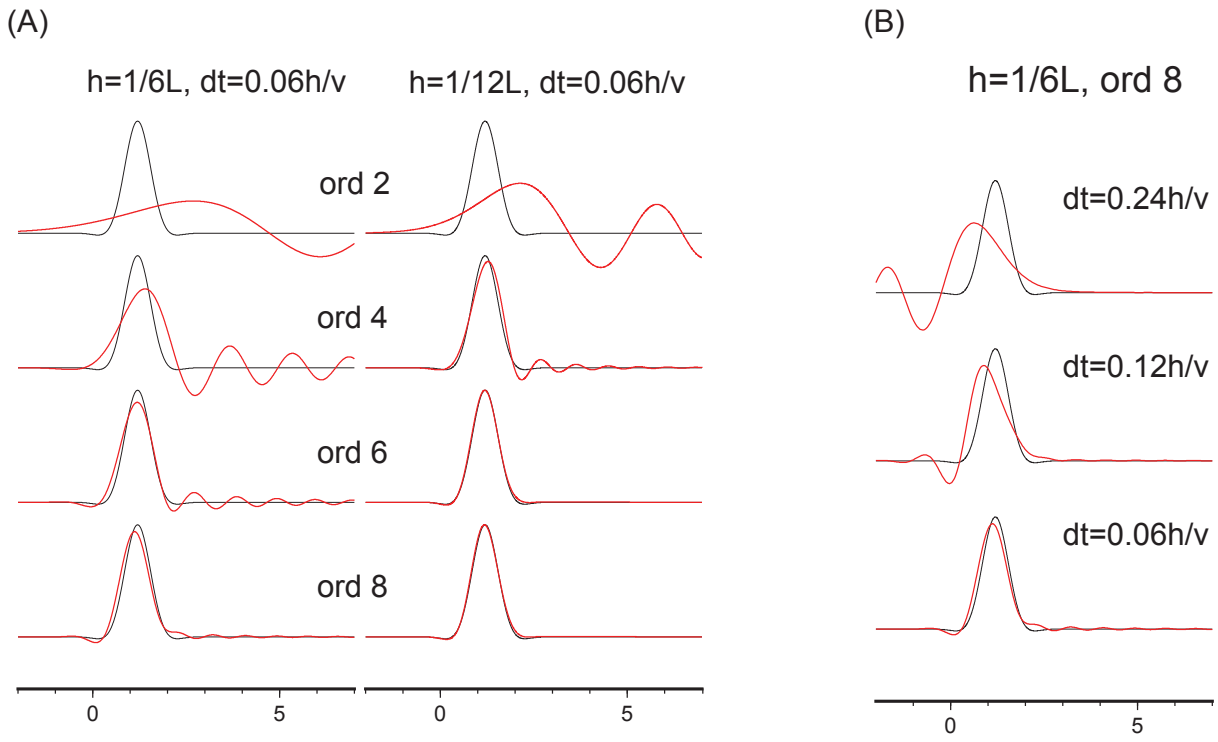

Figure 2.12: Illustration of dispersion error assuming SH simulation in a homogeneous space. The S velocity v is 6 km/s, and the source-time function is of Gaussian shape with central frequency 1Hz, which gives a wavelength L of 6km. The source receiver distance is 6000km, which is $1000L$. (A) Demonstration of spatial dispersion. Red traces are simulation results, and black is the analytical calculation. For two cases of grid space of $h = 1/6L$ and $h = 1/12L$, dispersion error reduces as we increase spatial discretization order. The time discretization is very fine and its dispersion error can be neglected. (B) Demonstration of temporal dispersion. For $h = 1/6L$ and 8th order spatial discretization, time dispersion error decreases as we reduce the time step.

staggered grid method, whose dispersion error can be mitigated by reducing the time step, which does not increase simulation memory requirements. Detailed analysis of this scheme is discussed in (Virieux 1984; Levander 1988). Here we show an example to illustrate the dispersion error. In a homogeneous space with S velocity of 6km/s, we conduct a SH simulation with a source-time function of Gaussian shape (central frequency about 1Hz and wavelength 6km). The source receiver distance is 6000km, which corresponding propagating 1000 cycles. In Fig. 2.12a, we show how the spatial dispersion is reduced by increasing spatial discretization order or halving the grid space. In Fig. 2.12b, we show how the temporal dispersion is mitigated by reducing the time step. Note the phase delay of spatial dispersion and phase advance of temporal dispersion.

thickness(km)	vp(km/s)	vs(km/s)	density (g/cc)
3.95	4.4	2.51	2.0
10.0	6.0	3.46	2.6
16.0	6.7	3.87	2.9
∞	7.7	4.5	3.3

Table 2.1: Layered crust model.

2.3 Validation

Regional modeling

We begin with the simplest problem, producing synthetics for a strike slip fault in a homogeneous space, to test the radiation patterns and 2D to 3D correction. A snapshot of the radial velocity wavefield in the XZ plane is shown in Fig. 2.13a, with three receivers distributed to sample the radiation pattern. The raw finite difference synthetics (velocity seismogram for the line source) are shown in Fig. 2.13b, along with the line source analytical results. After 3D spreading correction, we obtain the point source seismograms in Fig. 2.13c, which are in good agreement with the point source analytical results. Note the wavelet shape difference between line source seismograms and point source seismograms, and that 3D correction is necessary to recover the given wavelet shape, which is the derivative of a Gaussian source time function in this case.

Next, we considered a layered crust (Table 1) using a double-couple source with a strike of 201°, a dip of 10° and a rake of 90° (labeled (201°,10°,90°)). The event is at a depth of 10 km. The source time function is a triangle with a length of 0.6s. In Fig. 2.14, we display the comparison between a well-developed "frequency-wavenumber (FK)" code (Zhu and Rivera 2002) and the new FD code, at an azimuth of 270°. The body wave parts agree well in both amplitude and phase, and the surface wave parts agree well in the phase, but some amplitude differences exist when strong interference of multiple phases arriving at the same time, which is a limitation of our correction method.

Global modeling

A test of global synthetics against modes summation method for PREM model is shown in Fig. 2.15. Note that the plots are in true amplitude, and the fit of both phase and amplitude demonstrates the effectiveness of our correction method for body wave phases. A demonstration of the effects of various 2D to 3D correction terms is shown in Fig. 2.16. After integration of the raw 2D synthetic velocity seis-

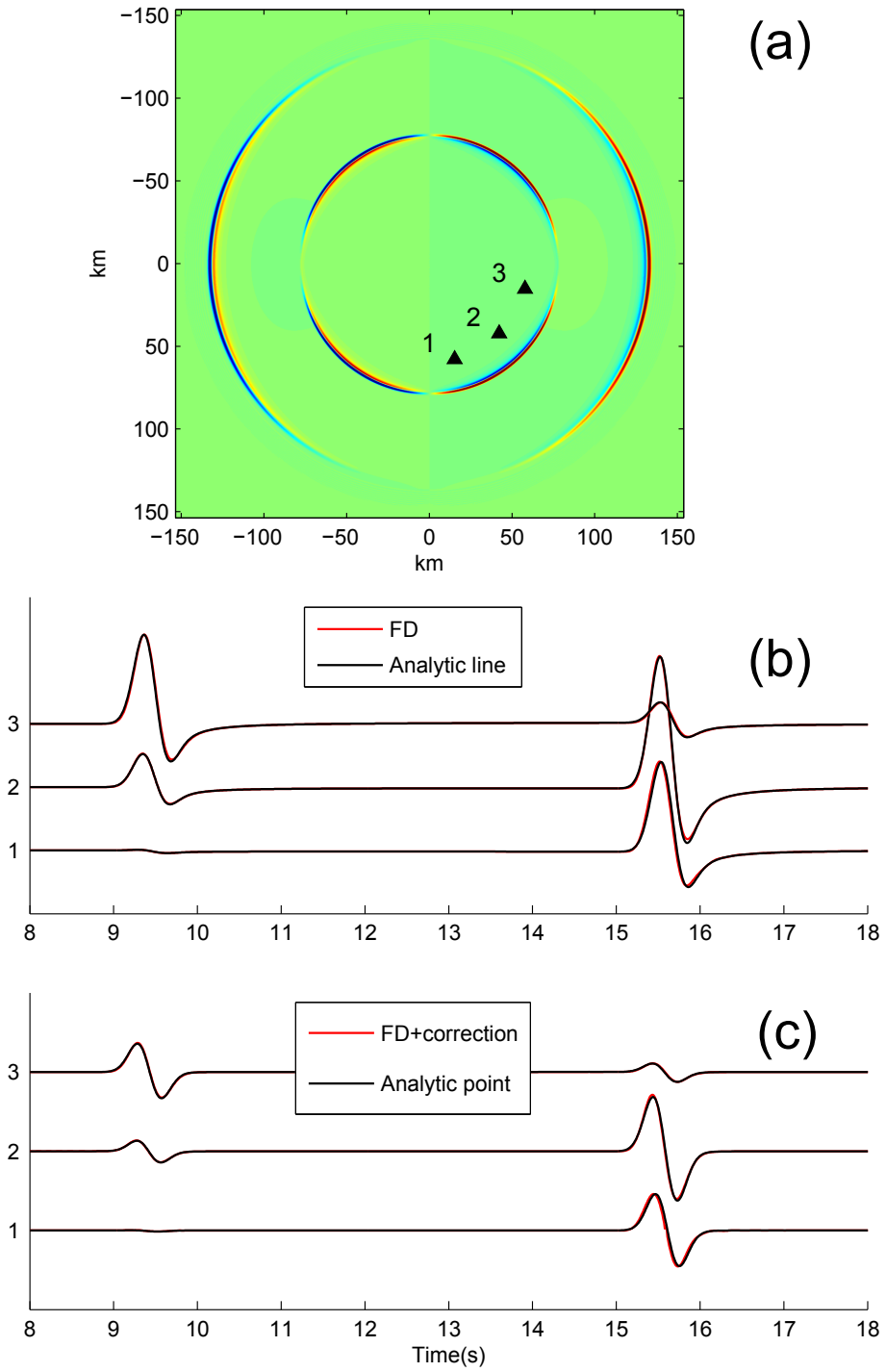

Figure 2.13: Comparison of FD synthetics with the analytic solution. (a) The source is at the origin. Three receivers are shown as black triangle. The snapshot shows the radial component wavefield from a strike slip fault. (b) Comparison of the line source velocity seismogram generated by FD and by analytical calculations at the three receivers. (c) Comparison of point source velocity seismogram obtained from post processing the line source FD simulation and from analytical calculation.

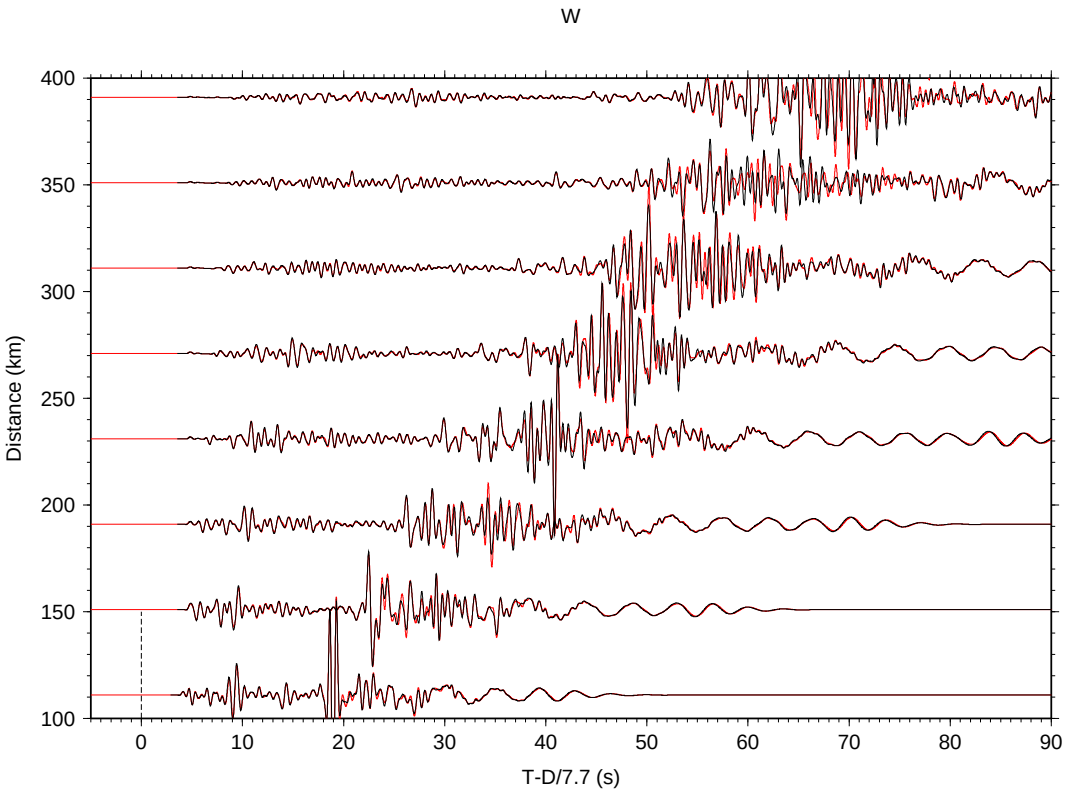

Figure 2.14: Comparison of vertical (Z) component seismograms generated by FD (red) and FK (black) for the layered model shown in Table 2.1. The source is a double couple with strike $201°$, dip $10°$, and rake $90°$. The receivers are at an azimuth of $270°$. The source time function is a symmetrical triangle with a length of 0.6 s. The FD simulation has grid size of 0.1 km and a time step of 0.005 s.

mogram, we obtain the displacement seismogram, which contains long period tails associated with its line source nature. This feature is removed nicely by performing the convolution operation, which results in the point source waveform shapes. The second step requires processing the wavefield to capture the ray parameter p, and performing the $\sqrt{p}$ correction. Note that phases ScS2, ScS3, and ScS4 have progressively smaller ray parameters, which results in different amplitude correction factors. And after making all the correction, the FD synthetics fit the FK synthetics very well.

Another benchmark for earth flattening is shown in Fig. 2.17, where we compare the absolute amplitudes and their decay of S(Sdiff) and P(Pdiff) phases against mode summation method. We can see for the SH case that the fit is very good. For the P-SV case, $m = 3$ fits the absolute amplitude of P(Pdiff) better than $m = 0$. Note that the relative decay for $m = 0$ and $m = 3$ is about the same, and both fit the mode synthetics quite well.

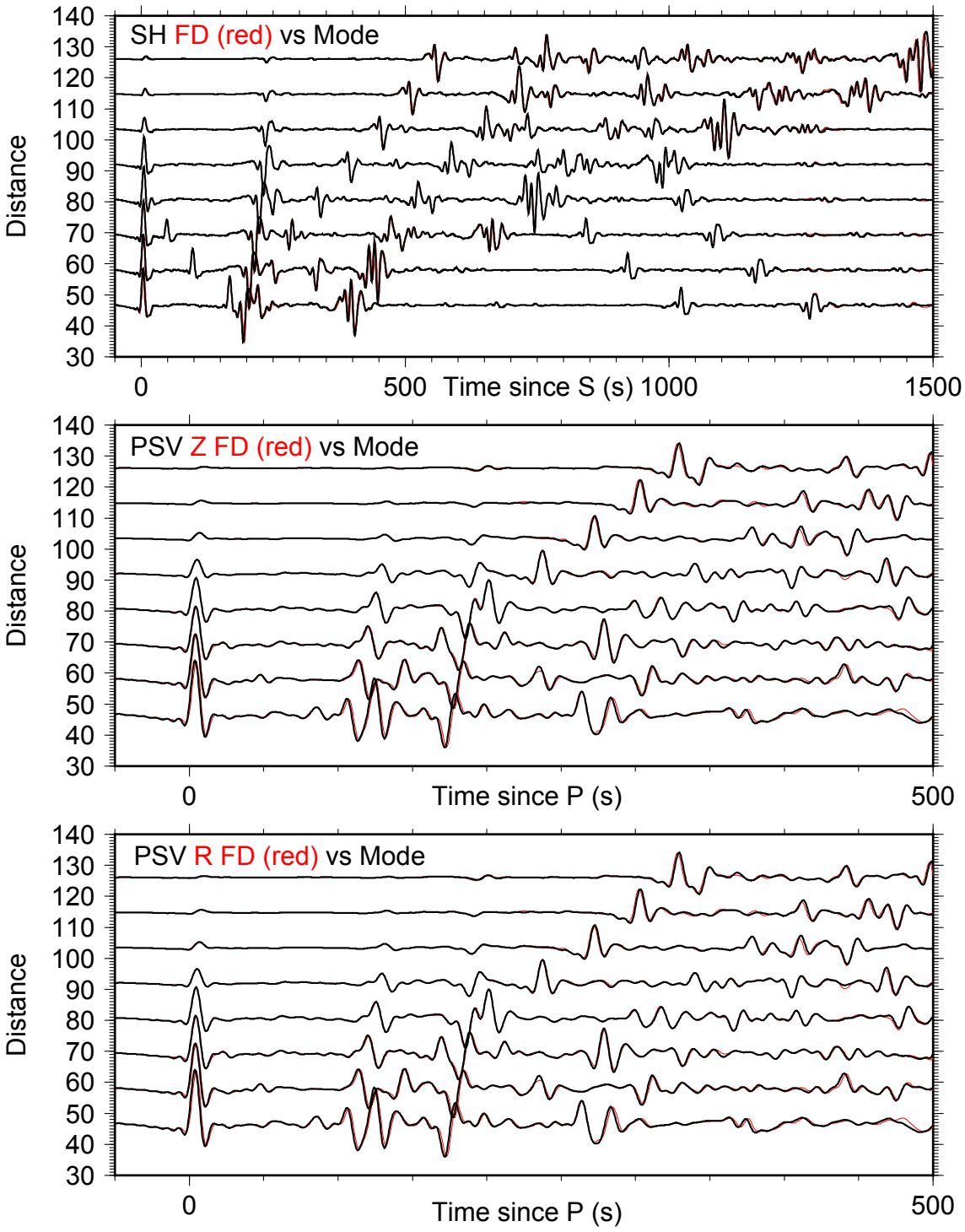

Figure 2.15: Comparison of the displacement seismograms for the PREM model generated using FD and mode summation method. The earth flattening transformation using $m = 3$ for both PSV and SH system. The source is for the 20100218 event, a double couple with strike $71°$, dip $15°$, and rake$166°$. The receivers are at an azimuth of $37°$. The source time function is a symmetrical triangle with a length of 10s. The FD simulation has a grid size of 1.57km and a time step of 0.02s. Both synthetics are filtered to 8-100s because mode summation is accurate for 8s and longer.

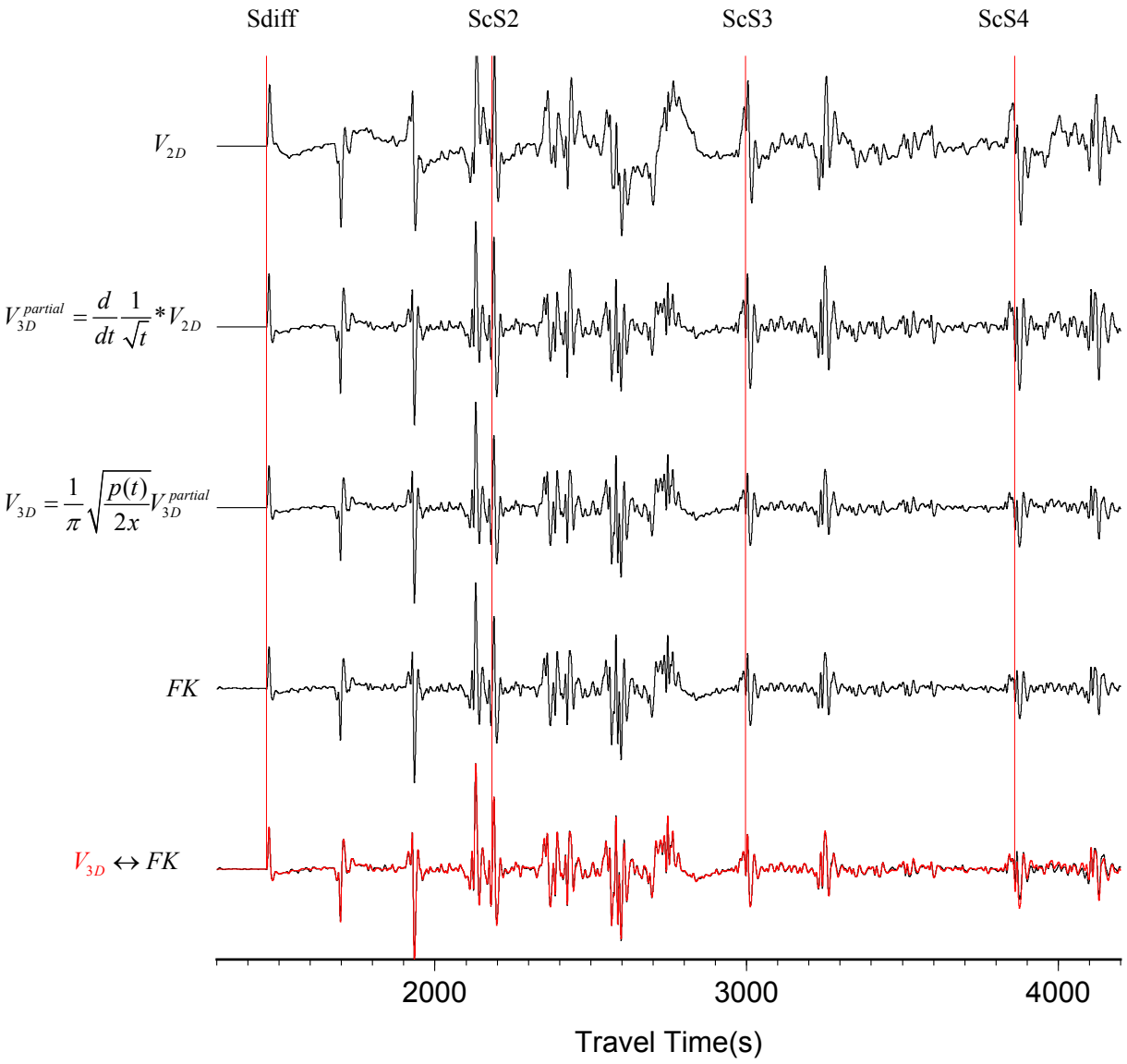

Figure 2.16: Illustration of the correction steps. The displacement SH synthetics are at a distance of 106°. From top to bottom, we show the 2D finite difference synthetics V_{2D} in displacement (an integration of raw velocity seismogram), the correction that just accounts for wavelet shape $V_{2D}^{partial}$, the full correction that accounts for relative amplitudes of different phases V_{3D}, the FK synthetics, and overlay of V_{3D} (red) with FK synthetics (black) at the bottom. All traces are highpass filtered to 300s and shorter period.

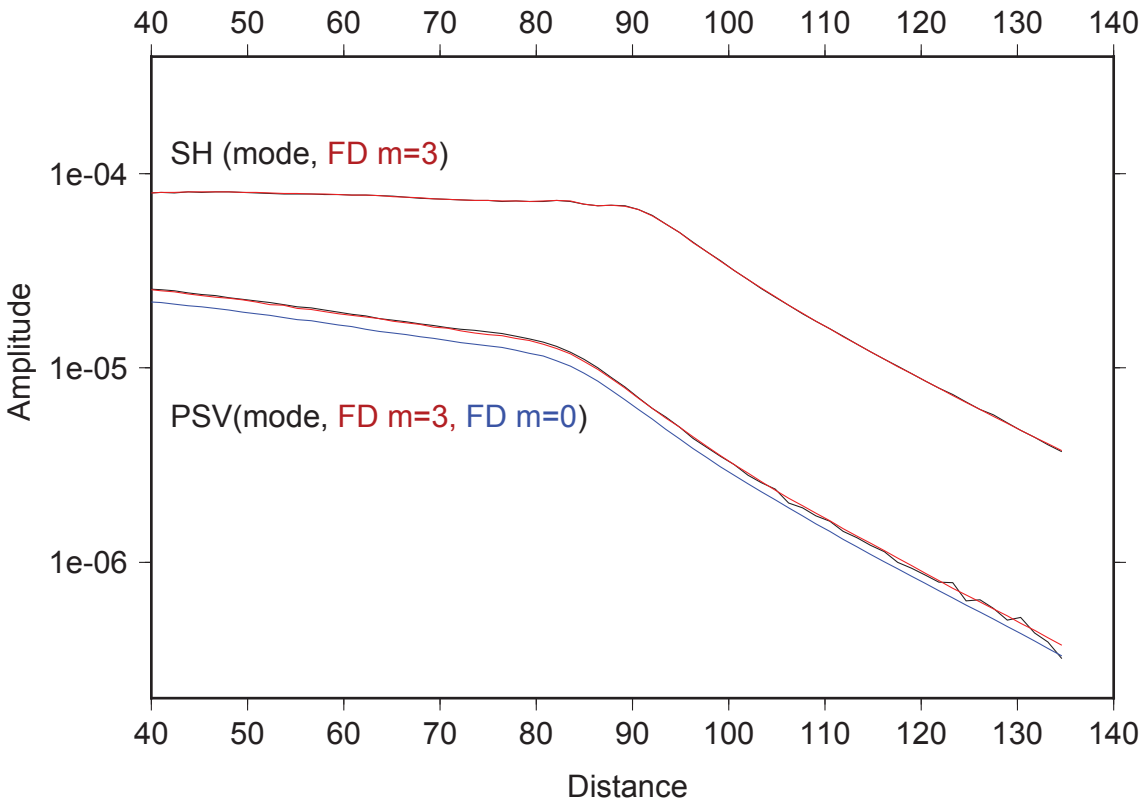

Figure 2.17: Comparison of the amplitude of synthetics between finite difference and mode summation method for S(Sdiff) and P(Pdiff) phases. Note that in the P-SV case the mode and FD best matches for $m = 3$ in the earth-flattening transformation.

Finally, we compared our synthetics with 3D SEM for a model shown in Fig. 2.18a. The 2D synthetics is generated for a cross-section displayed in Fig. 2.18b. Compared with SEM, our synthetics capture most of the features in 3D SEM synthetics as shown in Fig. 2.18c. Although such demonstrations are certainly encouraging, we suggest that when 2D models fit the data this well, it is important to have the ability to check the results against other fully 3D method.

2.4 Application and Discussion

In this section, we discuss some applications of our method. Consider generating the synthetics for the data in Fig. 2.1. The flattened earth model is shown in Fig. 2.11. This cross-section along the subducted North Pacific arc is probably the most complex on Earth and was chosen here because it samples the CMB near a known sample of a D"region (Lay and Helmberger 1983). There is a transitional structure at about 45°(Fig. 2.1) near the CMB where the wavefield begins to sample a relatively fast zone beneath North America. Because such fast zones have been associated with the Scd phases, Sidorin et al. (1999) suggested a mineral phase

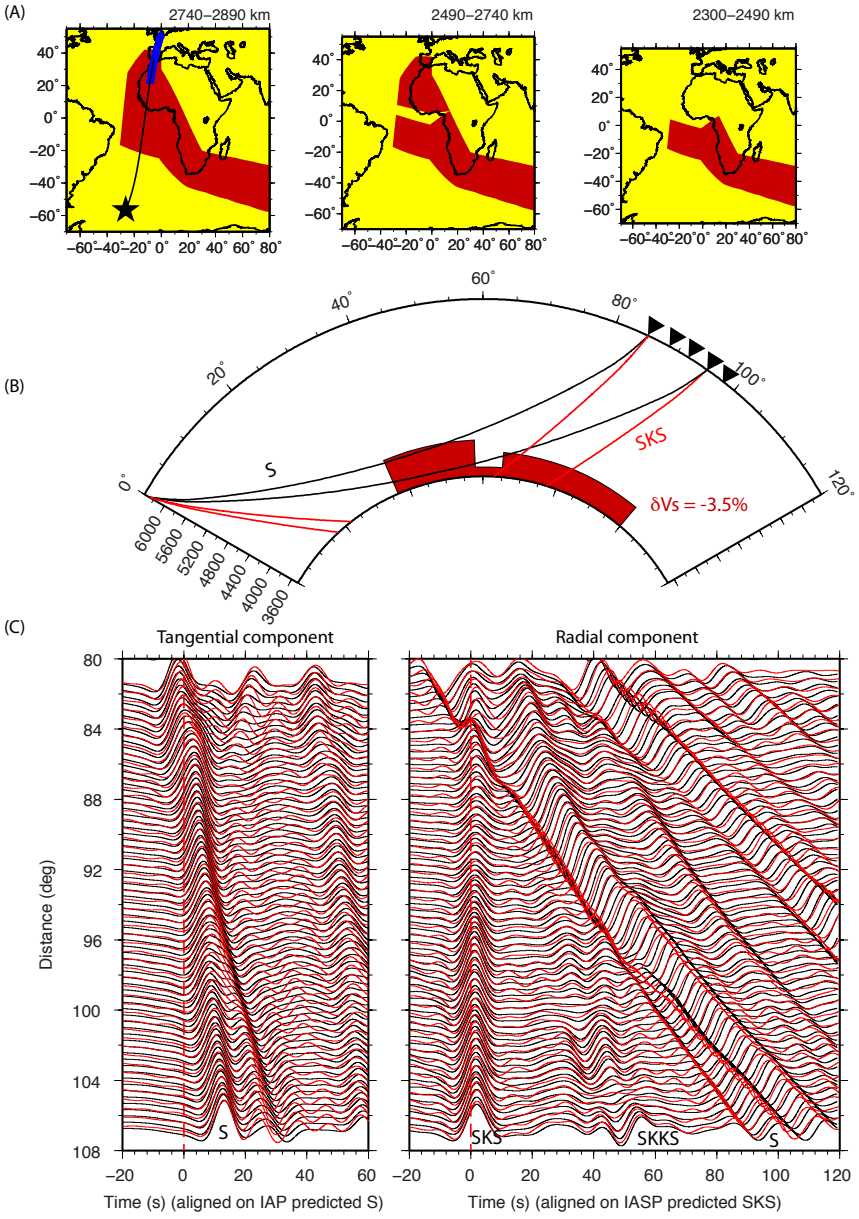

Figure 2.18: Comparison between 2D-FD and 3D-SEM synthetics. (a) The 3D model at different depths used in the SEM calculation. The model is modified after the western edge model of the African Large Low Shear Low Velocity Province (Sun and Miller 2013). Here, the western edge of their model was extended further west to reduce the strong 3D effect from the sharp edge, which makes it more suitable for 2D calculation. The model has a uniform 3.5% shear velocity reduction inside (red region). The black star shows the location of the event and blue points located at Europe denote the dense stations along the same great circle path used in the calculation. (b) displays the 2D cross section along the great circle path in (a). (c) Comparison of the 2D FD (black) and 3D SEM (red) synthetics. The two methods produce good agreement on both travel times and waveforms.

change with a positive Clapeyron slope. They also produced a global map of the phase-boundary height above the CMB, assuming a constant shear velocity jump of 2%, triggered by shear velocity tomography. An even more complicated mapping of tomographic models into a global view of the phase transition was proposed by Sun and Helmberger (2008).

To study this region, stacking of dense record sections are particularly valuable. The stack reveals the complexities of the crossing of SKS and S, as well as SP at the shorter distances, which are shown with GyPSum model FD synthetics in Fig. 2.19a. Although there is some success in predicting the timing shift, the apparent Scd phase in the SH section is missing, because the tomographic model does not attempt to address the phase changes directly. The phase boundary mapping prediction is included in Fig. 2.19b, and fits the data much better. The fit at larger distance (85°to 95°) is not as good as at smaller distance (75°to 85°), where Scd is the second arrival. This may be due to the slab-edge effects, and such complexities can also be studied using the new FD methodology, which will be given in future efforts.

In some cases, out-of-plane model complexity (non-2D model) is important. For example, at shorter-periods, evidence of lateral variation rapidly develops. Such characteristics for Western United States have been examined in terms of multi-pathing by Sun and Helmberger (2011), where both in-plane and out-of-plane complexity is observed in the USArray data for body waves. The out-of-plane features are obvious in azimuthal record sections, (Sun et al. 2009). To model this 3D features, we can calculate several 2D sections using our method, and then combine them using diffraction methods. For example, a simplified approach has been presented by Helmberger and Ni (2005), where 2D synthetics sampling the Fresnel zone region are assembled to simulate the out-of-plane features. Synthetics generated in this way match 3D SEM results for record sections sampling the edges of the African LLSVP (Ni et al. 2005).

Although not addressed here, there are a number of other hybrid methods that interface analytical results for a smooth varying global model with numerical results for a local complex model; see Wen and Helmberger (1998). Such a method was used to model small scale features on the inner core - outer core boundary, (Dai et al. 2012). We use these synthetics as another test against our code, modeling PKiKP phase up to 2Hz (Li et al. 2014). In short, many hybrid models has been developed in this refining tomographic model approach through 2D modeling. The resulting model can be incorporated in full 3D SEM modeling as shown in Chen et al. (2007),

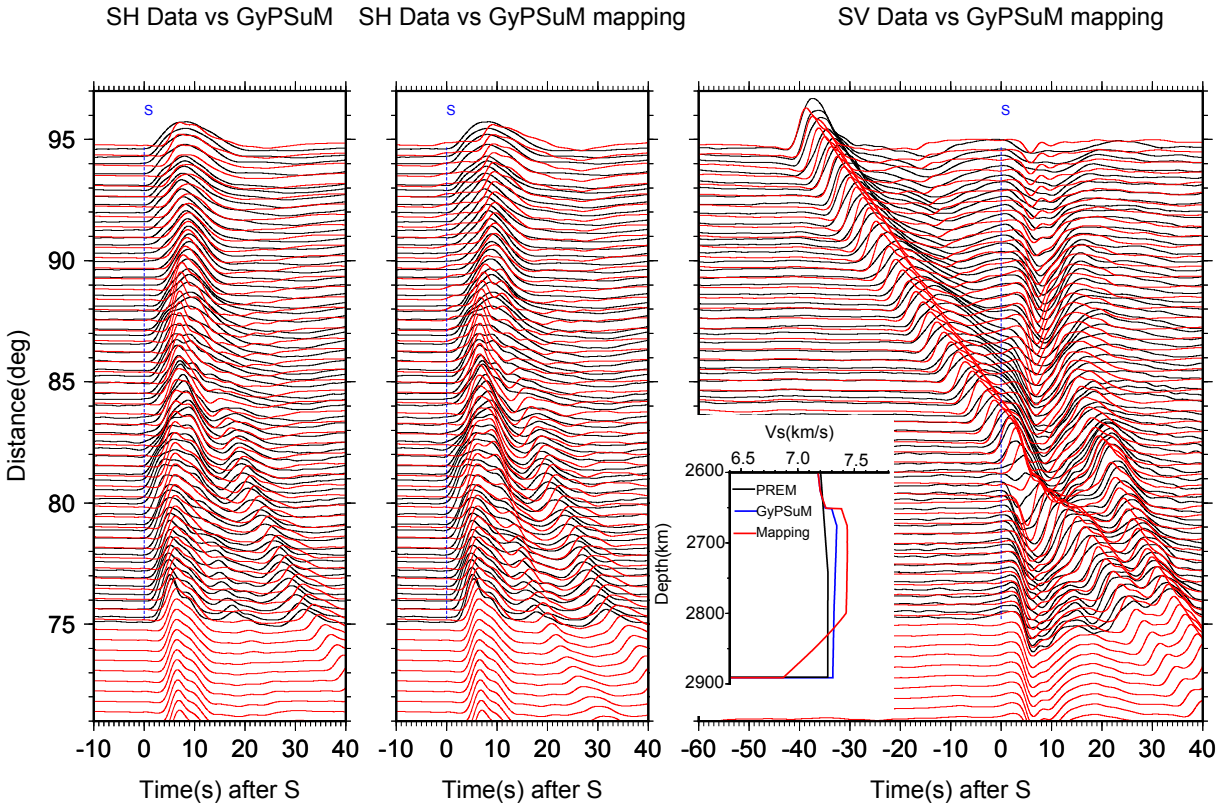

Figure 2.19: Comparison of the data (black) with FD synthetics(red) using the GyPSuM model(blue) for SH system is shown in (a). Comparison of the data (black) with FD synthetics(red) using the phase mapped GyPSuM model for SH system is shown in (b), and for P-SV system shown in (c).

or can be used as starting models in adjoint methods (Tape et al. 2009).

2.5 Conclusions

We further developed 2D finite-difference method for modeling the waveform complexities of relative high frequency global seismic body waves. We have shown a new formulation of the FD source that fixes the low frequency drift, and one that now better accounts for the 3D spreading aspects of the wavefield. We also show that the earth-flattening transformation is effective for global synthetics constructing, where $m = 3$ are preferred in both the SH and the P-SV mapping. In summary, our approach, although involving many approximations, is simple and well validated against other methods, and is adequate for many applications.

2.6 Appendix: Earthquake source

Most earth models have been developed as perturbations of a layered structure, where the wavefield is decomposed into SH and the P-SV systems. This decomposition was

pioneered in papers by Harkrider (1964) and Sato (1969), who derived potentials to separate the wavefield into vertical and horizontal dependencies. A convenient form of these solutions, in terms of the Laplace-transformed displacement in the vertical (W), tangential (V), and radial (Q) directions (see Fig. 2.5), is (Helmberger and Vidale 1988)

$$\begin{aligned}
\hat{W} &= \frac{\partial \hat{\phi}}{\partial z} + sp\hat{\Omega}, \\
\hat{V} &= \frac{1}{r}\frac{\partial \hat{\phi}}{\partial \theta} - \frac{1}{spr}\frac{\partial \hat{\Omega}}{\partial z \partial \theta} - \frac{\partial \hat{\chi}}{\partial r}, \\
\hat{Q} &= \frac{\partial \hat{\phi}}{\partial r} - \frac{1}{sp}\frac{\partial \hat{\Omega}}{\partial r \partial z} + \frac{1}{r}\frac{\partial \hat{\chi}}{\partial \theta},
\end{aligned} \tag{2.23}$$

where z, r, and θ are the vertical, radial, and polar angle coordinates, and

$$\begin{aligned}
\hat{\phi} &= \frac{M_0}{4\pi\rho}\frac{2}{\pi} Im \int_c^{+i\infty+c} \sum_{i=1}^{3} C_i(p) A_i(\theta, \lambda, \delta) \frac{p}{\eta_\alpha} \exp(-s\eta_\alpha |z|) K_{3-i}(spr) dp, \\
\hat{\Omega} &= \frac{M_0}{4\pi\rho}\frac{2}{\pi} Im \int_c^{+i\infty+c} \sum_{i=1}^{3} SV_i(p) A_i(\theta, \lambda, \delta) \frac{p}{\eta_\beta} \exp(-s\eta_\beta |z|) K_{3-i}(spr) dp, \\
\hat{\chi} &= \frac{M_0}{4\pi\rho}\frac{2}{\pi} Im \int_c^{+i\infty+c} \sum_{i=1}^{2} SH_i(p) A_{i+3}(\theta, \lambda, \delta) \frac{p}{\eta_\beta} \exp(-s\eta_\alpha |z|) K_{3-i}(spr) dp,
\end{aligned} \tag{2.24}$$

where K_i is the modified Bessel function, $\eta_v = (1/v^2 - p^2)^{1/2}$, $v = \alpha$ for P waves and $v = \beta$ for S waves, and $i = 1$ for pure strike slip, $i = 2$ for dip slip, and $i = 3$ for 45° dip slip, describing the three fundamental fault mechanisms. The factors C_i, SV_i, SH_i are vertical radiation patterns

$$\begin{aligned}
C_1 &= -p^2, \\
SV_1 &= -\varepsilon p \eta_\beta, \\
SH_1 &= 1/\beta^2, \\
C_2 &= 2\varepsilon p \eta_\alpha, \\
SV_2 &= \left(\eta_\beta^2 - p^2\right), \\
SH_2 &= -\frac{\varepsilon}{\beta^2}\frac{\eta_\beta}{p}, \\
C_3 &= \left(p^2 - 2\eta_\alpha^2\right), \\
SV_3 &= 3\varepsilon p \eta_\beta,
\end{aligned} \tag{2.25}$$

where $\varepsilon = sgn(z)$, and A_i are horizontal radiation patterns

$$\begin{aligned} A_1 &= \sin 2\theta \cos\lambda \sin\delta + 1/2 \cos 2\theta \sin\lambda \sin 2\delta, \\ A_2 &= \cos\theta \cos\lambda \cos\delta - \sin\theta \sin\lambda \cos 2\delta, \\ A_3 &= 1/2 \sin\lambda \sin 2\delta, \\ A_4 &= \cos 2\theta \cos\lambda \sin\delta - 1/2 \sin 2\theta \sin\lambda \sin 2\delta, \\ A_5 &= -\sin\theta \cos\lambda \cos\delta - \cos\theta \sin\lambda \cos 2\delta. \end{aligned} \tag{2.26}$$

Although these equations can be integrated numerically, a useful approximation is obtained by taking the first term of the asymptotic series, and applying Cagniard-de Hoop theory (Helmberger and Harkrider 1977). In the time domain the displacement becomes

$$\begin{aligned} W_\alpha &= L^{-1}\left(\frac{\partial\hat{\phi}}{\partial z}\right) = \frac{M_0}{4\pi\rho}\frac{2}{\pi}A_i(\theta,\lambda,\delta)\frac{d}{dt}\left[\frac{1}{\sqrt{2r}}\frac{1}{\sqrt{t}} * Im\left[C_i(p)\frac{\sqrt{p}}{\eta_\alpha}(-\varepsilon\eta_\alpha)\frac{dp}{dt}\right]\right], \\ W_\beta &= L^{-1}\left(sp\hat{\Omega}\right) = \frac{M_0}{4\pi\rho}\frac{2}{\pi}A_i(\theta,\lambda,\delta)\frac{d}{dt}\left[\frac{1}{\sqrt{2r}}\frac{1}{\sqrt{t}} * Im\left[SV_i(p)\frac{\sqrt{p}}{\eta_\beta}(p)\frac{dp}{dt}\right]\right], \\ Q_\alpha &= L^{-1}\left(\frac{\partial\hat{\phi}}{\partial r}\right) = \frac{M_0}{4\pi\rho}\frac{2}{\pi}A_i(\theta,\lambda,\delta)\frac{d}{dt}\left[\frac{1}{\sqrt{2r}}\frac{1}{\sqrt{t}} * Im\left[C_i(p)\frac{\sqrt{p}}{\eta_\alpha}(-p)\frac{dp}{dt}\right]\right], \\ Q_\beta &= L^{-1}\left(-\frac{1}{sp}\frac{\partial\hat{\Omega}}{\partial r\partial z}\right) = \frac{M_0}{4\pi\rho}\frac{2}{\pi}A_i(\theta,\lambda,\delta)\frac{d}{dt}\left[\frac{1}{\sqrt{2r}}\frac{1}{\sqrt{t}} * Im\left[SV_i(p)\frac{\sqrt{p}}{\eta_\beta}(-\varepsilon\eta_\beta)\frac{dp}{dt}\right]\right], \\ V &= L^{-1}\left(-\frac{\partial\hat{\chi}}{\partial r}\right) = \frac{M_0}{4\pi\rho}\frac{2}{\pi}A_{i+3}(\theta,\lambda,\delta)\frac{d}{dt}\left[\frac{1}{\sqrt{2r}}\frac{1}{\sqrt{t}} * Im\left[SH_i(p)\frac{\sqrt{p}}{\eta_\beta}(p)\frac{dp}{dt}\right]\right], \end{aligned} \tag{2.27}$$

where

$$\begin{aligned} p &= \frac{r}{R^2}t + \mathrm{i}\left(t^2 - \frac{R^2}{V^2}\right)^{1/2}\frac{|z|}{R^2}, \\ \eta_v &= \frac{|z|}{R^2}t - \mathrm{i}\left(t^2 - \frac{R^2}{V^2}\right)^{1/2}\frac{r}{R^2}, \end{aligned} \tag{2.28}$$

and $W_\alpha + W_\beta$ approximates the vertical displacement, $Q_\alpha + Q_\beta$ approximates the radial displacement, and V approximates the tangential displacement, because the other terms in Eq. 2.23 are for the near field and thus neglected. However, because these terms involve simple derivatives of the P-SV and SH fields, they can also be expanded as power series to recover most of the near field (Helmberger and Harkrider 1977).

In Eq. 2.27, the term

$$\frac{1}{\eta}\frac{dp}{dt} = \frac{\mathrm{i}}{(t^2 - R^2/v^2)^{1/2}} \tag{2.29}$$

has a singularity at $t = R/v$, the time when the phase arrives. Thus using the first motion approximation, Eq. 2.28 becomes $p = p_0 = r/Rv$, and Eq. 2.27 can be simplified as

$$Im\left[\sqrt{p}(\cdots)\frac{1}{\eta}\frac{dp}{dt}\right] \approx Im\left[\sqrt{p_0}(\cdots)\frac{1}{\eta}\frac{dp}{dt}\right] = \sqrt{p_0}Im\left[(\cdots)\frac{1}{\eta}\frac{dp}{dt}\right], \qquad (2.30)$$

where $\sqrt{p_0}$ is real. Note that without $\sqrt{p}$ in the equation, $Im[\ldots]$ satisfies the 2D wave equation, similar to the term V_{2D} in Eq. 2.4.

The foregoing deduction is for a homogeneous space, but it can be generalized to flat or dipping layered media using general ray theory (Hong and Helmberger 1977). We can rewrite the displacement as explicit contributions from different fundamental faults, for example $Q_\alpha = \frac{d}{dt}\left(\frac{1}{\sqrt{t}} * \sqrt{p_0(t)/r}(\sum_{i=1}^{3} A_i Q_\alpha^i)\right)$, where Q_α^i and other similar terms are

$$\begin{aligned}
Q_\alpha^1(r,z,t) &= r\left(r^2 - 3z^2 + T_\alpha(3z^2)\right)\Psi_\alpha \\
Q_\beta^1(r,z,t) &= r\left(-r^2 + 3z^2 + T_\beta(r^2 - 2z^2)\right)\Psi_\beta \\
W_\alpha^1(r,z,t) &= -z\left(-3r^2 + z^2 + T_\alpha(2r^2 - z^2)\right)\Psi_\alpha \\
W_\beta^1(r,z,t) &= -z\left(3r^2 - z^2 + T_\beta(-2r^2 + z^2)\right)\Psi_\beta \\
Q_\alpha^2(r,z,t) &= -z\left(6r^2 - 2z^2 + T_\alpha(-4r^2 + 2z^2)\right)\Psi_\alpha \\
Q_\beta^2(r,z,t) &= -z\left(-6r^2 + 2z^2 + T_\beta(5r^2 - z^2)\right)\Psi_\beta \\
W_\alpha^2(r,z,t) &= r\left(2r^2 - 6z^2 + T_\alpha(-2r^2 + 4z^2)\right)\Psi_\alpha \\
W_\beta^2(r,z,t) &= r\left(-2r^2 + 6z^2 + T_\beta(r^2 - 5z^2)\right)\Psi_\beta \\
Q_\alpha^3(r,z,t) &= r\left(-3r^2 + 9z^2 + T_\alpha(2r^2 - 7z^2)\right)\Psi_\alpha \\
Q_\beta^3(r,z,t) &= r\left(3r^2 - 9z^2 + T_\beta(-3r^2 + 6z^2)\right)\Psi_\beta \\
W_\alpha^3(r,z,t) &= -z\left(9r^2 - 3z^2 + T_\alpha(-8r^2 + z^2)\right)\Psi_\alpha \\
W_\beta^3(r,z,t) &= -z\left(-9r^2 + 3z^2 + T_\beta(6r^2 - 3z^2)\right)\Psi_\beta
\end{aligned} \qquad (2.31)$$

where

$$\begin{aligned}
T_\gamma &= \frac{R^2}{t^2\gamma^2}, \\
\Psi_\gamma &= \frac{M_0}{4\pi^2\rho}\sqrt{2}\frac{t^2}{R^6\sqrt{1-T_\gamma}}H(t - R/\gamma),
\end{aligned} \qquad (2.32)$$

for P-SV, and for SH

$$\begin{aligned}
V^4 &= \frac{M_0}{4\pi^2\rho}\sqrt{2}\frac{r}{R}\frac{1}{\beta^2 R}\frac{1}{\sqrt{1-T_\beta}}H\left(t - R/\beta\right), \\
V^5 &= \frac{M_0}{4\pi^2\rho}\sqrt{2}\frac{\sqrt{R^2 - r^2}}{R}\frac{1}{\beta^2 R}\frac{1}{\sqrt{1-T_\beta}}H\left(t - R/\beta\right).
\end{aligned}$$

Note that $W_{2D} = W^i_\alpha + W^i_\beta, Q_{2D} = Q^i_\alpha + Q^i_\beta$ satisfies the 2D wave equation, and can be interfaced using 2D finite differences.

The above formula was derived for cylindrical coordinates. However, it is better to use Cartesian coordinates to obtain a formula suitable for FD source injection, see Fig. 2.5. Converting from cylindrical coordinates $\{Q, V, W\}(r, \theta, z)$ to Cartesian coordinates $\{U_x, U_y, U_z\}(r, \theta, z)$ is straightforward for $x \geq 0$, but for $x < 0$, it must be noted that the sign convention for displacement changes, and $\theta = \theta_c + \pi$. We obtain

$$\{U_x, U_y, U_z\}(x, z) = \{Q, V, W\}\,(r = x, z, \theta = \theta_c)\,, \quad x \geq 0,$$
$$\{U_x, U_y, U_z\}(x, z) = \{-Q, -V, W\}\,(r = -x, z, \theta = \theta_c + \pi)\,, \quad x < 0.$$

Thus, for both $x \geqq 0$ and $x < 0$

$$\{U_x, U_y, U_z\}(x, z) = \{Q, V, W\}\,(r = x, z, \theta = \theta_c)\,. \tag{2.33}$$

Therefore, we only need to change r to x in Eq. 2.31 , and use $\theta = \theta_c$ for both $x \geqq 0$ and $x < 0$ to obtain a solution in Cartesian coordinates.

References

Aki, Keiiti and Paul G Richards (1980). *Quantitative seismology : theory and methods*. San Francisco: W.H. Freeman, 2 v. (xiv, 932, 16 p.) ISBN: 0716710587 (v. 1) 0716710595 (v. 2) (cit. on pp. 14, 18, 22).

Alterman, Z and F C Karal (1968). "Propagation of elastic waves in layered media by finite difference methods". In: *Bulletin of the Seismological Society of America* 58.1, pp. 367–398 (cit. on pp. 10, 20).

Biswas, N. and L. Knopoff (1970). "Exact earth-flattening calculation for Love waves". In: *Bulletin of the Seismological Society of America* 60.4, pp. 1123–1137 (cit. on p. 26).

Cerveny, Vlastislav (2001). *Seismic ray theory*. Vol. 148. 2. Cambridge University Press. Chap. 2. ISBN: 0521366712. DOI: 10.1046/j.1365-246X.2002.01638.x (cit. on p. 16).

Chapman, C H (1973). "The earth flattening transformation in body wave theory". In: *Geophysical Journal of the Royal Astronomical Society* 35, pp. 55–70 (cit. on p. 26).

– (2004). *Fundamentals of seismic wave propagation*. Cambridge University Press. ISBN: 052181538X (cit. on pp. 14, 18).

Chen, M et al. (2007). "Waveform modeling of the slab beneath Japan". In: *Journal of Geophysical Research-Solid Earth* 112.B2. DOI: ArtnB02305Doi10.1029/2006jb004394 (cit. on pp. 10, 37).

Coutant, O, J Virieux, and A Zollo (1995). “Numerical source implementation in a 2D finite difference scheme for wave propagation”. In: *Bulletin of the Seismological Society of America* 85.5, pp. 1507–1512 (cit. on pp. 14, 19).

Crotwell, H Philip, Thomas J Owens, and Jeroen Ritsema (1999). “The TauP toolkit: flexible seismic travel-time and ray-path utilities”. In: *Seismological Research Letters* 70, pp. 154–160 (cit. on p. 11).

Dahlen, F. A. and Jeroen Tromp (1998). *Theoretical Global Seismology*. Princeton, N.J.: Princeton University Press, p. 1025 (cit. on p. 26).

Dai, Zhiyang, Wei Wang, and Lianxing Wen (2012). “Irregular topography at the Earth’s inner core boundary.” In: *Proceedings of the National Academy of Sciences of the United States of America* 109.20, pp. 7654–8. ISSN: 1091-6490. DOI: 10.1073/pnas.1116342109 (cit. on p. 37).

Furumura, T, B L N Kennett, and M Furumura (1998). “Seismic wave field calculation for laterally heterogeneous whole earth models using the pseudospectral method”. In: *Geophysical Journal International* 135, pp. 845–860 (cit. on p. 10).

Gilbert, Freeman and Donald V. Helmberger (1972). “Generalized Ray Theory for a Layered Sphere”. In: *Geophysical Journal International* 27.1, pp. 57–80. ISSN: 0956-540X. DOI: 10.1111/j.1365-246X.1972.tb02347.x (cit. on p. 26).

Graves, Robert W (1996). “Simulating seismic wave propagation in 3D elastic media using staggered-grid finite differences”. In: *Bulletin of the Seismological Society of America* 86.4, pp. 1091–1106 (cit. on p. 17).

Harkrider, David (1964). “Surface waves in multilayered elastic media I. Rayleigh and Love waves from buried sources in a multilayered elastic half-space”. In: *Bulletin of the Seismological Society of America* 54.2, pp. 627–679 (cit. on p. 39).

Helmberger, D. V. and S. Ni (2005). “Approximate 3D Body-Wave Synthetics for Tomographic Models”. In: *Bulletin of the Seismological Society of America* 95.1, pp. 212–224. ISSN: 0037-1106. DOI: 10.1785/0120040004 (cit. on p. 37).

Helmberger, Don and David Harkrider (1977). “Modeling earthquakes with generalized ray theory”. In: *Modern problems in elastic wave propagation*. New York: John Wiley & Sons, pp. 479–518 (cit. on p. 40).

Helmberger, Donald V. (1973). “Numerical seismograms of long-period body waves from seventeen to forty degrees”. In: *Bulletin of the Seismological Society of America* 63.2, pp. 633–646 (cit. on p. 26).

Helmberger, Donald V and John E Vidale (1988). “Modeling strong motions produced by earthquakes with two-dimensional numerical codes”. In: *Bulletin of the Seismological Society of America* 78.1, pp. 109–121 (cit. on pp. 22, 39).

Hong, T.L. and D.V. Helmberger (1977). “Generalized ray theory for dipping structure”. In: *Bulletin of the Seismological Society of America* 67.4, pp. 995–1008 (cit. on p. 41).

Jahnke, Gunnar et al. (2008). "Global SH -wave propagation using a parallel axisymmetric spherical finite-difference scheme: application to whole mantle scattering". In: *Geophysical Journal International* 173.3, pp. 815–826. ISSN: 0956540X. DOI: 10.1111/j.1365-246X.2008.03744.x (cit. on p. 10).

Komatitsch, Dimitri and Jeroen Tromp (1999). "Introduction to the spectral element method for three-dimensional seismic wave propagation". In: *Geophysical Journal International* 139, pp. 806–822 (cit. on p. 9).

Lay, Thorne and Donald V Helmberger (1983). "A shear velocity discontinuity in the lower mantle". In: *Geophysical Research Letters* 10.1, pp. 63–66 (cit. on p. 35).

Levander, Alan R (1988). "Fourth-order finite-difference P-SV seismograms". In: *Geophysics* 53.11, pp. 1425–1436. DOI: 10.1190/1.1442422 (cit. on pp. 27, 29).

Li, Dunzhu, Donald V Helmberger, and Daoyuan Sun (2014). "Notes on the variability of reflected inner-core phases". In: *Earthquake Science*, in review (cit. on p. 37).

Micikevicius, Paulius (2009). "3D finite difference computation on GPUs using CUDA". In: *GPGPU-2: Proceedings of the 2nd Workshop on General Purpose Processing on Graphics Processing Units*, pp. 79–84. ISBN: 9781605585178 (cit. on p. 27).

Miksat, J, T M Müller, and F Wenzel (2008). "Simulating three-dimensional seismograms in 2.5-dimensional structures by combining two-dimensional finite difference modelling and ray tracing". In: *Geophysical Journal International* 174.1, pp. 309–315. DOI: 10.1111/j.1365-246X.2008.03800.x (cit. on p. 16).

Mittet, Rune (2002). "Free-surface boundary conditions for elastic staggered-grid modeling schemes". In: *Geophysics* 67.5, pp. 1616–1623 (cit. on p. 27).

Müller, G. (1971). "Approximate treatment of elastic body waves in media with spherical symmetry". In: *Geophysical Journal of the Royal Astronomical Society* 23, pp. 435–449 (cit. on pp. 25, 26).

Ni, Sidao, Don V. Helmberger, and Jeroen Tromp (2005). "Three-dimensional structure of the African superplume from waveform modelling". In: *Geophysical Journal International* 161.2, pp. 283–294. ISSN: 0956540X. DOI: 10.1111/j.1365-246X.2005.02508.x (cit. on p. 37).

Nissen-Meyer, Tarje, Alexandre Fournier, and F. a. Dahlen (2007). "A two-dimensional spectral-element method for computing spherical-earth seismograms - I. Moment-tensor source". In: *Geophysical Journal International* 168.3, pp. 1067–1092. ISSN: 0956540X. DOI: 10.1111/j.1365-246X.2006.03121.x (cit. on p. 10).

Saikia, Chandan K. and D. V. Helmberger (1997). "Approximation of Rupture Directivity in Regional Phases Using Upgoing and Downgoing Wave Fields". In: *Bulletin of the Seismological Society of America* 87.4, pp. 987–998 (cit. on p. 24).

Sato, Ryosuke (1969). "Formulations of solutions and for earthquake source models and some related problems". In: *Journal of physics of the earth* 17.2, pp. 101–110 (cit. on p. 39).

Sidorin, Igor, Michael Gurnis, and Don V. Helmberger (1999). "Evidence for a Ubiquitous Seismic Discontinuity at the Base of the Mantle". In: *Science* 286.5443, pp. 1326–1331. ISSN: 00368075. DOI: 10.1126/science.286.5443.1326 (cit. on p. 35).

Simmons, Nathan a. et al. (2010). "GyPSuM: A joint tomographic model of mantle density and seismic wave speeds". In: *Journal of Geophysical Research* 115.B12, pp. 1–24. ISSN: 0148-0227. DOI: 10.1029/2010JB007631 (cit. on p. 11).

Sun, Daoyuan and Don Helmberger (2008). "Lower mantle tomography and phase change mapping". In: *Journal of Geophysical Research* 113.B10, B10305. ISSN: 0148-0227. DOI: 10.1029/2007JB005289 (cit. on p. 37).

– (2011). "Upper-mantle structures beneath USArray derived from waveform complexity". In: *Geophysical Journal International* 184.1, pp. 416–438. ISSN: 0956540X. DOI: 10.1111/j.1365-246X.2010.04847.x (cit. on p. 37).

Sun, Daoyuan and Meghan S. Miller (2013). "Study of the western edge of the African Large Low Shear Velocity Province". In: *Geochemistry, Geophysics, Geosystems* 14. ISSN: 15252027 (cit. on p. 36).

Sun, Daoyuan et al. (2009). "Direct measures of lateral velocity variation in the deep Earth". In: *Journal of Geophysical Research-Solid Earth* 114, B05303. DOI: ArtnB05303Doi10.1029/2008jb005873 (cit. on p. 37).

Tape, Carl et al. (2009). "Adjoint tomography of the southern California crust." In: *Science (New York, N.Y.)* 325.5943, pp. 988–92. ISSN: 1095-9203. DOI: 10.1126/science.1175298 (cit. on p. 38).

Toyokuni, Genti and Hiroshi Takenaka (2006). "FDM computation of seismic wavefield for an axisymmetric earth with a mement tensor point source". In: *Earth Planets Space* 58, pp. 29–32 (cit. on p. 10).

Tromp, Jeroen et al. (2010). "Near real-time simulations of global CMT earthquakes". In: *Geophysical Journal International* 183.1, pp. 381–389. ISSN: 0956540X. DOI: 10.1111/j.1365-246X.2010.04734.x (cit. on p. 9).

Vidale, John E and Donald V Helmberger (1987). "Path effects in strong motion seismology". In: *Seismic strong motion synthetics*. Ed. by Bruce A. Bolt. London: Academic Press Inc (cit. on pp. 10, 23).

Vidale, John E, Donald V Helmberger, and Robert W Clayton (1985). "Finite-difference seismograms for SH waves". In: *Bulletin of the Seismological Society of America* 75.6, pp. 1765–1782 (cit. on pp. 20, 22).

Virieux, Jean (1984). "SH-wave propagation in heterogeneous media: Velocity-stress finite-difference method". In: *Geophysics* 49.11, pp. 1933–1957 (cit. on pp. 27, 29).

Wang, Yanbin, Hiroshi Takenaka, and Takashi Furumura (2001). "Modelling seismic wave propagation in a two-dimensional cylindrical whole-earth model using the pseudospectral method". In: *Geophysical Journal International* 145.3, pp. 689–708. ISSN: 0956540X. DOI: 10.1046/j.1365-246x.2001.01413.x (cit. on p. 10).

Wen, Lianxing and Donald V Helmberger (1998). "A two-dimensional P-SV hybrid method and its application to modeling localized structures near the core-mantle boundary". In: *Journal of Geophysical Research* 103.B8, pp. 17901–17918 (cit. on p. 37).

Zhang, Wei and Yang Shen (2010). "Unsplit complex frequency-shifted PML implementation using auxiliary differential equations for seismic wave modeling". In: *Geophysics* 75.4, T141–T154. ISSN: 0016-8033. DOI: 10.1190/1.3463431 (cit. on p. 27).

Zhu, Lupei and Luis a. Rivera (2002). "A note on the dynamic and static displacements from a point source in multilayered media". In: *Geophysical Journal International* 148, pp. 619–627. ISSN: 0956540X. DOI: 10.1046/j.1365-246X.2002.01610.x (cit. on p. 30).

Chapter 3

NOTES ON THE VARIABILITY OF REFLECTED INNER CORE PHASES

Li, Dunzhu and Sun, Daoyuan and Helmberger, Don (2014). "Notes on the variability of reflected inner core phases". In: *Earthquake Science* 27, pp. 441–468. DOI: 10.1007/s11589-014-0093-9.

Recent events beneath Central America have produced excellent sets of inner core reflection (PKiKP phase) at high frequency recorded by USArray ranging from 18° to 30°. However, the amplitude of this phase displays considerable scatter with a factor of 6 or more. Such scatter has been attributed to upper mantle scattering and the Inner Core Boundary (ICB) in combination. Here, we show that neighboring events share upper mantle scatterers beneath the receivers, and their ratio allows a clearer image of deep earth structure. After confirming that some of the measured variation is indeed due to deep structure, we stacked nearby traces to reduce fine scale variations which are mostly due to shallow structure. Then, the remaining relatively large scale variation pattern of PKiKP phase is caused by the inner core boundary, as demonstrated by numerical experiments. After migration of data to the ICB we observe a consistent image. We find that such a pattern can be explained by a patch of mushy material of a few kilometers high where the material changes gradually from that of the outer core to that of the inner core.

3.1 Introduction

The solidification process at the Inner-Core-Boundary (ICB) strongly influences the Earth's magnetic field, and becomes of key importance to the geodynamo. Laboratory experiments indicate that a thin mushy layer forms at the boundary between a fluid and the growing solid, and Shimizu et al. (2005) suggest that such a zone should exist at the ICB depending on the properties of the light element present. Such a layer is likely to be highly variable given the dynamic circulation involved. Thus, seismologists have been addressing properties of this interface with an array of interesting observations. Most detailed seismic studies of the ICB involve the various branches of the PKP system and, in particular, the differential times between PKiKP and PKIKP (Fig. 3.1), by Poupinet et al. (1983) and Cormier

and Choy (1986). Hemispheric difference became well mapped more recently (see e.g., Niu and Wen 2001; Wen and Niu 2002; Waszek et al. 2011). Short wavelength variations on the ICB based on these phases are discussed by Cao et al. (2007) along with possible temporal variation, which is also discussed in an earlier paper by Wen (2006). Because PKiKP is essentially at critical angle at ranges where PKIKP is also observed ($130^\circ - 140^\circ$), it is not sensitive to density changes across the ICB, i.e., Cormier and Richards (1977) and Song and Helmberger (1992). The ICB has also been investigated at small distances (precritical angles) where the amplitude ratio of PKiKP to PcP from the LASA array was used to estimate the density jump Engdahl et al. (1970). One of the first attempts to model the fine-structure of the ICB was by Cummins and Johnson (1988) where they demonstrated that the PKiKP precritical angle reflections will be greatly reduced by adding a transition zone. Thus they concluded that the few existing measurements indicated a very sharp interface, less than 2 km. A number of global studies followed, i.e., Shearer and Masters (1990), attempting to further constrain the density jump at the ICB. More recently, short-period arrays have provided more definitive measurements of this ratio, Kawakatsu (2006), and papers by Koper (2004) and Koper and Dombrovskaya (2005), involving both differential times and amplitudes. They proposed a density jump of 0.525 ± 0.239 (g/cm^3) where they attempted to establish a meaningful error estimate. This proves difficult but their studies and others suggest that earthquake radiation pattern effects are small (with corrections less than 25%) since the take-off angles for PcP and PKiKP are similar, see Fig. 3.1. Radiation pattern effects have also been addressed by Tkalčić et al. (2010), in which they argue that differential radiation amplitudes between PcP and PKiKP can probably be neglected. They also argue that much larger variations of this ratio are produced by path effects approaching the individual stations, and question the usefulness of these ratio measurements. They found that a deep event beneath the Kuril Islands, as recorded on the J-Array (Japan), had a negative correlation between the identification of PcP and PKiKP, i.e., if one can detect clean PcP, the PKiKP phase is in the noise and vice versa. They explain this feature by adding an upper-mantle heterogeneous layer with vertically elongated perturbations (exponential auto correlation random media, with vertical scales 100 km and horizontal scale 2 km, 5% RMS in P-velocity). Thus, the difference in the upcoming ray paths allows one phase to be enhanced but not the other. They suggest that the presence of the slab along the path to Japan could be the cause of such a layer. Observations from the oceanic direction appear not to be affected as much(Kawakatsu 2006). Still more recently, Dai et al. (2012) use the rapid variation

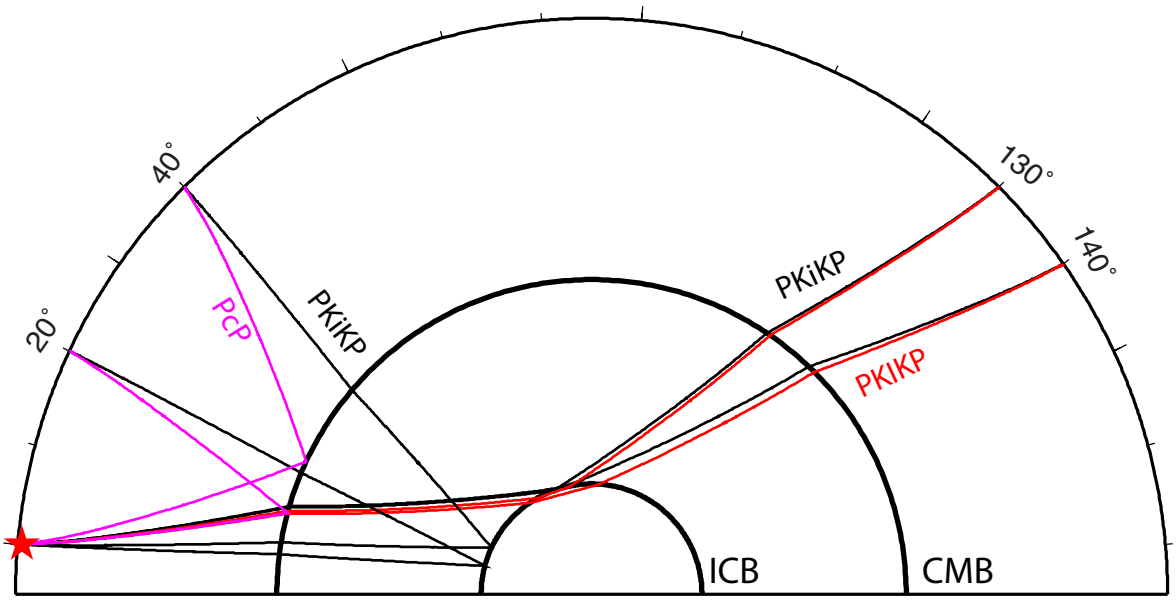

Figure 3.1: Diagram of example geometrical ray paths for the two main phases used in this study: PKiKP (black) and PcP (magenta). Ray paths for PKiKP (black) and PKIKP (red) at critical angle ranges ($130°$to $140°$) are also displayed.

in the PKiKP/PcP ratio to map out a box-car structure, 14 km high with a horizontal length of about 3 degrees, as observed on the dense Hi-Net Array covering Japan.

In short, there appears to be considerable evidence for fluctuations in the pre critical angle PKiKP/PcP ratio as discussed above. This is probably highly situation-specific as suggested by Adushkin and Ovchinnikov (2004). Here, we will investigate these phases as observed on the USArray and apply our newly developed simulation code (Li et al. 2014) to address the many causes for complexities at these high frequencies. Because both the data and simulations are relatively complicated we have added two appendixes. The first involves automated processing of waveforms that display a mixture of noise and scattering effects from deep heterogeneities. The second treats the simulation of short-period waveforms and the placement of scattering boxes at the source region and receiver region. The latter serves as a primer to previous simulation efforts.

3.2 Data and Processing

Detecting the PKiKP phase at precritical angles is difficult because of its small amplitude. However, we have found a few events beneath Central America in the search window 2005 to 2012 displaying this phase, see Table 3.1. We studied the two events with the largest number of visual detections which happened to be within $1.6°$

Origin	Latitude	Longitude	Depth(km)	Mw
2006-12-03 20:52:15.73	14.013	-91.342	61.0	5.98
2007-06-08 13:32:02.20	13.769	-90.895	65.0	5.83
2007-07-06 01:09:18.48	16.495	-93.784	121.1	6.06
2007-07-23 22:30:08.45	14.381	-90.954	113.0	5.50
2008-11-15 23:03:16.59	13.072	-88.927	48.0	5.81
2009-01-17 02:57:31.59	15.742	-92.605	174.1	5.82
2009-04-27 16:46:27.49	16.941	-99.568	33.3	5.83
2009-05-03 16:21:45.75	14.618	-91.252	108.0	6.28
2009-11-26 19:08:11.19	13.467	-90.051	55.0	5.95

Table 3.1: Events that contain visible PKiKP phases after filtering to 1 to 3Hz

(< 180km) of each other, see Fig. 3.2. Note that because the TA array is marching eastward, the two events have limited number of common stations, which however prove to be particularly important. The broadband record section of the 20091126 event is displayed in Fig. 3.3A, where PKiKP cannot be identified. Observations from the 20090503 event display similar characteristics as displayed in Fig. 3.4. The main difficulty in observing this phase is the noise produced by regional propagating crustal waves that bury PKiKP in broadband record sections, although other core phases PcP, ScP, and PcS are still visible along with their depth phases. Filtering between 1-3Hz produces the clearest view of PKiKP (Fig. 3.3B) as in other studies. Unfortunately, the Earth appears amazingly complicated at these frequencies and the observed PKiKP amplitude varies spatially. To obtain properties of ICB, one must evaluate and eliminate signal contamination when the signal propagates along the paths crossing both the upper-mantle and core-mantle-boundary.

Because our analysis involves noisy data, it becomes difficult to process. We want a method that is both flexible and can be used in stacking where alignment becomes a major issue. It appears that the Multi-Path Detector (MPD) which was initially proposed for longer period studies(Sun and Helmberger 2011), is effective in this case. This method simplifies the banana-split approximation (Helmberger and Ni 2005), and assumes the observed complex waveform is a superposition of two simple waveforms due to multi-pathing. The two simple waveforms have the same shape, but their amplitude ratio and relative time shift ΔLR are adjustable parameters and are searched to maximize the fits to the data, see Fig. 3.5. Maps of these parameters (ΔT , ΔLR , and amplitudes) are presented in Appendix A with respect to PREM. With these parameters, we can stack the nearby seismograms, and investigate both the amplitude and ΔT in stacking results. Boot-strapping procedures can be used to

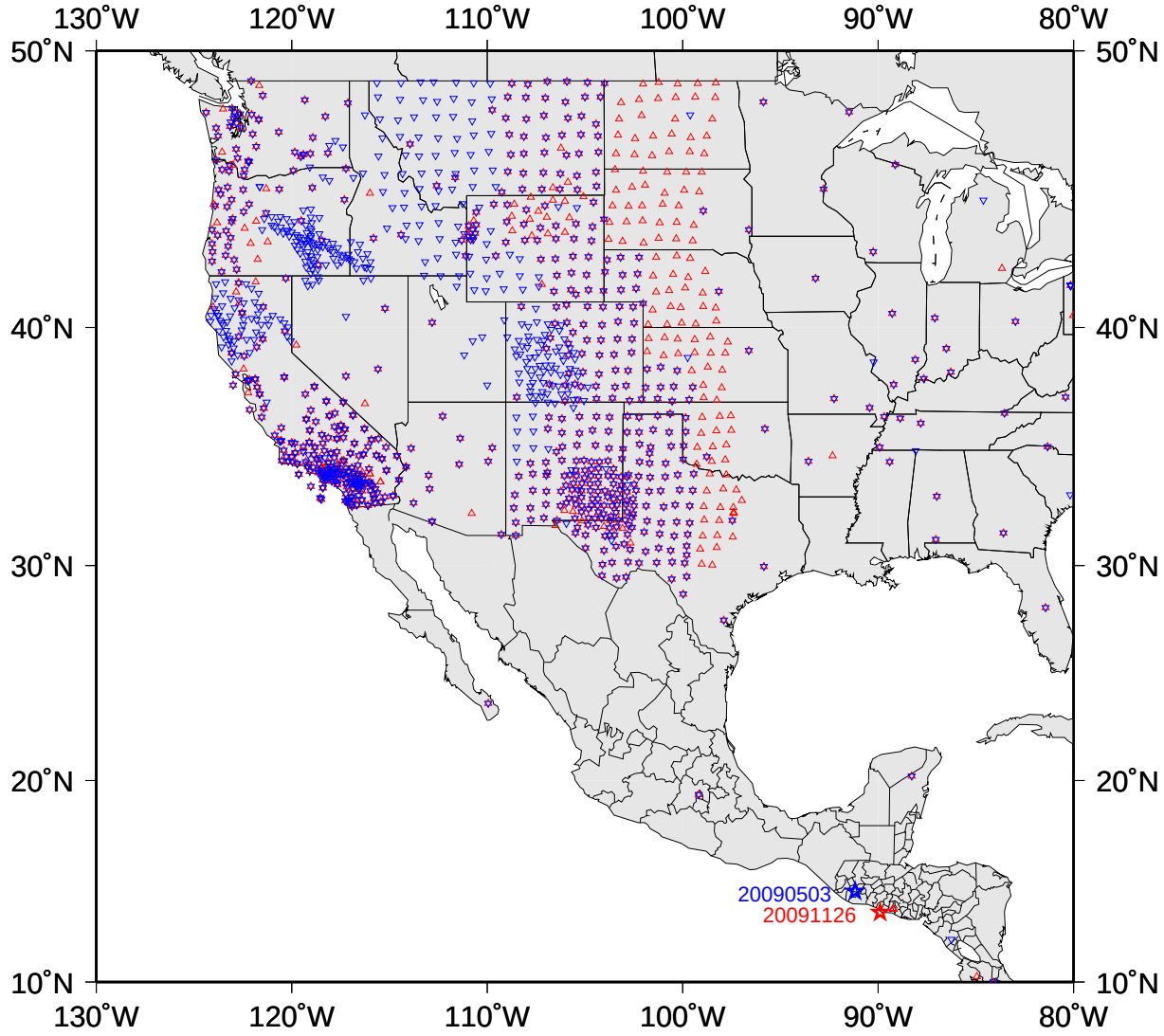

Figure 3.2: Locations of two events (20090503 and 2009112, denoted as stars) and their corresponding USArray recording stations indicated by color.

assess the stack reliability as applied in Sun et al. (2013).

Amplitudes between PKiKP and PcP display shotgun patterns with nearly an order-of-magnitude scatter which changes between the two events, see Fig. 3.6. Note that the distance plot for event 20090503 shows the predicted behavior for 1D model where the ratio grows with distance as predicted in other studies(Cummins and Johnson 1988), see Appendix B for predicted amplitudes from PREM. The level of scatter in Fig. 3.6 is similar to other studies which clearly display the difficulty of using the (PKiKP/PcP) ratio as discussed in Tkalčić et al. (2010). In the next section we will discuss some advantages of using a pair of events to help separate shallow effects from deep effects.

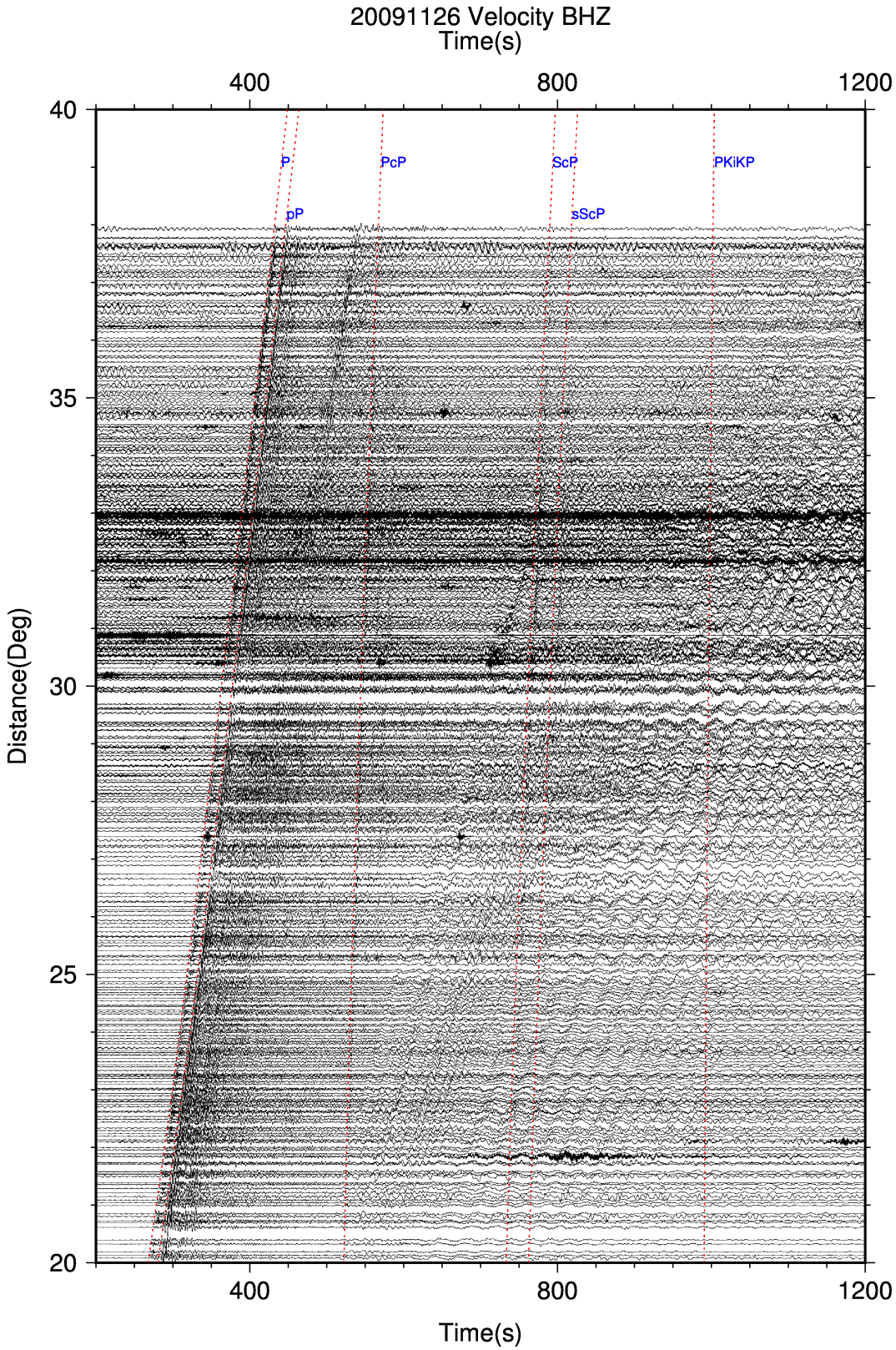
20091126 Velocity BHZ
Time(s)
400
800
1200
40
35
30
25
20
P
pP
PcP
ScP
sScP
PKiKP
Distance(Deg)
400
800
1200
Time(s)

(a) Broadband

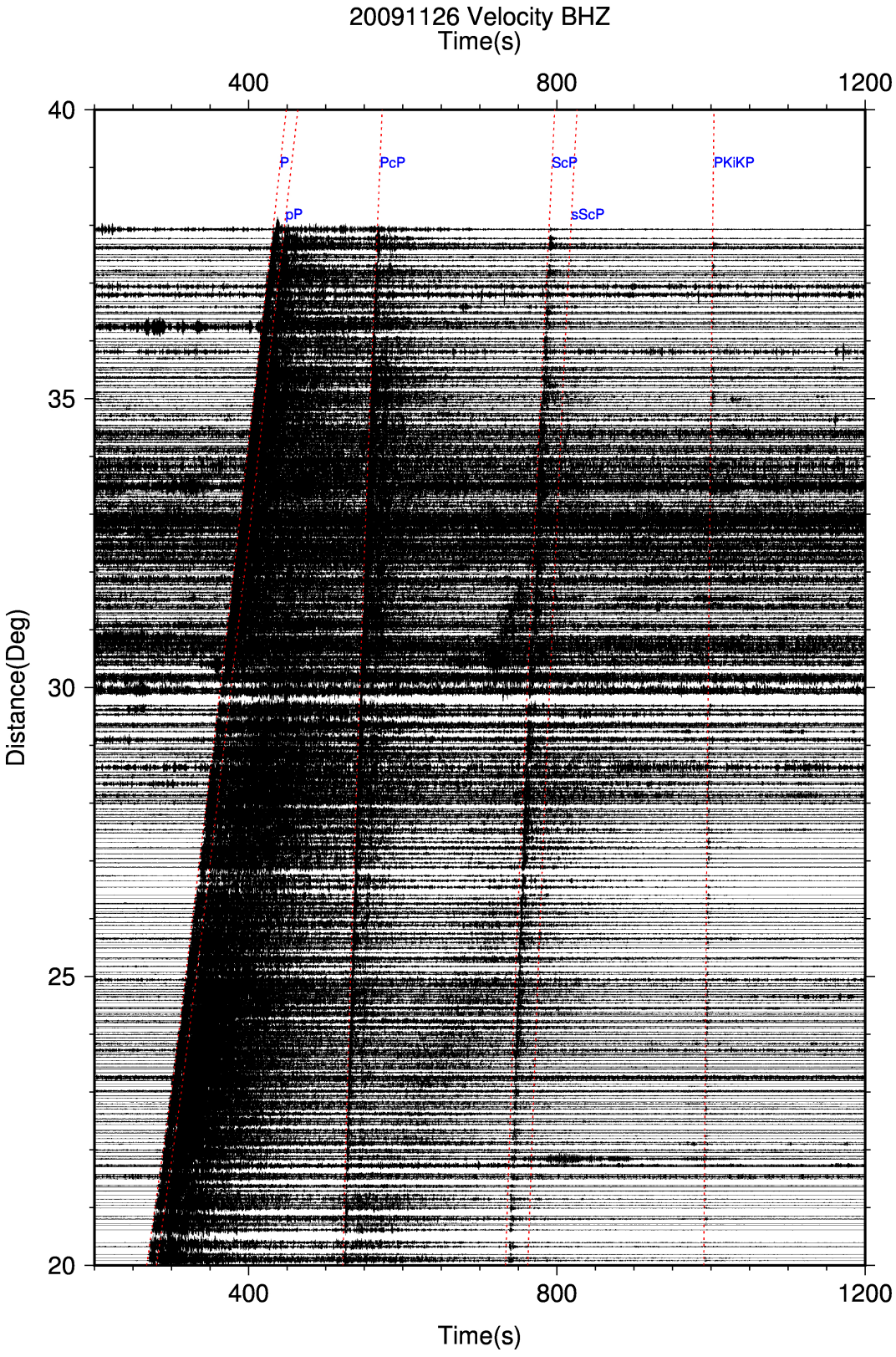

(b) Bandpass 1 to 3Hz

Figure 3.3: (A) Broadband velocity seismogram for 20091126 event plotted as a record section. (B) Same section but applying bandpass filter from 1 to 3 Hz to enhance the PKiKP phase.

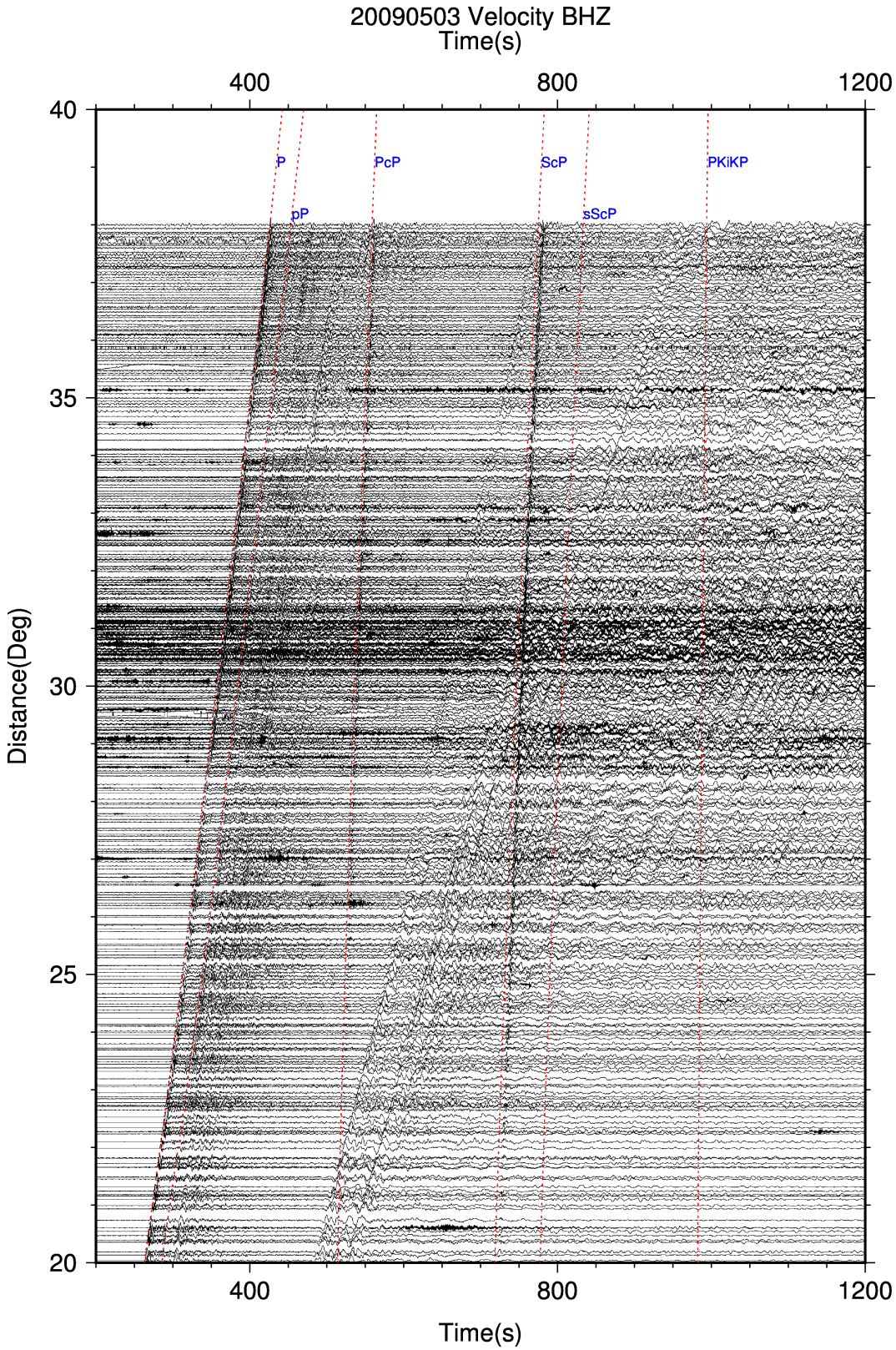
20090503 Velocity BHZ
Time(s)
400
800
1200
40
35
30
25
20
P
pP
PcP
ScP
sScP
PKiKP
Distance(Deg)
400
800
1200
Time(s)

(a) Broadband

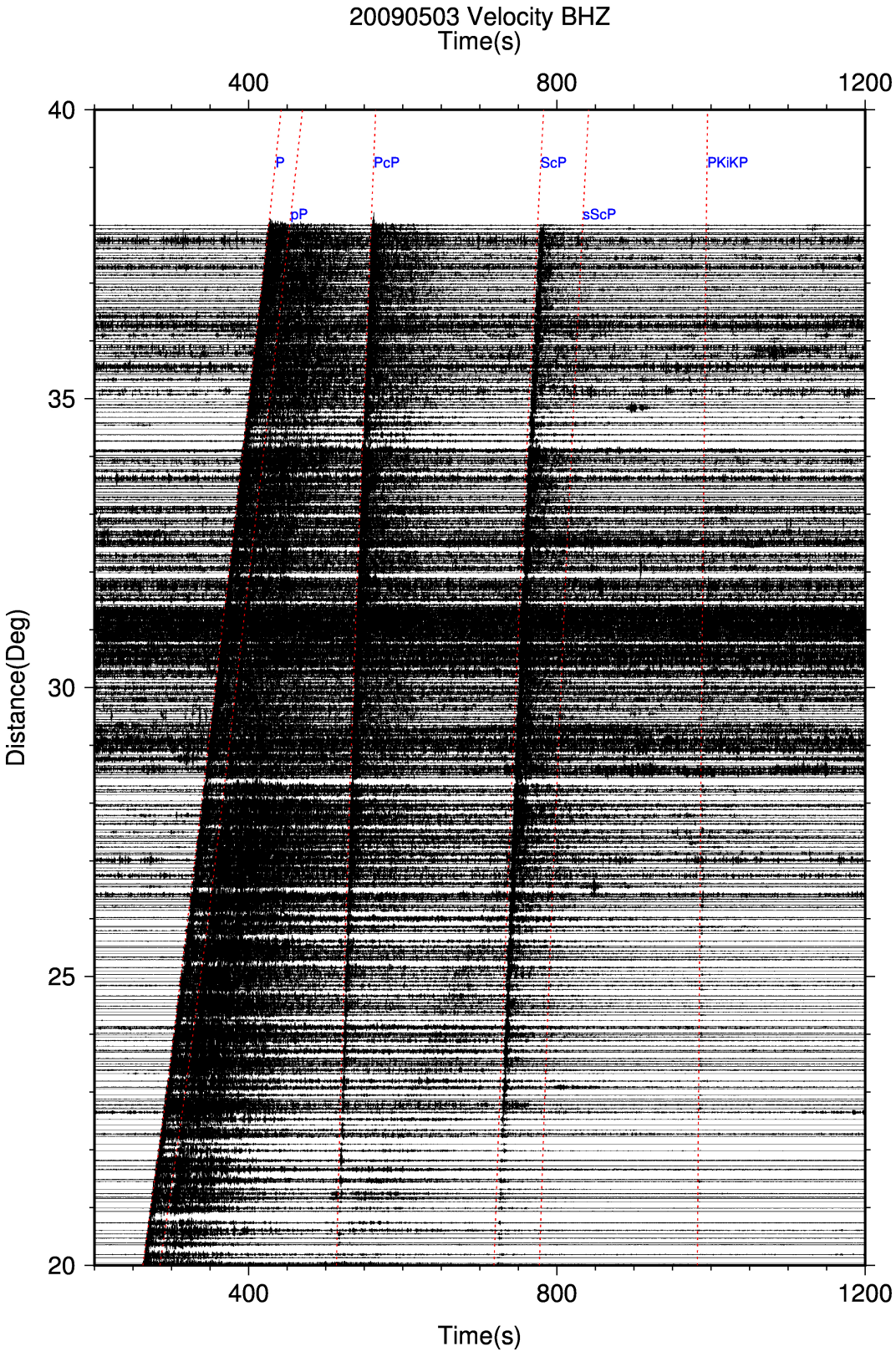

(b) Bandpass 1 to 3Hz

Figure 3.4: (A) Broadband velocity seismogram record section for the 20090503 event. (b) Applying bandpass filter from 1 to 3 Hz enhances the PKiKP phase.

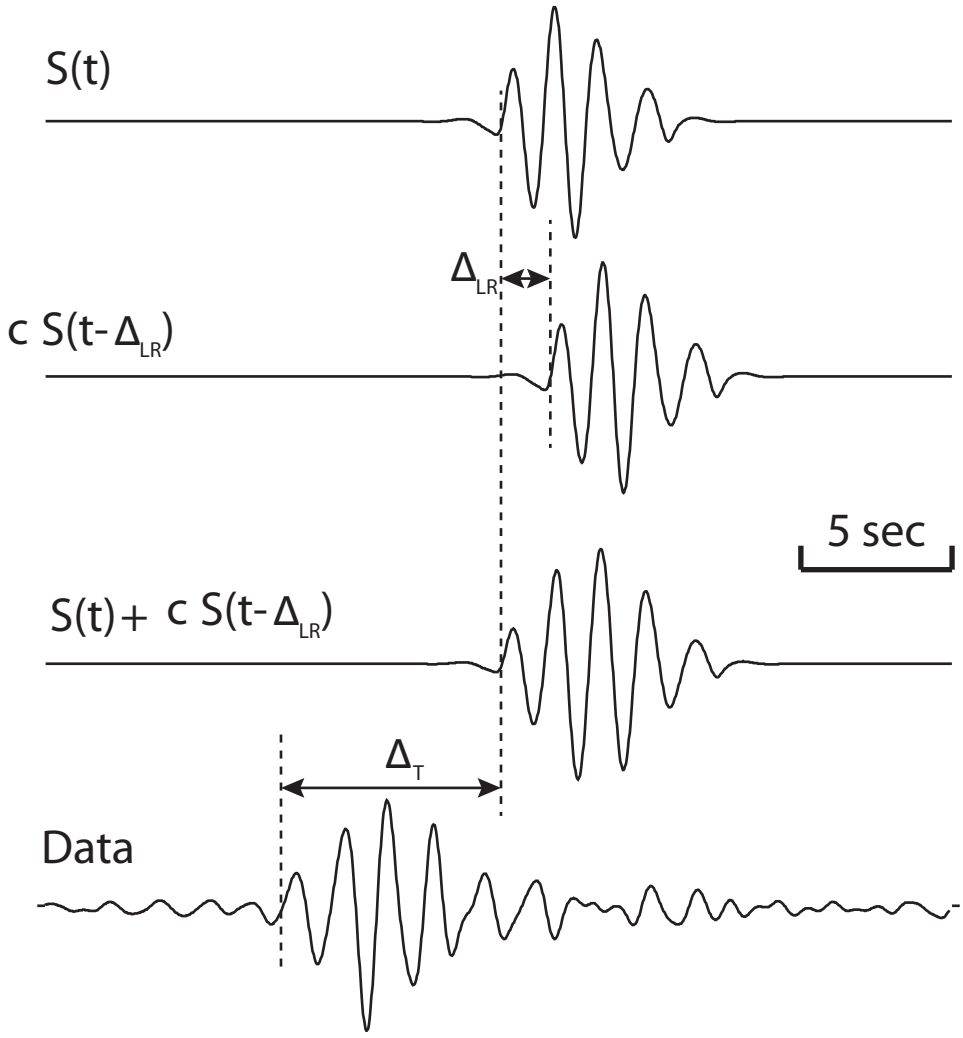

Figure 3.5: Illustration of the multi-path detector (MPD) method on high frequency data. The top trace $S(t)$ is the prediction from reference model, i.e. PREM. The MPD depends on the choice of the source time function (STF). We first examined the data and picked the record with the simplest waveform, which was then used to cross-correlate and align other data at distance range $18°$to $23°$. Then we stacked those aligned data which has high cross-correlation coefficient to form the STF. The bottom trace shows the data, which is more complicate than the S(t). To simulate the data, we add the scattering contributions (same waveform as $S(t)$, but with an adjustable time shift ΔLR and adjustable amplitude factor c) to the reference synthetic. The best cross correlation between the data and simulated waveform is searched. The time difference between the simulated waveform to the data is defined as ΔT.

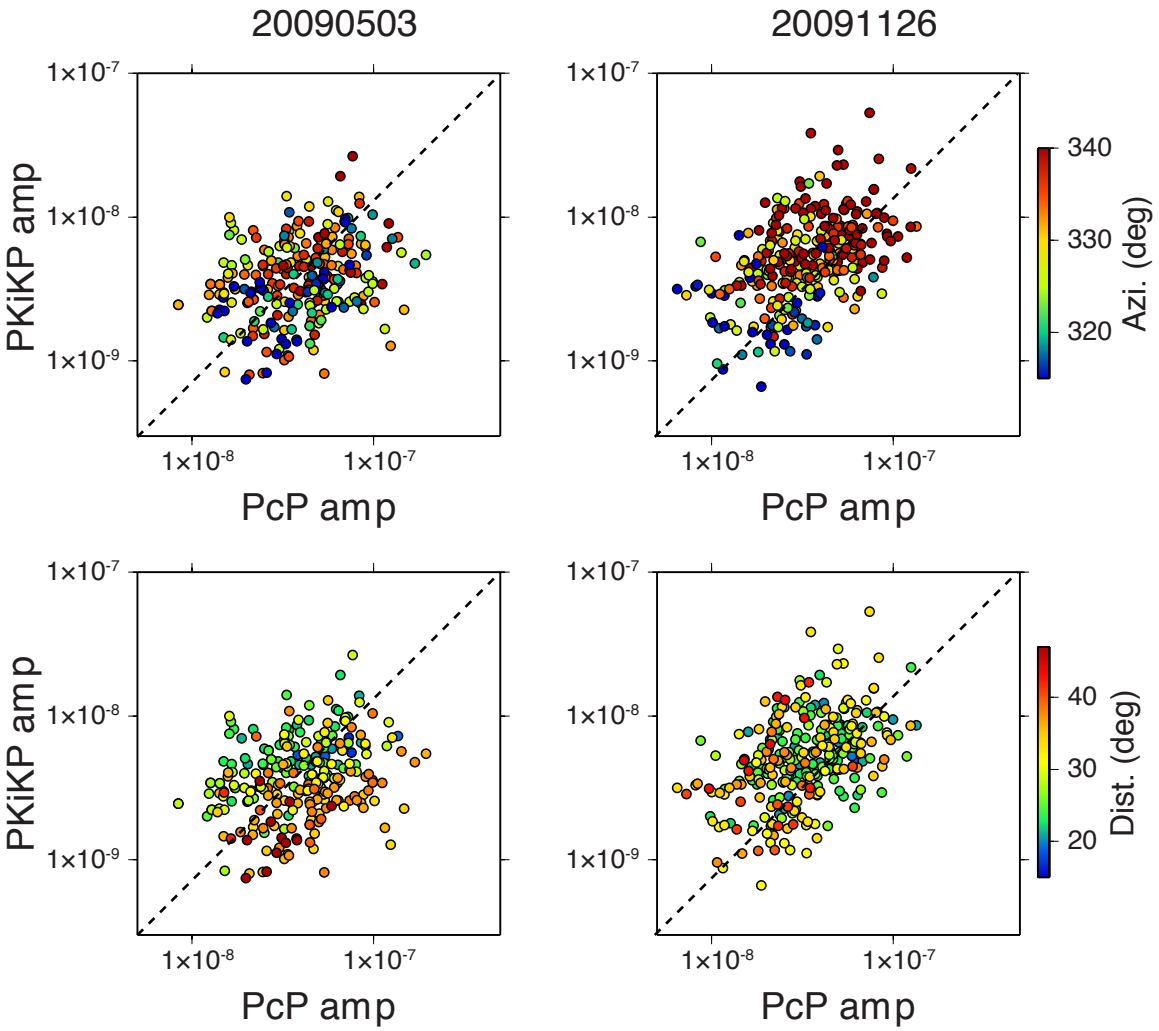

Figure 3.6: PKiKP amplitude versus PcP amplitude. The symbols are color-coded by azimuth in the top row and distance in the bottom row. Note the strong scatters in the amplitudes for individual station records. Also note that the event 20090503 behaves more like PREM with the PKiKP/PcP ratio having a smaller values at large distance.

3.3 Evidence for deep earth effects

We begin this section with a numerical simulation (see Fig. 3.7) assuming an upper-mantle scattering model proposed by Tkalčić et al. (2010) but with a point source, see Appendix B for details. This model is not unique in that we do not know where these scatterers are located but such a model does generate strong variation in the amplitude ratio. Note that the amplitudes between the two phases are out-of-phase and greatly enhance the ratio variation. Thus, large ratio variation is easily achieved with this level of scatterers, as in Fig. 3.6, making the error-bars on estimating ICB density jump from ratios of individual stations huge. However, the differential behavior between two events recorded at the same station is still useful for correcting receiver effects. Note that the PcP ray paths for the two events in Fig. 3.7 are very near each other, so were for PKiKP ray paths. Here, the scatterers are probably stronger than for the real earth, but even so the ratio of individual phases between two events are not affected much, especially for PKiKP phase.

In short, analyzing these two nearby events is especially useful, as discussed above, to evaluate how much variation is due to deep Earth structure and how much is due to receiver structure. Thus, we select stations which recorded clean (signal noise ratio larger than 2) PcP and PKiKP phase for both events, as displayed in Fig. 3.8, aligned on the predicted PREM travel times. Generally, for each event the ratio (PKiKP/PcP, denoted as R) is quite variable as noted earlier. However, on average this ratio for the first event seems to be similar to the ratio for the second event. This implies that at these stations, amplitude variations are mostly controlled by the receiver portion of the path as demonstrated by Tkalčić et al. (2010). The observation also suggests that the individual PKiKP/PcP ratio may not be good for studying ICB because of upper mantle scatterers. Also note that ratio of PcP amplitude between the two events effectively eliminates upper mantle influence, but still shows scatter, indicating CMB is not simple.

The receiver side effects cannot be the only reason for the amplitude variation. The ratios for the two events are displayed in maps view in Fig. 3.9. Note that there are many neighboring stations with rather large differences. For example, if we examine more closely the ratio of the data set in the lower left panel of Fig. 3.9, we see that there are distinct patterns, i.e., the apparent boundary along the New Mexico-Texas border. A particularly good example of rapid change is the comparison of some of stations in the southern California (CI array). Note that the ratio displays a north-south linear pattern (lower right panel of Fig. 3.9). A close comparison of

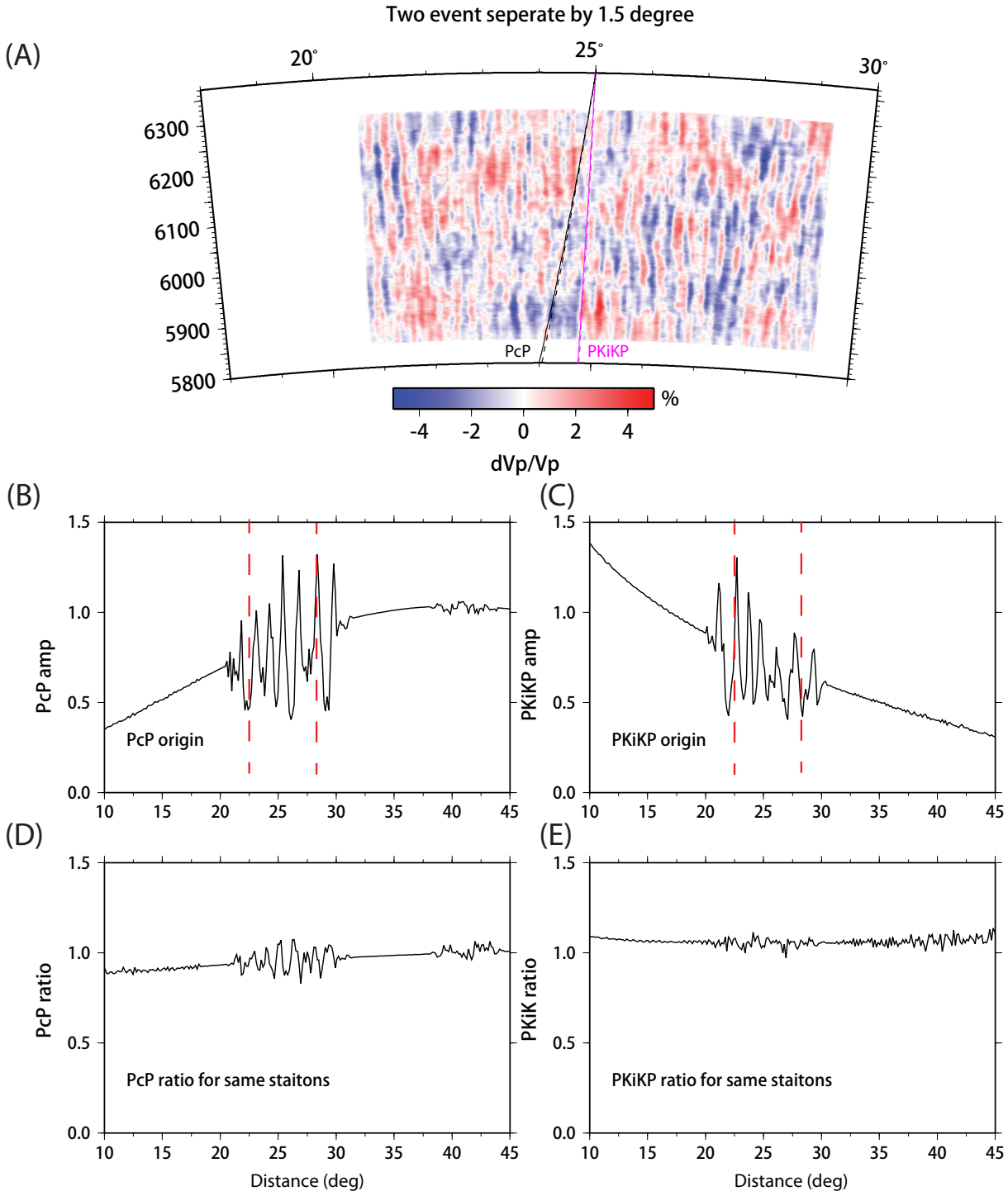

Figure 3.7: Simulation of effects caused by upper mantle heterogeneities on receiver side at the same stations for two nearby events. (A) Strong upper mantle heterogeneities are included in the model. Although the two events are separated by $1.6°$, both PcP (black) and PKiKP (magenta) ray paths (solid and dash lines) are very close in the upper mantle. The upper mantle heterogeneities introduce strong amplitude variations on both (B) PcP and (C) PKiKP. The (D) PcP ratios between two events for the same stations are relatively stable, so were for (E) PKiKP ratios. These ratios can be used as an efficient way to remove possible strong upper mantle effects on the high frequency data and isolate deep earth contribution.

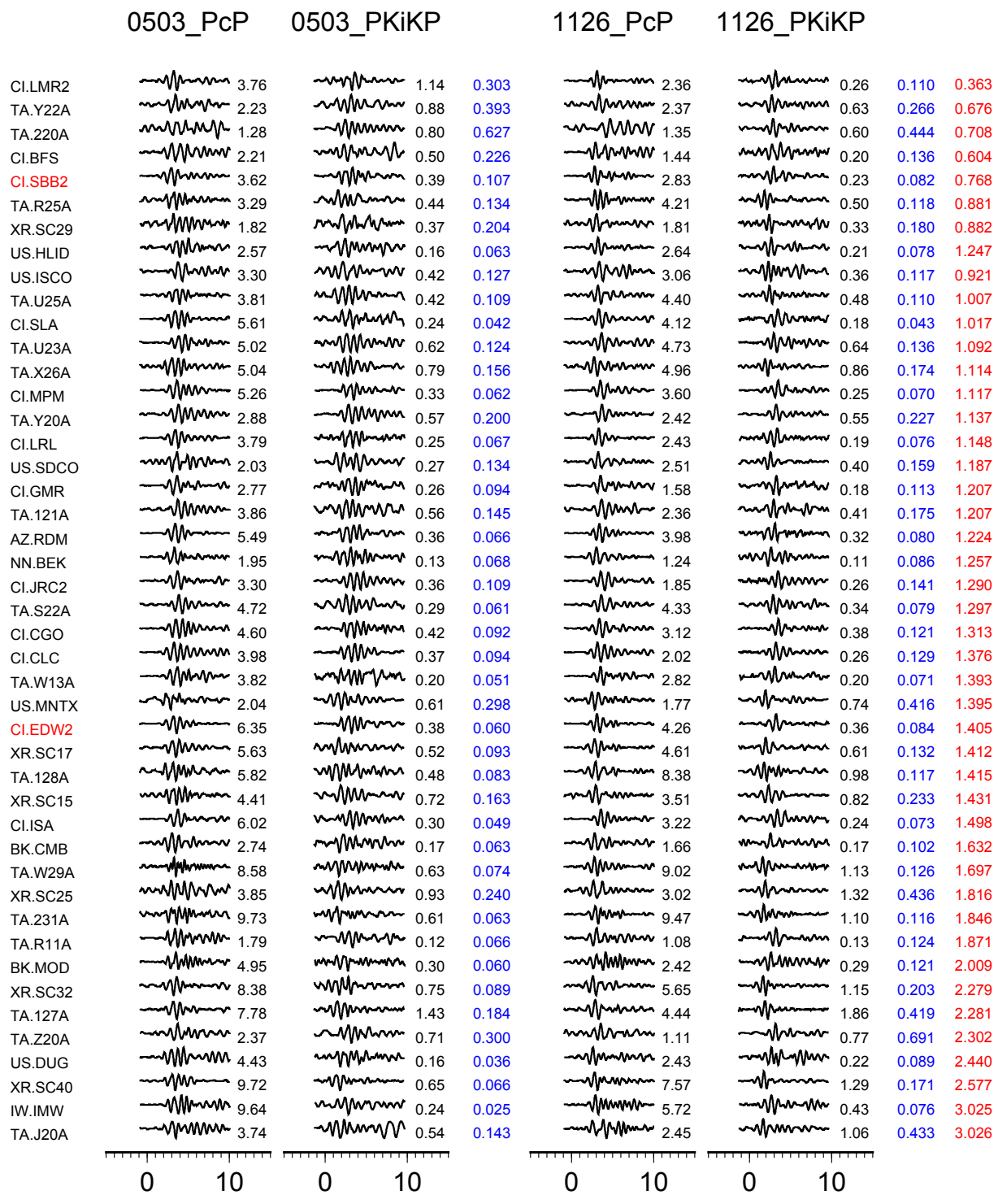

Figure 3.8: Selected displacement seismograms aligned on PREM arrivals, with SNR>2 at 1 to 3Hz, for both PcP and PKiKP phase and recorded by both events. The black number shows the maximum absolute amplitude for each trace (×1E-8 m), the blue number shows the ratio between PKiKP and PcP for each event, and the red number indicates the ratio of the two blue number. Seismograms are ordered by the red number.

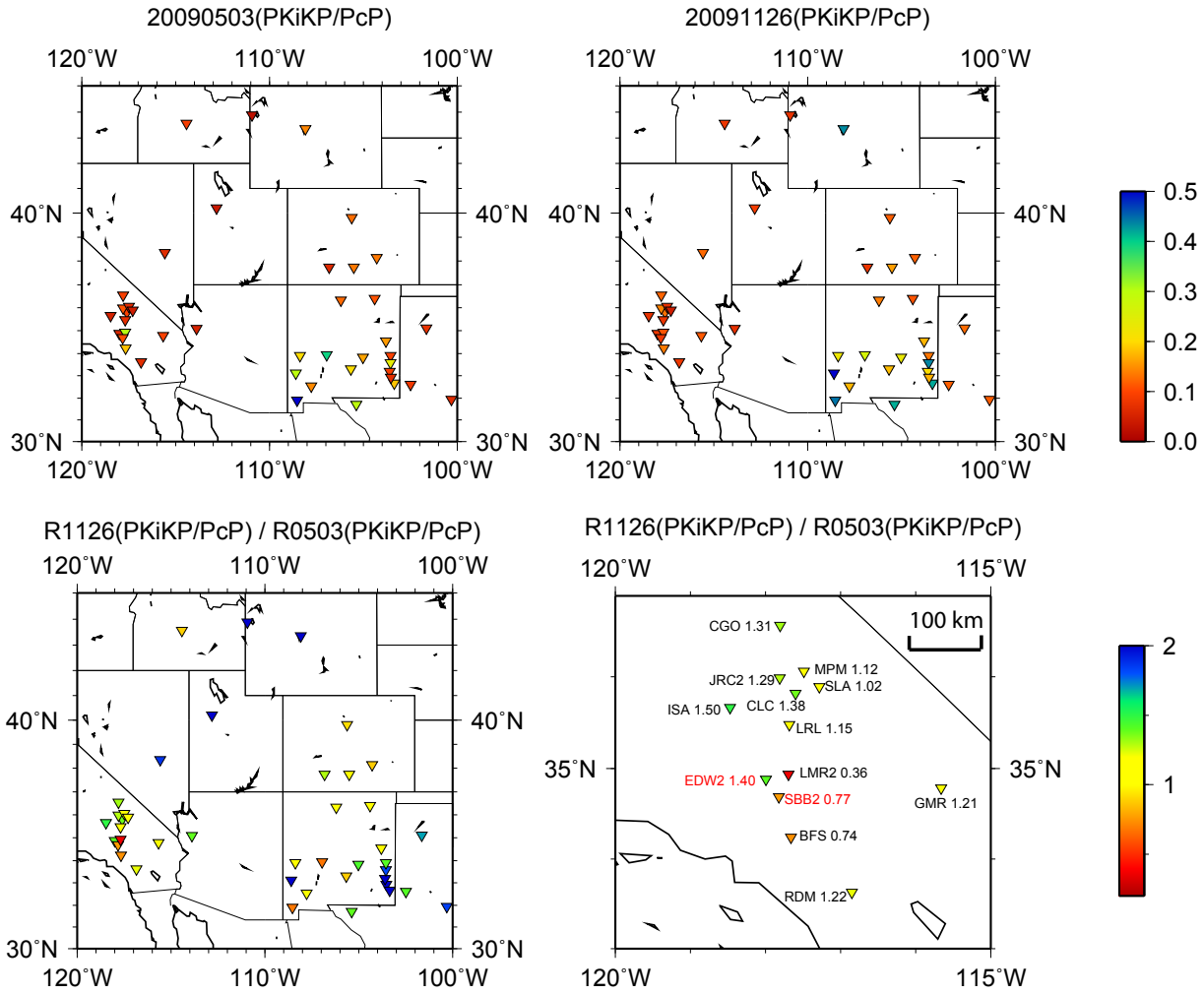

Figure 3.9: In map view, top two panels show the PKiKP/PcP ratio for the two events, and bottom left panel shows ratio of ratio between the two events, with a zoom-in of CI array in bottom right panel. Note the jump of ratio of ratio at relatively close CI stations.

two stations (EDW2 and SBB2) along this boundary indicates a jump by a factor of two within a horizontal distance of less than 50 km, see Fig. 3.10 for details. Such a change is difficult to explain without very sharp features in the deep earth, as demonstrated by the numerical experiment in Fig. 3.7. Thus some variation of PKiKP amplitude does provide some information about deep structure.

In summary, there is evidence for amplitude variations at all boundaries including the CMB and ICB. In the next section, we present some modeling results that suggests the ICB boundary can still be investigated using the above data-set.

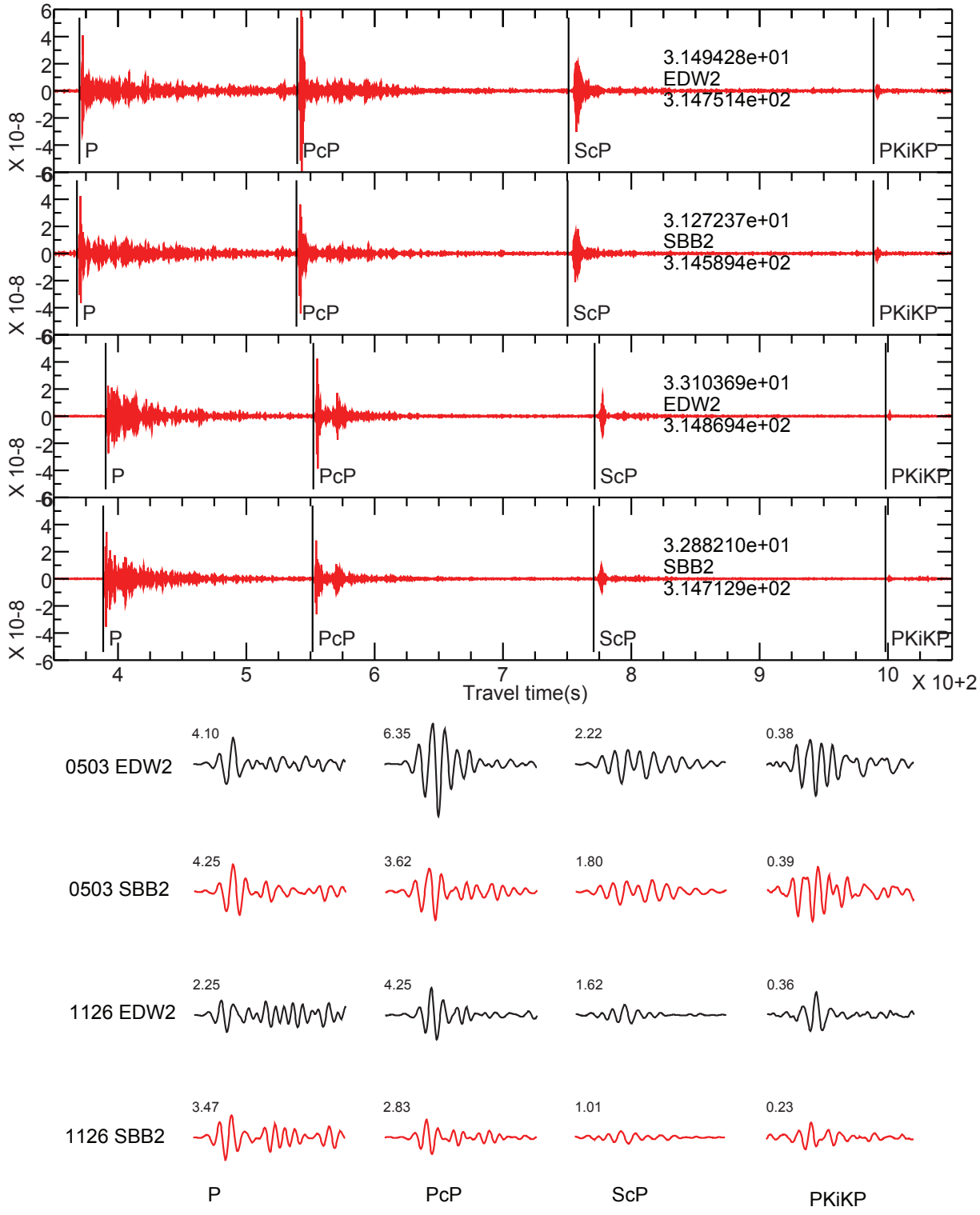

Figure 3.10: A case where PKiKP/PcP ratio of ratio has a factor of 2 difference between nearby stations, see Fig 8. Seismograms (1 to 3 Hz) of each phase are displayed in the lower panel. Black number indicates maximum absolute amplitude for each phase window.

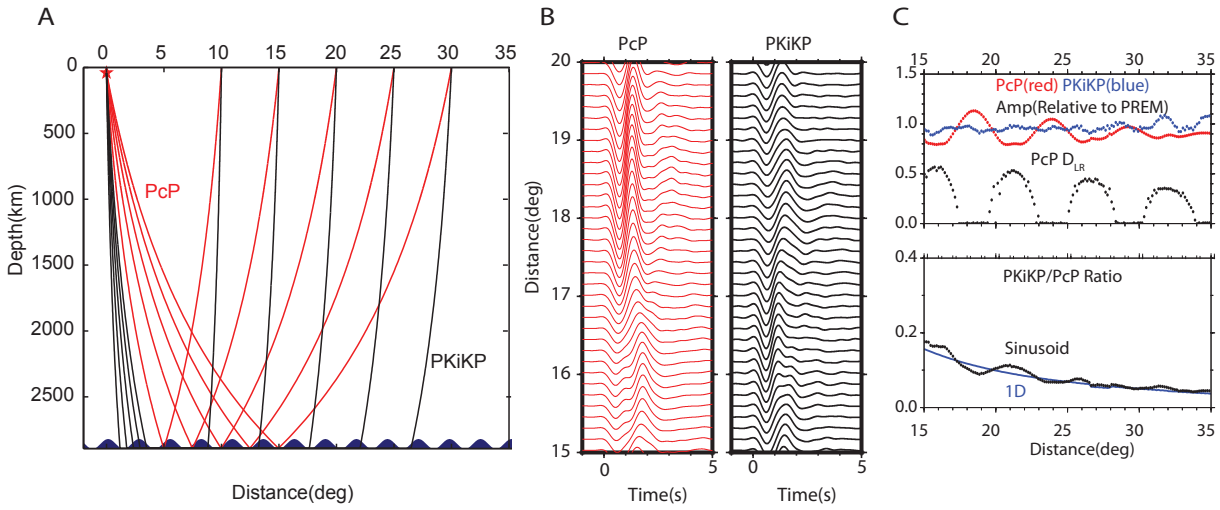

Figure 3.11: Simulation of effects of the CMB structure. (A) The model includes sinusoids of low velocity structure at the CMB with the width of 100 km and the height of 100 km. Inside the low velocity structure, the Vp anomaly is -5%. Note that the PcP (red) and PKiKP (black) sample very different parts of the low velocity structure. (B) The synthetics of PcP and PKiKP for the model in (A). The low velocity structures at the CMB have much less effect on PKiKP waveforms than PcP waveforms. The PKiKP amplitudes (blue line) in (C) are almost constant. In contrast, the amplitudes of PcP (red line) display greater variations, where large ΔLR (black line) values correlate with smaller amplitudes. Thus, the PKiKP/PcP ratio is mainly controlled by the variations in the amplitude of PcP in this model.

3.4 Modeling Deep Structure

In the previous section, we discussed how the upper mantle path effects can seriously interfere with the PKiKP/PcP ratios, especially approaching the receivers. One way to reduce the upper mantle effects is by stacking nearby traces. We will discuss this later, but first we study the effects of CMB and ICM structure on the PKiKP phase.

We assume a wash-broad pattern anomaly at the CMB, see Fig. 3.11. The 1D ray paths (after earth flattening) for the two phases are displayed, along with synthetic waveforms from 15° to 20°. Note that the structure focuses PcP energy from 17° to 20° (concave upward) and defocuses (upward bump) near 15° as displayed in Fig. 3.11B. In Fig. 3.11C, the MPD result shows the good correlation of PcP amplitude with multi-pathing time (ΔLR), where the larger the splitting the smaller the amplitude. In contrast, the PKiKP phase is less affected and the PKiKP/PcP ratio is controlled by PcP as shown in the lower panel of Fig. 3.11C. This test demonstrates that it is relatively easy to change both the timing and amplitude of PcP without significantly changing PKiKP by having structures at the CMB.

But the simplest way to change PKiKP may be by adding topography to the ICB as pointed out by Dai et al. (2012). For example, they examined the effects of inserting a box-like structure roughly 14 km high, 3° wide, with properties of the inner core (Fig. 3.12, first model). This feature produces a multi-pathed PKiKP, one from the top of box (precursor) and one from the original ICB coming from each side. Their relative strength depends on geometry with the strongest precursor occurring for the ray sampling near the center of the box. The precursor becomes small (in the noise) for box widths less than about 50 km, but still can affect the amplitude of PKiKP as displayed in Fig. 3.13. Reducing the height of the box to 4 km (Fig. 3.12, , second model) brings the two pulses together. Note in this case that, the amplitude of PKiKP is similar to 1D. However, if we let the properties of the box change gradually from outer core material on top to inner core material on bottom (Fig. 3.12, , third model), the PKiKP amplitude can easily change by factors of two.

3.5 Results

Stacking nearby traces reduces small scale scatter, which is mostly due to upper mantle. Fig. 3.14 demonstrates such a scenario. We assume a target ICB anomaly (a 10 km high 1°wide Gaussian shape anomaly) with material gradually changing from that of the outer core to that of the inner core, which appears to be useful in explaining our data, as shown later. Synthetics for three models and one stacked record section from 10° to 20° are displayed below. PREM synthetics are on the leftmost. The column next displays the effect of adding the ICB bump, which changes the PKiKP amplitude. Then adding scattering in the upper mantle produces a great deal more variation. Finally, in the rightmost record section, we stacked the third record section over a 2° window, which greatly reduces the upper mantle scattering effects. More stacking produces the same decay as PREM but is less revealing in recognizing features with rapid amplitude drops near 20°.

Based on these numerical experiments, we returned to the USArray dataset and stacked over a moving window of 1.5° which generally included over 8 stations. The results are displayed in Fig. 3.15. Here, the data are aligned on the ΔT shifts of each trace relative to the reference arrival time. Bootstrapping analysis as discussed in Sun et al. (2013) indicates that the stacking is stable. Generally, stacking about five stations is needed to produce a stable measurement in that neighboring stacks are quite similar. The station coverage for the two PASSCAL arrays contains many more traces as indicated in Fig. 3.15. The variation in amplitude is given in color

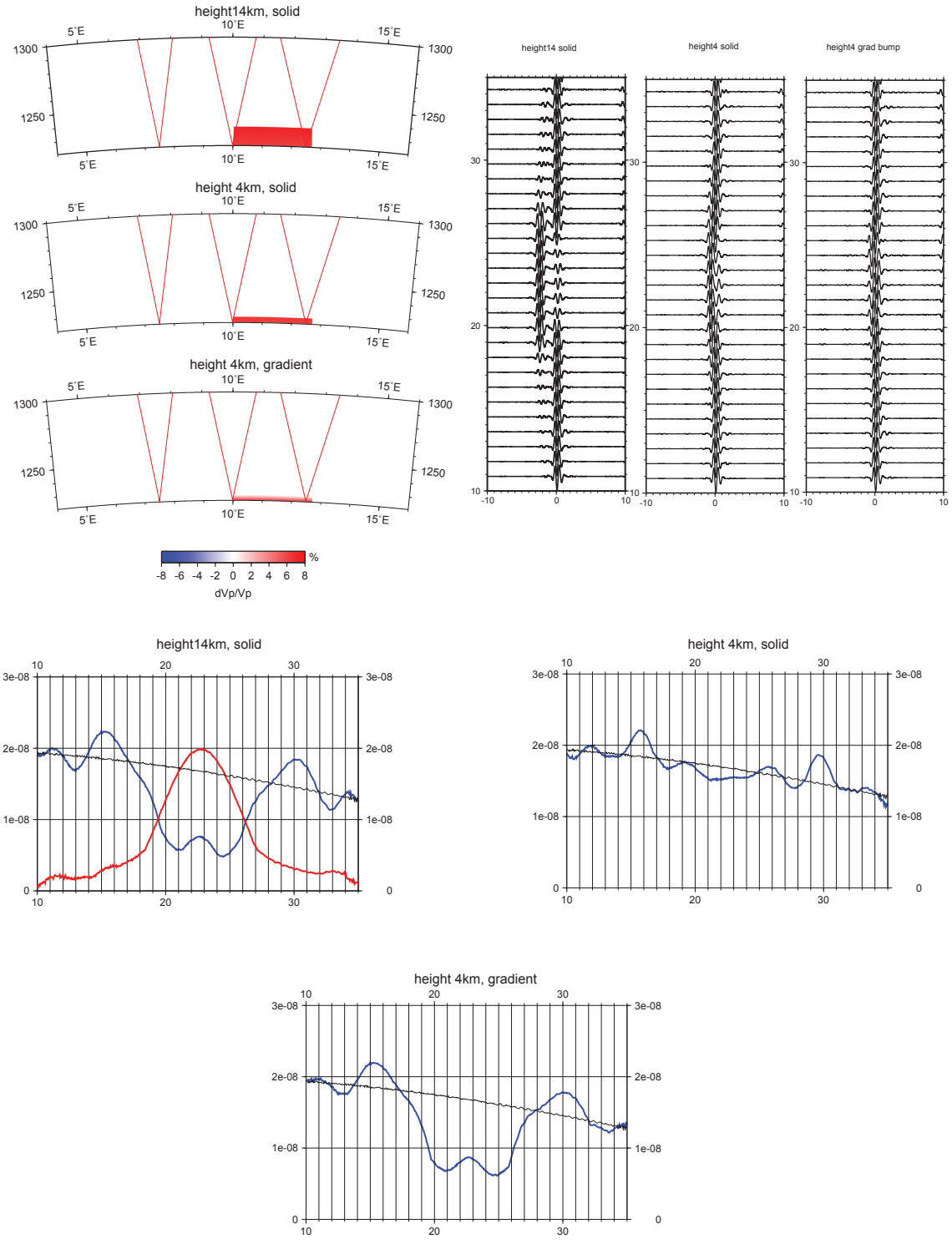

Figure 3.12: Three models at ICB, where the top one contains anomalies 2.8° width and 14 km high with inner core materials property, the second one is the same as the first one except a 4km height is used, and the third one is similar to the second one except now the anomaly is a gradient transition between outer core material to inner core material. The seismograms of PKiKP for the three models are shown on the left, and the amplitude plots are shown below. Note that the first model PKiKP has two arrivals, one corresponding to reflection from the top of the anomaly (precursor), shown in red, while the other is the non-optical ray reflections from ICB outside the anomaly, shown in blue. The amplitude for 1D reference model is shown in black.

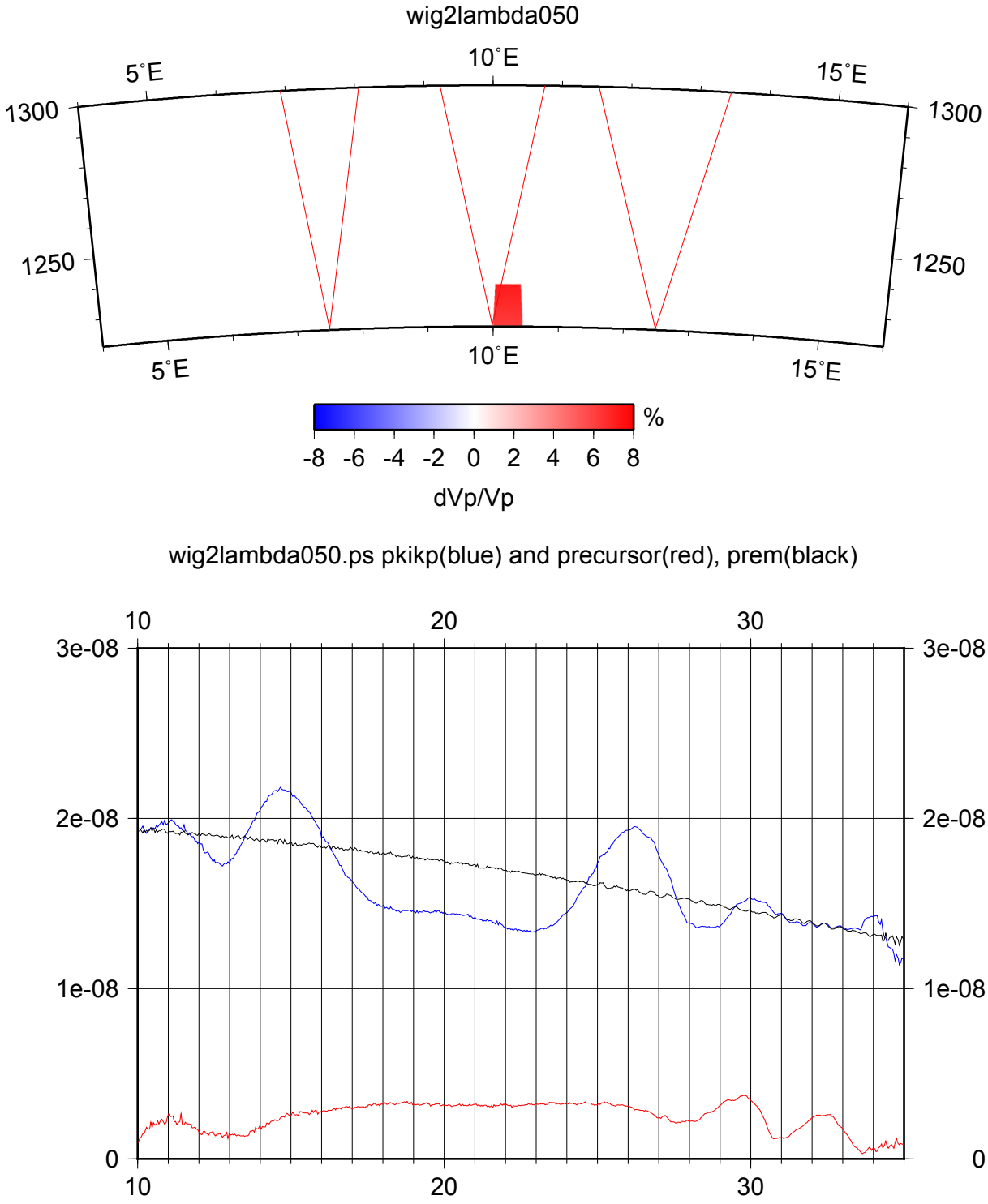

Figure 3.13: A model similar to the first model in Fig. 3.12, but with heterogeneity at ICB of 14 km and about 0.5 degree width.

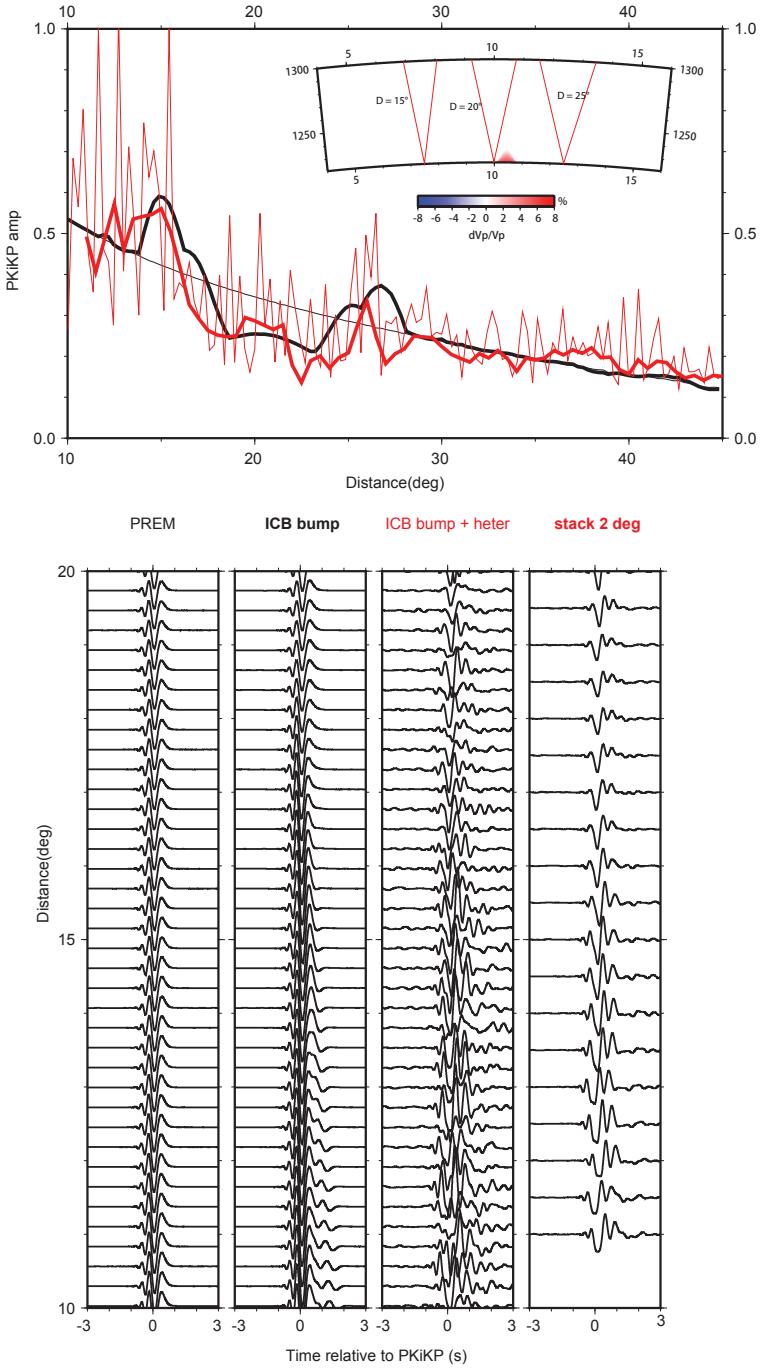

Figure 3.14: Testing the stacking procedure on simulated waveforms, where the influence of upper mantle heterogeneity is greatly reduced. Three models are considered. The first one is 1D PREM, the second one added a ICB bump to the first one, and the third model added upper mantle heterogeneity to the second model. The recorded PKiKP phase is shown on the left three record sections, and stacking of the third record section is shown in the rightmost. The amplitude of the four record sections is displayed as thin line (PREM), thick dashed line (ICB bump), thin dashed line (ICB bump + heterogeneity), and red dashed line (stack every 2°), respectively.

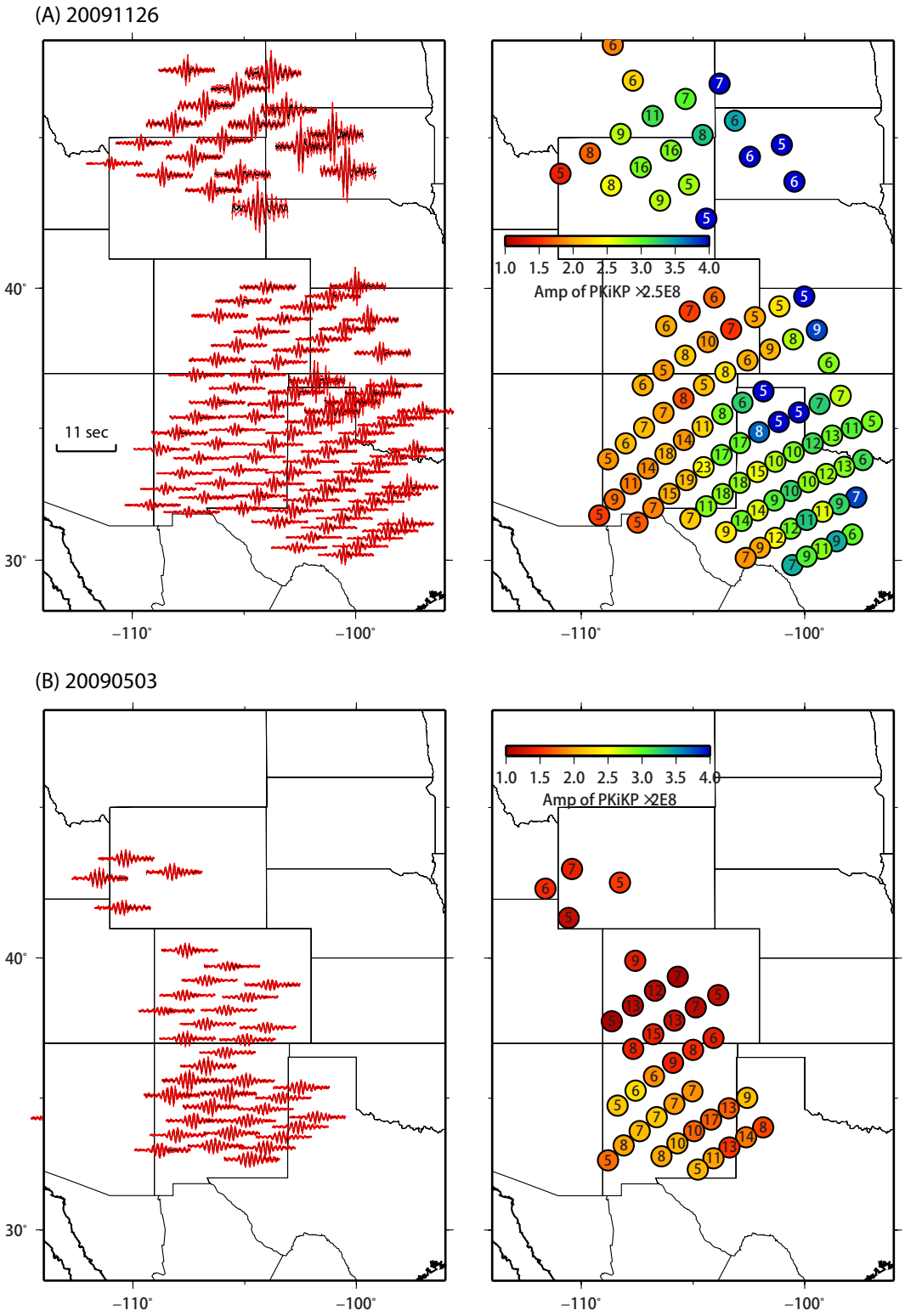

Figure 3.15: Stacked PKiKP records and their amplitudes for events (A) 20091126 and (B) 20090503. Every waveform in the left column is the stacked record for the data within a circle having the radius of 120 km. A bootstrap-resampling algorithm was applied to generate the stacked waveforms (black traces) and the waveforms with 95% confidence level are displayed in red. In the right column, the amplitudes of the stacked PKiKP waveforms are displayed in colors. The numbers inside the circle indicate the number of traces used in the stacking process.

where the strong difference in gradient occurs between the two events near the New Mexico-Texas border. Note that if this pattern was controlled by upper-mantle attenuation, both events would behave the same, which is not the case. Moreover, the amplitudes of PcP do not show such feature, which it should if the PKiKP pattern was caused by attenuation. The stacked trace amplitudes for PcP and PKiKP and their ratio are shown in Fig. 3.16, for two azimuthal windows 310° to 330° (western US) and 330° to 347°(Texas). Note that the amplitudes of PcP for Texas are behaving PREM-like while PKiKP (black) jumps up starting near 30°. Thus, the ratio of PKiKP/PcP becomes over a factor of two larger as well. Also, note the large difference in PKiKP between these events beneath Nebraska. If these patterns are controlled by the ICB, we should see a better match by simply projecting these dots downward as in Fig. 3.17. The combined data sets display a strong edge roughly along the heavy dotted line separating the two colors where the amplitude of PKiKP jumps by a factor of two to three. More data is needed to develop a clearer image but such behavior can be explained by a Gaussian bump containing a transition from outer core to inner core, as shown in Fig. 3.14, at the edge of this boundary.

3.6 Discussion

The enigmatic nature of PKiKP observability is well known and confirmed in this study where its detection is low except for a few events. As in previous studies, we assume that both PcP and PKiKP have similar source strength, and the rapid variation (small scale) in each is caused by scattering (Tkalčić et al. 2009). Our numerical experiments suggest several approaches of data processing to help circumvent some of these problems and separate features caused by the upper-mantle, CMB, and ICB.

First, we demonstrate that our earlier developed MPD analysis proves to be effective in processing PcP and PKiKP to obtain accurate and systematical measures of timing and amplitude. Whereas, processing long-period waveform data displays a clear relationship between amplitude and complexity (Sun and Helmberger 2011), short-period data does not. This feature is confirmed by numerical experiments on random media. But given the rapid changes in upper-mantle scattering, it proved difficult to find systematic variation in differential PKiKP-PcP times as in the Dai et al. (2012) study. However, changes in PcP and PKiKP amplitude due to deep structure can be detected either by measuring the ratio of amplitudes from two neighboring events or stacking. This approach works for numerical experiments with combinations of deterministic features at the core-boundaries and random scatterers near the Earth's surface. The data shows rapid changes in PKiKP amplitude that can be explained

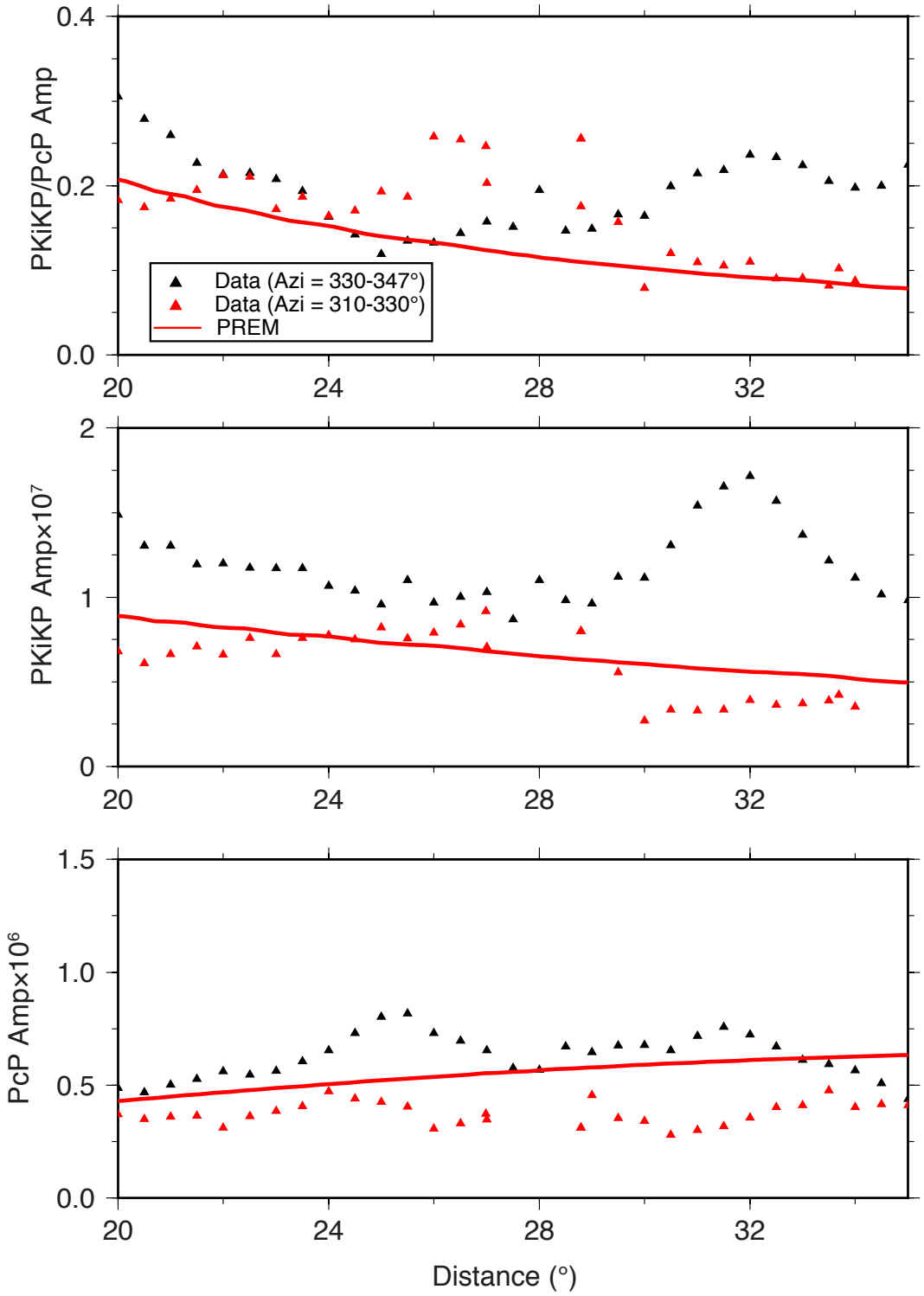

Figure 3.16: The amplitudes of the stacked records along the two azimuth bins for event 20091126. From the top to the bottom: PKiKP/PcP amplitude ratio, PKiKP amplitude, and PcP amplitude. The predictions from the PREM models are displayed as red lines.

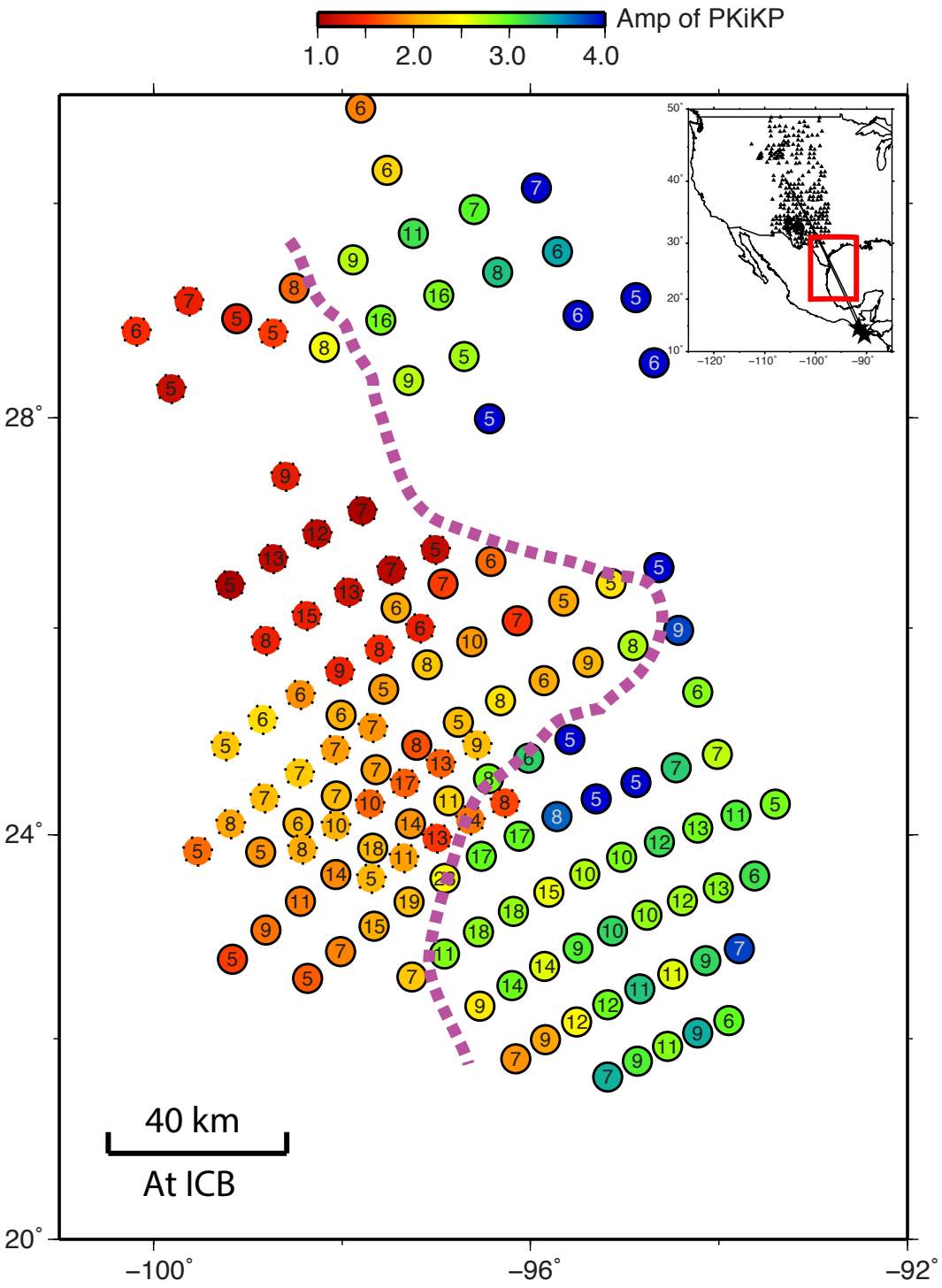

Figure 3.17: The PKiKP amplitude (normalized with respect to one station) patterns migrated to the ICB. The inset displays the map of the two events and stations. The solid circles are for event 20091126 and the dashed ones are for event 20090503. The numbers inside the circle indicate the number of traces used in the stacking. The thick magenta dash line separates the region with high amplitude (green/blue color) and low amplitude (red color), which indicates possible sharp transition occurring along this line at the ICB.

by gradational bumps on the inner-core with heights of several kms and lengths 1 degree horizontally, similar to that found along paths beneath the Banda Sea to Japan (Dai et al. 2012), and suggested by Cao et al. (2007). The latter paper addresses record sections of PKIKP and PKiKP (see Fig. 3.1), at distance of 135° to 140° for earthquake doublets recorded by the Yellowknife Array. They suggest that a bump on the ICB must be involved, and that this bump changes its position with time, i.e. Song and Richards (1996), and causes the observed differences.

Previous study reveals that PKIKP and PKiKP bifurcation are distinctly different between the Western Hemisphere and the Eastern Hemisphere, although the boundaries are not well sampled (Niu and Wen 2001). Timing differences of up to 0.5s with earlier bifurcations in the east and smaller PKIKP/PKiKP amplitudes are observed. While the average difference can be modeled well in 1D (Wen and Niu 2002), significant scatter (up to 50%) remains in any one record section. Note that the ray-paths are essentially identical in the mantle (see Fig. 3.1), so that this type of variation must be caused in the deep earth. Here, we present synthetic predictions for a simple Gaussian-shaped bump centered near the PKiKP bounce point. Surprisingly, synthetics show that this feature, at distance around 130°, shortens the timing separation between PKIKP and PKiKP just by a few tenths of second and slightly changes the amplitude ratio (see Fig. 3.19). Comparing typical anomalies at the ICB and CMB in Fig. 3.18, we can see CMB proves more effective in producing distortions of the PKP bifurcation at the level commonly observed as inWen and Niu (2002). In short, the role of CMB boundary complexity on PKiKP appears to be less important at small distances than that at large distance. Thus, to validate such fine-structure on the ICB, we need to sample both ICB and CMB with combinations of differential phases. This may be possible given the ever-expanded station coverage.

3.7 Summary

In summary, we used USArray data to study complexity of the ICB interface. Following previous efforts, we used two neighboring events method and local stacking method to suppress scattering from shallow receiver structure. We find numerical simulation is especially useful to help us understand where in the earth the complexities are likely to be produced. We found that local stacking of synthetics (> 5 stations with 2°) largely reduces receiver effects, even in case of very strong scattering, and then deep structure can be identified. The data was processed using this “rolling stacks” to generate a relative amplitude disk for each location and then migrated to

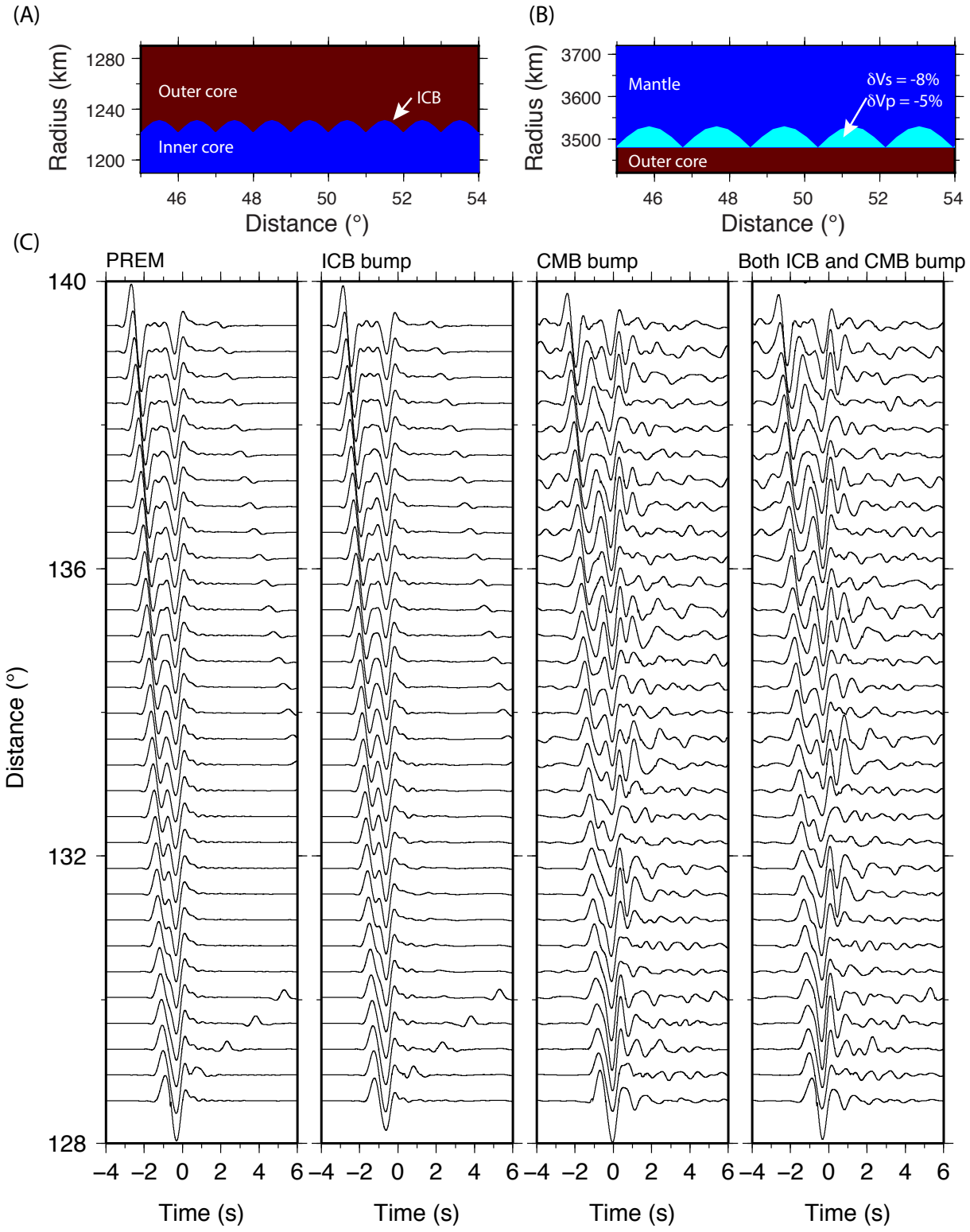

Figure 3.18: Scenario study for typical structures at CMB and ICB at PKiKP critical angle ranges. (A) and (B) display the implemented structures at core boundaries. From left to right, (C) displays synthetics for PREM model, model only with ICB structure in (A), model only with CMB structure in (B), and model with both ICB and CMB structures. Note the PKiKP is not particularly sensitive to the ICB structure as the CMB structure at this distance range.

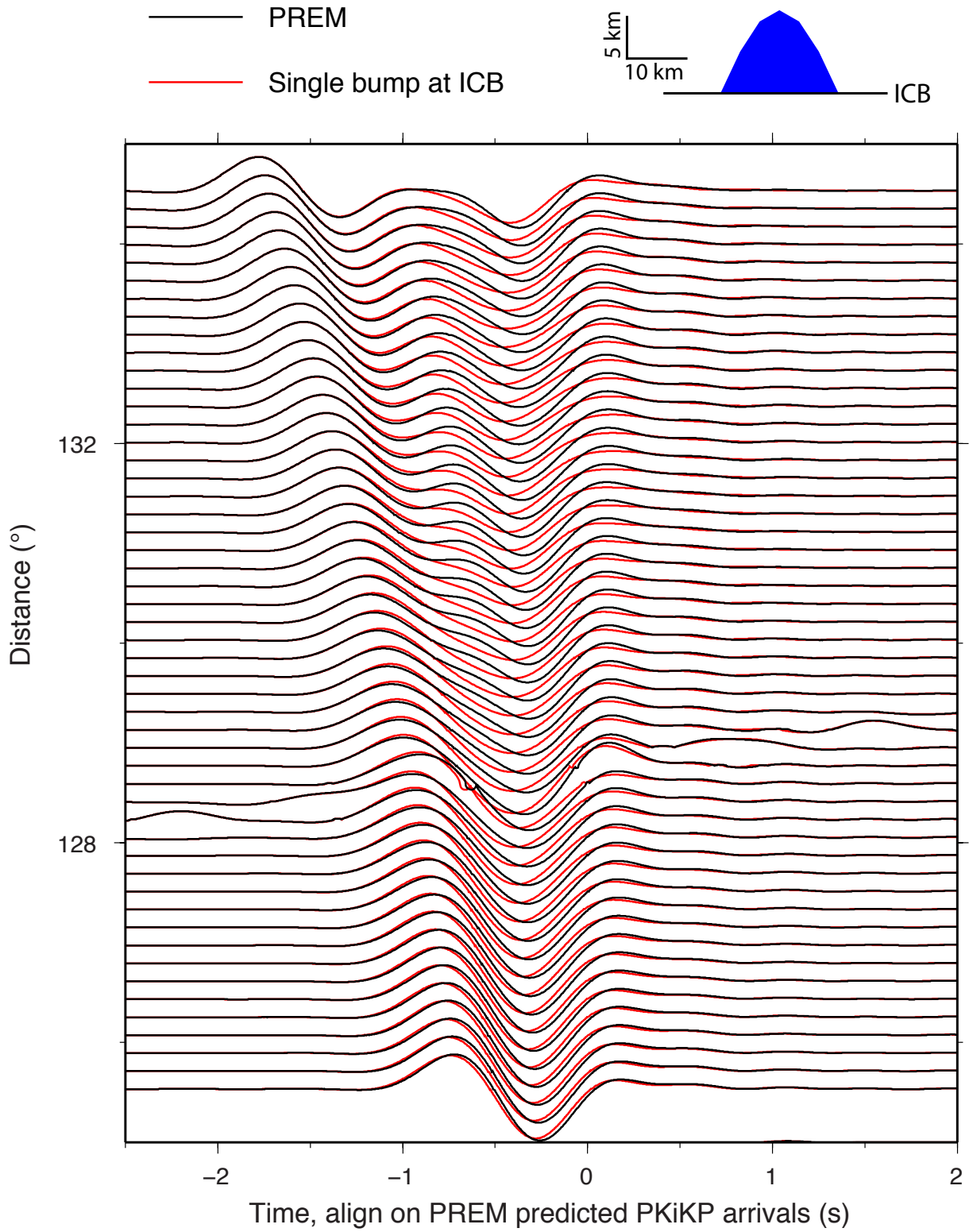

Figure 3.19: PKiKP and PKIKP synthetics for the PREM model (black) and the model with a single bump at the ICB (red). The bump has the width of 20 km (1 degree) and the height of 10 km with the inner core properties. The disruption near 128° is another secondary phase interfering with PKP system.

the ICB. Such a map at ICB shows sharp edges where amplitudes change by a factor of 2 to 3. Simulations of 2D structures suggest changes in the ICB, either a sudden increase of transitional thickness (a few km high of patchy mushy layer) and/or a sharp horizontal change in ICB elevation, can produce such effects.

Acknowledgements

We thank the Editor and two anonymous reviewers for their comments which greatly improved the manuscript. We also thank Brandon Schmandt for introducing us to these PKiKP data. Data were provided by the IRIS data center and Earthscope USArray. This work was supported by NSF EAR-1053064 and CSEDI EAR-1161046 at CalTech with partial support of D. Sun at USC under EAR-0809023.

Appendix A: Waveform Complexity Processing

The travel times ΔT are the most stable showing the relatively slow Western United States (WUS). Sun and Helmberger (2011) shows that at long-period, ΔLR maps generally correlate with the amplitude map, i.e., large ΔLR indicates strong multi-pathing and has low amplitude. Fig. 3.20 show that some features follow this pattern, but they do not match very well. It appears that the strong attenuation beneath WUS is an additional feature. These same complexities appear in the PKiKP maps but are not well correlated with what is observed in the PcP maps. Here, the overall amplitudes and ΔLR pattern agree better for PKiKP. Note that the amplitudes scatter about as much as in earlier mb bias measures used in studying attenuation(Lay and Helmberger 1983b). They found that while the western US has lower amplitude than eastern US with a bias δmb of 0.26 (corresponding an average amplitude difference of 2), any one station sampled in either region can differ by this amount. Here is a much larger sample but generally in agreement. The average jump in S-wave travel times is about 6s (Grand and Donald V. Helmberger 1984; Lay and Helmberger 1983a) and about half of this for P-waves. These features occur roughly along the Rocky Mountain Front. While PcP results displayed in Fig. 3.20 are in general agreement with these earlier studies, the PKiKP amplitude near the new Mexico-Texas boundary for event 20091126 are anomalously low. We think this is caused by the ICB as discussed later.

One of the remarkable fine-scale features of this mapping is the behavior of amplitudes between PcP and PKiKP along the northwestern coast, especially for event 20091126. Note the reversed strength between PcP and PKiKP, i.e., when PcP is weak, PKiKP is strong. We also found extreme differences in PKiKP amplitudes

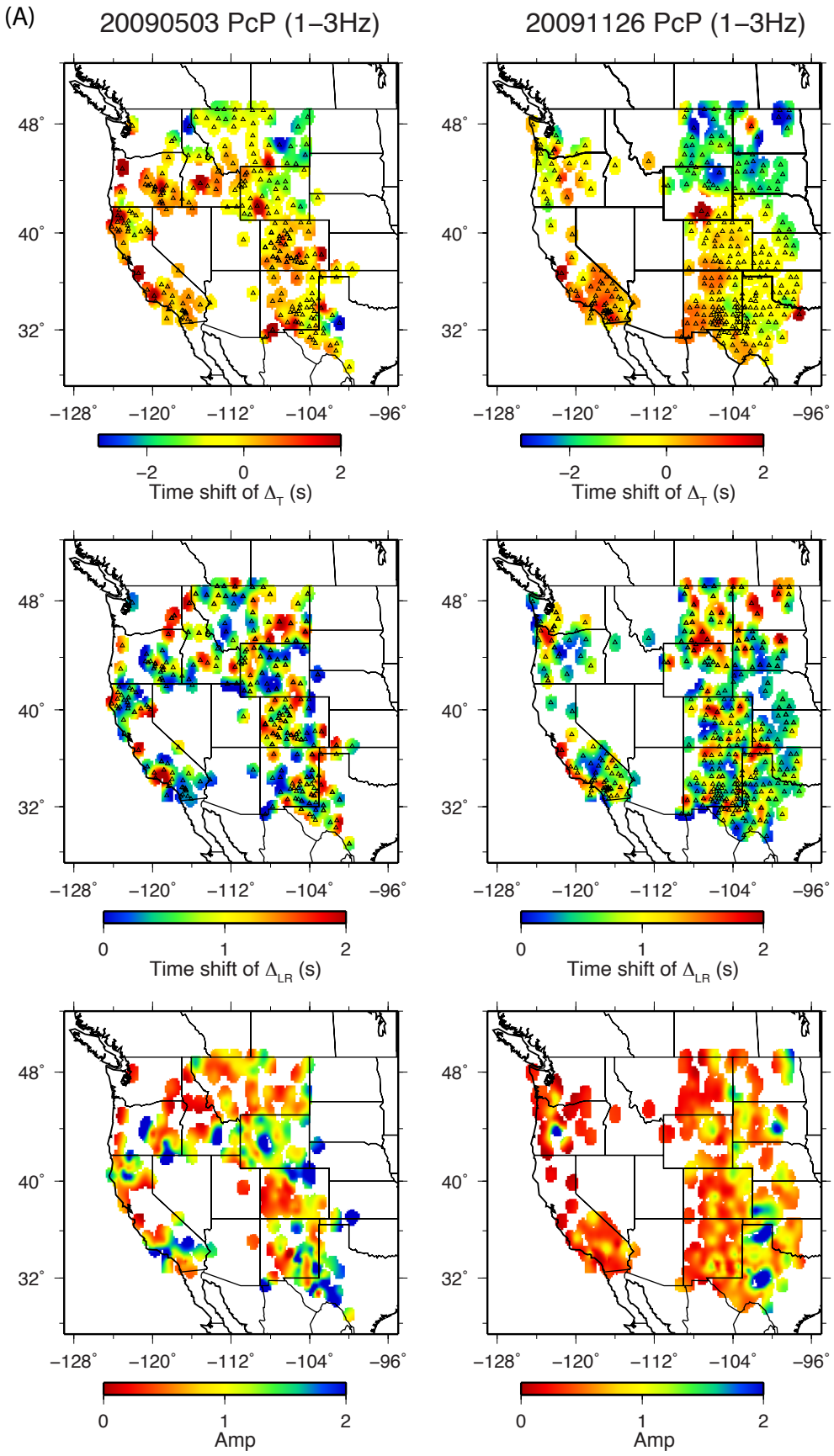
(A)
20090503 PcP (1–3Hz)
20091126 PcP (1–3Hz)
48°
40°
32°
−128°
−120°
−112°
−104°
−96°
−2
0
2
Time shift of Δ_T (s)
0
1
2
Time shift of Δ_LR (s)
Amp

(a) PcP phase

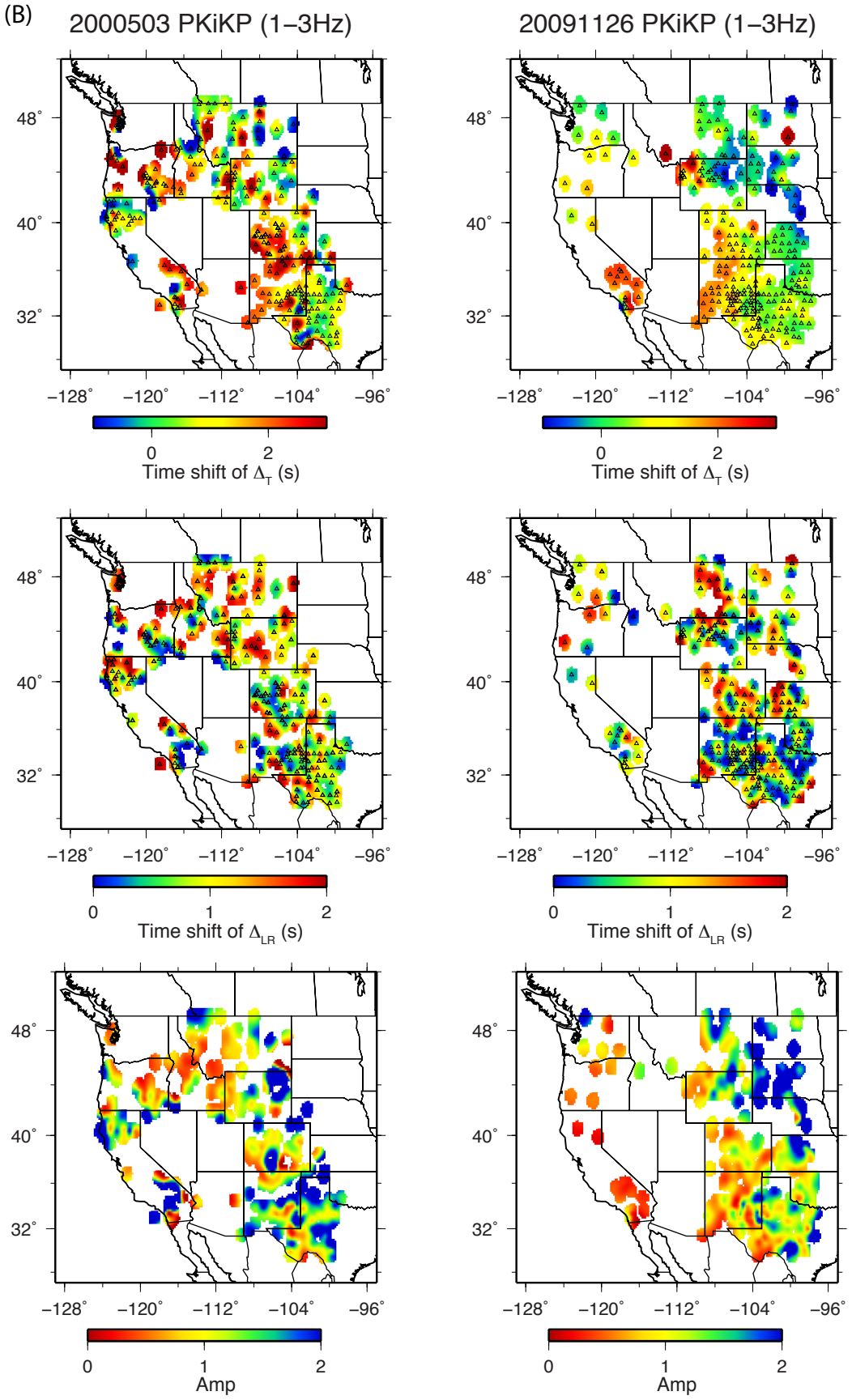

(b) PKiKP phase

Figure 3.20: MPD patterns of (a) PcP and (b) PKiKP phases for events 20090503 and 20091126, displaying considerable scatter.

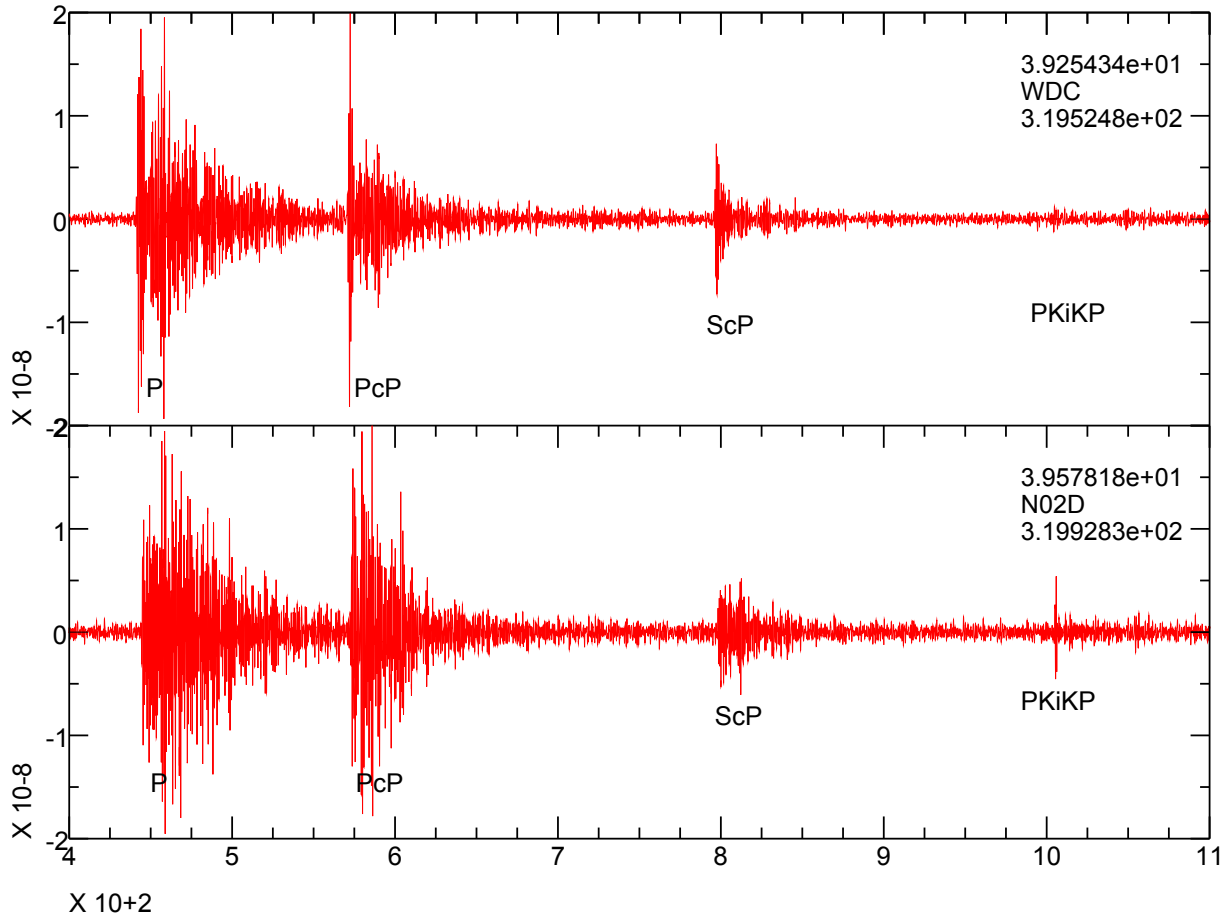

Figure 3.21: Seismograms (1 to 3Hz) of 20091126 event for two northern California stations 45km apart, where the core phases ray may sample the subducted slab. Note that P, PcP, and ScP phases are about the same amplitude, while PKiKP amplitudes are quite different.

at neighboring stations, less than 50 km apart, where one is in the noise while the other is very strong (see Fig. 3.21). These observations appear to be related to the subduction zone as in the Tkalčić et al. (2010) study. However, most of stations in our datasets do not display such anti-correlations. The variation appears to be caused by upper mantle scattering that is known to some degree, i.e., Nielsen et al. (2003).

Appendix B: Waveform Simulation

Significant progress in 3D modeling of global seismograms at the longer periods (17-100s) becomes possible with the development of advanced computing systems, Komatitsch and Tromp (2002). Extending this to shorter periods is challenging because of computing demands, so hybrid techniques prove useful. Several axisym-

metric methods can reach shorter periods such as in Nissen-Meyer et al. (2007). The 2D pseudo-spectral approach as described in Cormier (2000) is particularly good at treating random media and used extensively in the recent study by Tkalčić et al. (2009). Some hybrid methods use a combination of analytic and finite-difference (FD) methods which are interfaced with the Kirchhoff integral. Essentially, one propagates a signal through simple regions using generalized rays and only uses numerical methods in the heterogeneous regions, see Wen and Helmberger (1998). This method was used by Dai et al. (2012) in inserting a box-like structure at the ICB. We have reproduced their results using our new 2D FD code(Li et al. 2014), as discussed in the main text.

To obtain seismograms from a point source in 2D media, we need to consider in-plane propagation and out-of-plane spreading. Three difficulties needs to be addressed in implementing this procedure: (1) the mapping procedure involved in 3D source excitation for earthquakes; (2) 3D spreading corrections; and (3) reducing the spherical earth to a flattened model. We solved the first issue by using a modern moment tensor excitation approach. The out-of-plane geometric spreading is accounted for by applying a post-simulation filter. In addition, an earth-flattening transformation is used to obtain simulations in a spherical geometry using calculations based on Cartesian coordinates. Simulations are generated using the 2D staggered grid finite difference method on graphics processing units (GPUs), which proves to be highly efficient and flexible for modeling global seismograms, including core phases. The effectiveness of this method is demonstrated by comparing our synthetics with the frequency-wavenumber normal-mode and SEM synthetics(Li et al. 2014).

The 2D pseudo-spectral method has been used extensively for studying scattering effects near the CMB, i.e., Cormier (2000). Recently it was used to investigate receiver effects for plane-wave incidence of PcP and PKiKP (Tkalčić et al. 2010). We repeated this experiment but assumed a point source for the PREM model, Fig. 3.22. We place the "scattering boxes" either beneath the source or the receivers. We assume an explosion source and Gaussian random media. To test our code, we conducted a detailed reciprocity numerical experiment given in Fig. 3.23. In Fig. 3.22, we can see that ray paths for PKiKP leaving the source region are nearly the same for receivers from 20° to 30°. The PcP rays are also compact but have an offset relative to PKiKP. In contrast, the ray paths are well separated at the receiver side with each path encountering a distinct structure. The synthetics for

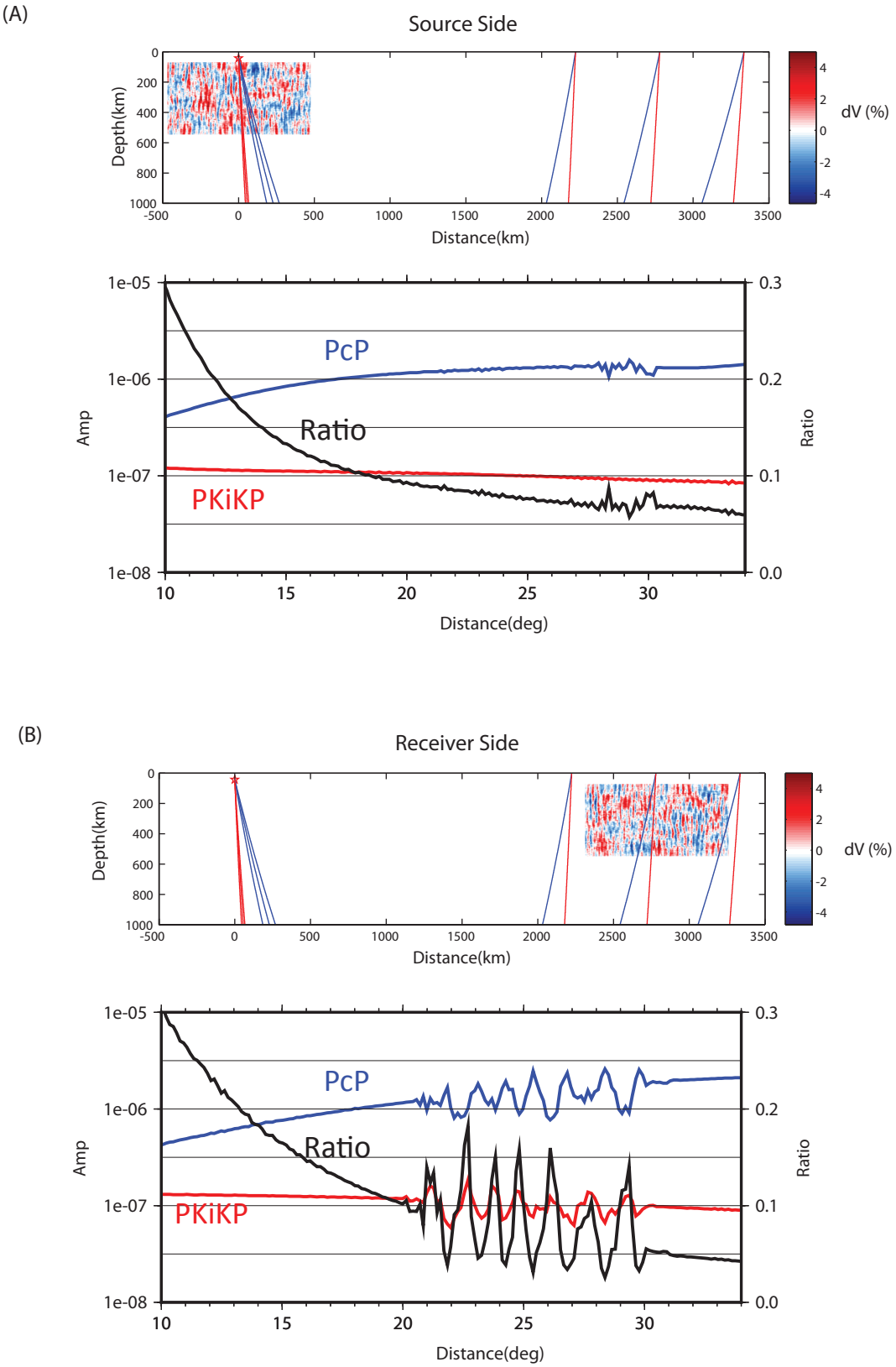

Figure 3.22: Sensitivity testing where random scatter media are placed beneath the source side (A) and receiver side (B). The amplitude of PcP (red), PKiKP(blue) and their ratio (black) are also displayed. Note the scatters in the source side have small effects on the relative amplitude at the receivers, where the scatters at the receiver side have large effects.

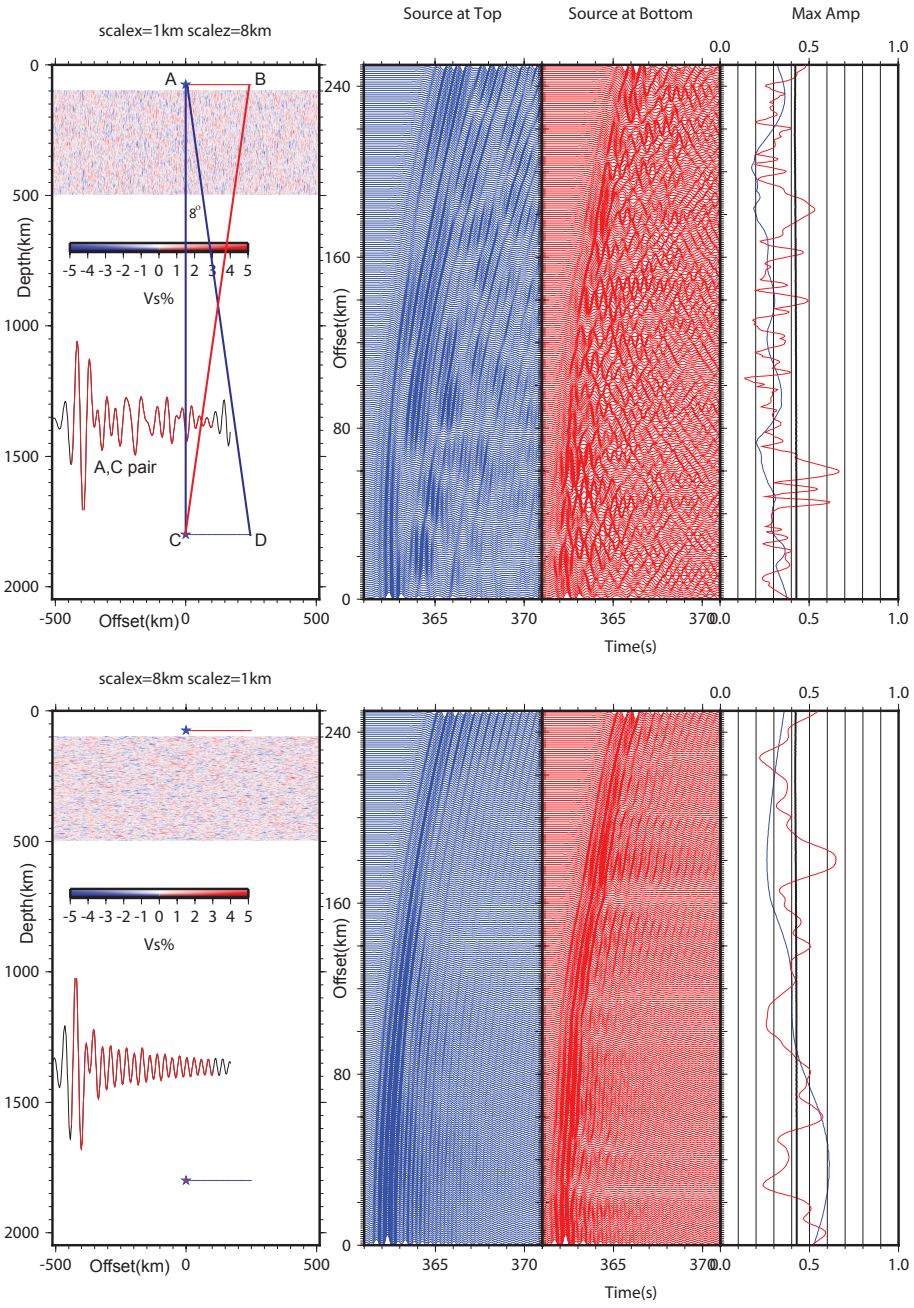

Figure 3.23: For SH wave and point force source, we calculate synthetics for homogeneous model (Vs 4.8 km/s) with top part having random variation. Two random media models with different scale length ratio are shown here. For each simulation, central frequency is 1.5 Hz, grid space is 0.5 km, which ensures 6 grid per wavelength. We put (1) Source at A, and receiver along CD line, (2) source at C, receiver along AB. The models are displayed on the left with synthetic sections and amplitudes on the right, color coded the same as source. The A,C pair seismogram satisfies reciprocity quite well, as shown in the inset. The record sections, AB, CD differs because of the different path in sampling the media. Variation in AB line is larger and more rapid than variation along CD line. Thus heterogeneity at the source side has small effects on records, while heterogeneity at the receiver side has large effects.

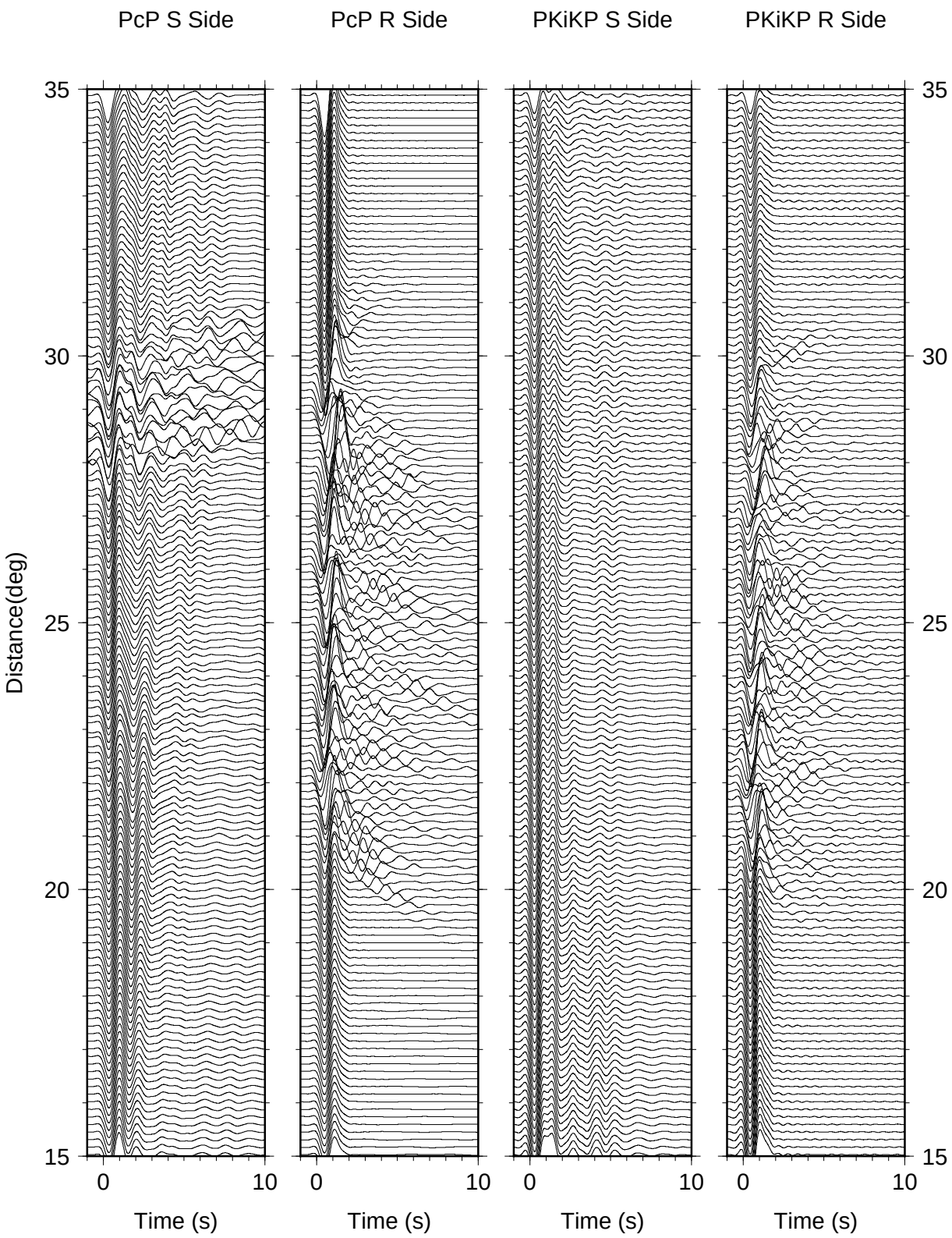

Figure 3.24: Synthetic seismograms for core phases for heterogeneity at source side and receiver side. The interruption of PcP in the leftmost panel is due to surface wave. In general, note that heterogeneity at sthe ource side has small effects on records, while heterogeneity at the receiver side has large effects.

these two situations are given in Fig. 3.24 and the amplitude variation is included in Fig. 3.22. Note that the rapid amplitude decay of PKiKP and the gentle increase in PcP controlled by the PREM model which is similar to the AK135 results as shown in Tkalčić et al. (2009). The PKiKP/PcP ratio is also displayed where the effect from source side scattering (Fig. 3.22) is smaller than that from receiver side scattering.

References

Adushkin, V. V. and V. M. Ovchinnikov (2004). "The Mosaic in Reflections from the Earth's Solid Core Boundary". In: *Doklady earth sciences* 397.6, pp. 883–885 (cit. on p. 49).

Cao, Aimin, Yder Masson, and Barbara Romanowicz (2007). "Short wavelength topography on the inner-core boundary." In: *Proceedings of the National Academy of Sciences of the United States of America* 104.1, pp. 31–35. ISSN: 0027-8424. DOI: 10.1073/pnas.0609810104 (cit. on pp. 48, 72).

Cormier, Vernon F (2000). "D" as a transition in the heterogeneity spectrum of the lowermost mantle". In: *Journal of Geophysical Research* 105.B7, pp. 16193–16205 (cit. on p. 79).

Cormier, Vernon F. and George L. Choy (1986). "A search for lateral heterogeneity in the inner core from differential travel times near PKP-D and PKP-C". In: *Geophysical Research Letters* 13.13, pp. 1553–1556 (cit. on p. 47).

Cormier, V.F. and P.G. Richards (1977). "Full wave theory applied to a discontinuous velocity increase: the inner core boundary". In: *J. Geophys.* 43, pp. 3–31 (cit. on p. 48).

Cummins, Phil and Lane R. Johnson (1988). "Short-period body wave constraints on properties of the Earth's inner core boundary". In: *Journal of Geophysical Research* 93.B8, p. 9058. ISSN: 0148-0227. DOI: 10.1029/JB093iB08p09058 (cit. on pp. 48, 51).

Dai, Zhiyang, Wei Wang, and Lianxing Wen (2012). "Irregular topography at the Earth's inner core boundary". In: *Proceedings of the National Academy of Sciences of the United States of America* 109.20, pp. 7654–7658. DOI: 10.1073/pnas.1116342109/-/DCSupplemental.www.pnas.org/cgi/doi/10.1073/pnas.1116342109 (cit. on pp. 48, 64, 69, 72, 79).

Engdahl, E. R., Edward A. Flinn, and Carl F. Romney (1970). "Seismic waves reflected from the Earth's inner core". In: *Nature* 228, pp. 852–853 (cit. on p. 48).

Grand, Stephen P. and Donald V. Helmberger (1984). "Upper mantle shear structure of North America". In: *Geophysical Journal of the Royal Astronomical Society* 76, pp. 399–438 (cit. on p. 75).

Helmberger, D. V. and S. Ni (2005). "Approximate 3D Body-Wave Synthetics for Tomographic Models". In: *Bulletin of the Seismological Society of America* 95.1, pp. 212–224. ISSN: 0037-1106. DOI: 10.1785/0120040004 (cit. on p. 50).

Kawakatsu, Hitoshi (2006). "Sharp and seismically transparent inner core boundary region revealed by an entire network observation of near-vertical PKiKP". In: *Earth Planets Space* 58, pp. 855–863 (cit. on p. 48).

Komatitsch, Dimitri and Jeroen Tromp (2002). "Spectral-element simulations of global seismic wave propagation - II . Three-dimensional models , oceans , rotation and self-gravitation". In: *Geophysical Journal International* 150, pp. 303–318 (cit. on p. 78).

Koper, Keith D. (2004). "Observations of PKiKP / PcP amplitude ratios and implications for Earth structure at the boundaries of the liquid core". In: *Journal of Geophysical Research* 109.B3, B03301. ISSN: 0148-0227. DOI: 10.1029/2003JB002750 (cit. on p. 48).

Koper, Keith D. and Marina Dombrovskaya (2005). "Seismic properties of the inner core boundary from PKiKP/P amplitude ratios". In: *Earth and Planetary Science Letters* 237.3-4, pp. 680–694. ISSN: 0012821X. DOI: 10.1016/j.epsl.2005.07.013 (cit. on p. 48).

Lay, Thorne and Donald V Helmberger (1983a). "A shear velocity discontinuity in the lower mantle". In: *Geophysical Research Letters* 10.1, pp. 63–66 (cit. on p. 75).

Lay, Thorne and Donald V. Helmberger (1983b). "Body-wave amplitude and travel-time correlations across north america". In: *Bulletin of the Seismological Society of America* 73.4, pp. 1063–1076 (cit. on p. 75).

Li, Dunzhu et al. (2014). "Global synthetic seismograms using a 2-D finite-difference method". In: *Geophysical Journal International*. DOI: 10.1093/gji/ggu050 (cit. on pp. 49, 79).

Nielsen, Lars et al. (2003). "Origin of upper-mantle seismic scattering - evidence from Russian peaceful nuclear explosion data". In: *Geophysical Journal International* 154.1, pp. 196–204. ISSN: 0956540X. DOI: 10.1046/j.1365-246X.2003.01955.x (cit. on p. 78).

Nissen-Meyer, Tarje, Alexandre Fournier, and F. a. Dahlen (2007). "A two-dimensional spectral-element method for computing spherical-earth seismograms - I. Moment-tensor source". In: *Geophysical Journal International* 168.3, pp. 1067–1092. ISSN: 0956540X. DOI: 10.1111/j.1365-246X.2006.03121.x (cit. on p. 79).

Niu, F and L Wen (2001). "Hemispherical variations in seismic velocity at the top of the Earth's inner core." In: *Nature* 410, pp. 1081–1084. ISSN: 0028-0836. DOI: 10.1038/35074073 (cit. on pp. 48, 72).

Poupinet, G., R. Pillet, and A. Souriau (1983). “Possible heterogeneity of the Earth’s core deduced from PKIKP travel times”. In: *Nature* 305, pp. 204–206 (cit. on p. 47).

Shearer, P. and G. Masters (1990). “The density and shear velocity contrast at the inner core boundary”. In: *Geophysical Journal International* 102.2, pp. 491–498. ISSN: 0956540X. DOI: 10.1111/j.1365-246X.1990.tb04481.x (cit. on p. 48).

Shimizu, H., J.P. Poirier, and J.L. Le Mouël (2005). “On crystallization at the inner core boundary”. In: *Physics of the Earth and Planetary Interiors* 151.1-2, pp. 37–51. ISSN: 00319201. DOI: 10.1016/j.pepi.2005.01.001 (cit. on p. 47).

Song, Xiaodong and Don V. Helmberger (1992). “Velocity structure near the inner core boundary from waveform modeling”. In: *Journal of Geophysical Research* 97.B5, pp. 6573–6586 (cit. on p. 48).

Song, Xiaodong and Paul G. Richards (1996). “Seismological evidence for differential rotation of the Earth’s inner core”. In: *Nature* 382, pp. 221–224 (cit. on p. 72).

Sun, Daoyuan and Don Helmberger (2011). “Upper-mantle structures beneath USArray derived from waveform complexity”. In: *Geophysical Journal International* 184.1, pp. 416–438. ISSN: 0956540X. DOI: 10.1111/j.1365-246X.2010.04847.x (cit. on pp. 50, 69, 75).

Sun, Daoyuan et al. (2013). “Rolling hills on the core-mantle boundary”. In: *Earth and Planetary Science Letters* 361, pp. 333–342. ISSN: 0012821X. DOI: 10.1016/j.epsl.2012.10.027 (cit. on pp. 51, 64).

Tkalčić, Hrvoje, Brian L. N. Kennett, and Vernon F. Cormier (2009). “On the inner-outer core density contrast from PKiKP/PcP amplitude ratios and uncertainties caused by seismic noise”. In: *Geophysical Journal International* 179.1, pp. 425–443. ISSN: 0956540X. DOI: 10.1111/j.1365-246X.2009.04294.x (cit. on pp. 69, 79, 83).

Tkalčić, Hrvoje et al. (2010). “Steep reflections from the earth’s core reveal small-scale heterogeneity in the upper mantle”. In: *Physics of the Earth and Planetary Interiors* 178.1-2, pp. 80–91. ISSN: 00319201. DOI: 10.1016/j.pepi.2009.08.004 (cit. on pp. 48, 51, 58, 78, 79).

Waszek, Lauren, Jessica Irving, and Arwen Deuss (2011). “Reconciling the hemispherical structure of Earth’s inner core with its super-rotation”. In: *Nature Geoscience* 4.4, pp. 264–267. ISSN: 1752-0894. DOI: 10.1038/ngeo1083 (cit. on p. 48).

Wen, Lianxing (2006). “Localized temporal change of the Earth’s inner core boundary.” In: *Science* 314, pp. 967–970. ISSN: 1095-9203. DOI: 10.1126/science.1131692 (cit. on p. 48).

Wen, Lianxing and Donald V Helmberger (1998). “A two-dimensional P-SV hybrid method and its application to modeling localized structures near the core-mantle boundary”. In: *Journal of Geophysical Research* 103.B8, pp. 17901–17918 (cit. on p. 79).

Wen, Lianxing and Fenglin Niu (2002). “Seismic velocity and attenuation structures in the top of the Earth’s inner core”. In: *Journal of Geophysical Research* 107.B11, p. 2273. ISSN: 0148-0227. DOI: 10.1029/2001JB000170 (cit. on pp. 48, 72).

Chapter 4

TOWARDS THE FULL ADJOINT FOR THE INVERSION OF MANTLE CONVECTION

We develop and test an adjoint based inversion for the simultaneous recovery of initial temperature conditions and viscosity parameters for a mantle convection problem. Based on a realistic rheological model including temperature and strain-rate dependent viscosity, we formulate the inversion problem within a PDE constrained optimization framework. We optimize a cost function that includes the misfit of surface velocity (plate motion) history and misfit of the current mantle temperature. The true discrete gradient of the cost function is obtained by solving the adjoint equation, itself derived in a fully discrete fashion, considering all dependencies between variables. The fully discrete approach allows us to check the correctness of our implementation through a finite difference test. The optimization is accelerated through a modified LBFGS method by adding a preconditioner. We test the method through two synthetic cases, a sinking cylinder and a realistic subduction model. The subduction model is characterized by the migration of a ridge toward a trench whereby both plate motions and subduction evolve. The results demonstrate: (1) given known viscosity parameters, the initial temperature can be well recovered, as in previous initial condition-only inversions where effective viscosity itself is given; (2) given the true initial temperature, viscosity parameters can be recovered accurately, even under a relatively strong trade off between viscosity parameters, at least for the parameters considered; (3) for the joint inversion of initial condition and viscosity parameters, initial condition and effective viscosity can be reasonably recovered, but small inaccuracies in the recovered temperature field may limit convergence to the correct viscosity parameters.

4.1 Introduction

Mantle convection and plate motions are coupled phenomena (e.g., Davies 1999) in which the constitutive relation (viscosity law) plays a first order role in determining not only the extent of this coupling but also the structure and evolution of mantle convection. Despite substantial effort attempting to determine the viscosity structure of the mantle, either through forward and inverse geophysical models or through laboratory work, many first order questions remain. For example, although

global geophysical flow models have suggested that the strength of lateral viscosity variations might be small (about an order of magnitude) (e.g., Moucha et al. 2007; Yang and Gurnis 2016), global forward (Stadler et al. 2010) and local inverse models (Baumann and Kaus 2015) suggest that the lateral variations in viscosity associated with plate tectonics may be many orders of magnitude ($> 10^3$). In addition, as long evident through forward models (Mckenzie et al. 1974; Lenardic et al. 2003) or plate tectonic reconstructions (see review by Seton et al. (2012)), mantle convection is highly time-dependent. This time-dependence implies that it is essential to find ways to constrain the structure of mantle convection sequentially backwards in time. Some progress along these lines has been made with global forward models (e.g., Bunge et al. 2009; Bower et al. 2015) and inverse models (e.g., Spasojevic et al. 2009; Moucha and Forte 2011). Although there has been some attempt to use variable viscosity in such inverse models meant to recover mantle structure in the past (Liu et al. 2008), they have not, arguably, approached realistic variations in viscosity that are critical to the dynamics.

Computational models of mantle convection, often with realistic rheologies, are now commonly being used to interpret a wide range of phenomena, such as plate motions, rifting, subduction, basin formation, continental delamination, and sea level change, for example. Forward models in particular have become detailed and realistic. For example, a wide range of studies have focused on the time dependence of subduction showing the evolution of slabs (Billen and Hirth 2007; Burkett and Billen 2009; Gerya 2011; Garel et al. 2014). Such models show potentially diagnostic time-dependent phenomena, including how slab structure, including slab dip and the degree of slab folding, change with time. Many of the same classes of phenomena are now found in different studies while qualitatively fitting general plate motions and seismic images of subducted slabs. Given the success with forward models and the general consensus of the classes of phenomena seen in forward models (see reviews in Billen 2008; Gerya 2011), we demonstrate here that these problems can be cast in an inverse sense.

Inverse models for convection have been formulated previously. For example, Bunge et al. (2003) advanced an adjoint method to recover an initial condition from the inversion, using seismic "images" as the data to fit in a model with plate motion history. Horbach et al. (2014) further derived this initial condition inversion using a general operator formulation, and found that a strong global minimum exists for the unknown initial condition, regardless of the starting model. In these two studies,

the viscosity structure is given, and does not depend on other state variables such as temperature and strain rate. Liu and Gurnis (2008) proposed an inversion of both viscosity parameters and initial conditions using an embedded pair of loops, where an inner loop with an adjoint of the energy equation, as in Bunge et al. (2003), recovers the initial condition assuming known viscosity parameters, while an outer loop recovers the viscosity parameters using linear least square in the context of fitting the dynamic topography. The method has been applied to the recovery of subduction history in North America since the Late Cretaceous (Spasojevic et al. 2009). Although the viscosity in their model is temperature- and strain-rate-dependent, they do not incorporate such dependence into the derivation of the adjoint equation, resulting in a suboptimal gradient. Our study is similar to these previous studies in terms of the inversion setup, but with several key extensions. We will build on the work of Bunge et al. (2003), Spasojevic et al. (2009), and Horbach et al. (2014), and argue that besides initial conditions, a key component of a formal inversion should be the inference of material properties, involving the scaling between seismic velocity anomalies and density and temperature, the parameters that determine the temperature-dependence of viscosity, yield stress, and the non-linear exponent for strain-rate dependent viscosity, and so on. The constitutive properties are important because they determine the time-dependent dynamics of subduction and mantle convection (Zhong and Gurnis 1995b; Garel et al. 2014). This joint inversion is similar to Liu and Gurnis (2008), but we will derive a full adjoint set of equations considering all the dependencies.

The inference of the parameters of variable viscosity is mathematically and algorithmically involved. Worthen et al. (2014) studied inversion of these parameters in an adjoint of instantaneous Stokes flow by fitting surface velocity observations, where the temperature structure is assumed given. They invert spatially varying parameter fields, like prefactor and nonlinear exponent to the viscosity law, using a limited memory BFGS (Broyden-Fletcher-Goldfarb-Shanno) quasi-Newton method, and find a strong trade off between the prefactor and nonlinear exponent fields, although the effective viscosity and viscous dissipation are well recoverable. Following this approach, Ratnaswamy et al. (2015) also use an adjoint of the Stokes equation but caste the problem within a Bayesian framework to infer several important viscosity parameters controlling plate coupling, including a yield stress, a non-linear exponent in the stress-strain rate relation, and the prefactor on the viscosity within several individual fault zones. Their unknowns are scalar parameters instead of parameter fields, which allowed them to form the second derivatives (the

Hessian matrix) explicitly and demonstrated the trade off between parameters with a posterior covariance matrix.

Based on these previous studies, we attempt to solve an inversion problem where the unknowns include both the initial temperature condition and scalar viscosity parameters of the mantle. The data we use are the present day mantle temperature (which would be inferred from seismic tomography) and plate reconstruction history. Following a general PDE-constrained optimization framework, we define the cost function, obtain its gradient using the adjoint method, and finally solve the optimization using a gradient-based method. We illustrate our method using two synthetic examples, one being a model of a sinking cylinder (a circle in two dimensions), and another of subduction and plate motions with a realistic viscosity law.

4.2 Equations for mantle convection

We study mantle convection and plate motion as governed by a creeping viscous fluid in a Cartesian domain Ω (assumed to be 2-D). Under the Boussinesq approximation for an incompressible fluid, the non-dimensional equations governing mantle convection are the equations for conservation of mass and momentum, i.e., the Stokes equations

$$\nabla \cdot \boldsymbol{u} = 0, \tag{4.1a}$$

$$-\nabla \cdot \sigma = \mathrm{Ra} T \boldsymbol{e}_z, \tag{4.1b}$$

and the equation for conservation of energy

$$\frac{\partial T}{\partial t} + \boldsymbol{u} \cdot \nabla T - \nabla^2 T = 0, \tag{4.2}$$

where $\mathbf{u}$ is the velocity, T the temperature, Ra the Rayleigh number, and $\boldsymbol{e}_z$ the unit vector pointing in the direction of gravity. The stress tensor, σ, is defined by

$$\sigma = -pI + 2\eta_{\mathrm{eff}} D(\boldsymbol{u}),$$
$$D(\boldsymbol{u}) = \frac{1}{2}\left(\nabla \boldsymbol{u} + (\nabla \boldsymbol{u})^{\intercal}\right),$$

with p the pressure, and η_{eff} the effective viscosity, which depends on location, temperature and strain rate (details defined in later).

We assume the Dirichlet condition for temperature on the top and bottom of the domain Γ_d, and no flux condition on the remaining (side) boundaries

$$\begin{aligned} T|_{\Gamma_d} &= T_d, \\ \nabla T \cdot \boldsymbol{n}|_{\partial\Omega\setminus\Gamma_d} &= 0, \end{aligned}$$

where $\boldsymbol{n}$ is the unit normal at the boundary, and T_d specifies the Dirichlet boundary condition ($T_d = 0$ at the top and $T_d = 1$ at the bottom for the subduction model).

For the Stokes equation, we assume a free slip mechanical condition on all boundaries

$$\begin{aligned} \boldsymbol{u} \cdot \boldsymbol{n}|_{\partial\Omega} &= 0, \\ \boldsymbol{n} \times (\boldsymbol{n} \times \sigma\boldsymbol{n})\,|_{\partial\Omega} &= 0. \end{aligned}$$

The initial condition for the temperature is specified as T^0, i.e.,

$$T(x, t = 0) = T^0(x).$$

4.3 Viscosity law

The viscosity of the mantle is governed by the high-temperature creep of silicates in which laboratory experiments show that the creep strength is temperature-, pressure-, compositional- and stress-dependent (Ranalli and Karato 1995). The effective viscosity η_{eff} is thus specified by the following viscosity law

$$\begin{aligned} \varepsilon_{\text{II}} &= \frac{1}{2} D(\boldsymbol{u}) : D(\boldsymbol{u}), \\ \eta &= C e^{E(0.5-T)} \left(\varepsilon_{II}\right)^{\frac{1-n}{2n}}, \\ \eta_{\text{eff}} &= \eta_{\min} + \min\left(\frac{\sigma_{\text{yield}}}{2\sqrt{\varepsilon_{II}}}, W \min\left(\eta_{\max}, \eta\right)\right), \end{aligned} \tag{4.3}$$

where ϵ_{II} is the second invariant of strain rate tensor, $C > 0$ is a viscosity prefactor, $E > 0$ is the non dimensional activation energy, $n > 0$ is the nonlinear exponent, $\{\eta_{\min}, \eta_{\max}\}$ controls the range of viscosity, and σ_{yield} is the yield stress, and we refer to $W(x)$, $0 < W(x) \leq 1$, as the weakening factor.

In our model, W is used to approximate phenomenological aspects that cannot be represented in a purely viscous flow model, such as processes which govern mega-thrust faults along the subduction interface, or partial melting near a mid-ocean ridge. For example, mega-thrust faults are represented using a weakzone stencil (that is, a stencil outlining the region around a megathrust thought to have weakened

over geological time), where $W(x) = 1$ throughout most of the domain, except along the subduction interface and near ridges where $W(x) < 1$. One can allow the stencil to move with time $W = W(x,t)$ to model trench rollback or advance, but we currently have not incorporated such a time-dependent stencil in our inversion model.

4.4 Discretization

The finite element method (FEM) is widely used for computations of mantle convection simulation (e.g., Moresi et al. 2000). The method can incorporate many aspects that are inherently important to mantle convection, such as complicated geometry, different boundary conditions, variable material properties, and mesh refinement. We build our FEM code using the deal.II finite element library (Bangerth et al. 2007), upon which ASPECT (Kronbichler et al. 2012), a community code for mantle convection, is also based. One feature of deal.II is the extensive support for adaptive mesh refinement (AMR), including the p4est library (Burstedde et al. 2011). AMR does not require us to specify the mesh a priori, and instead the mesh can be refined or coarsened according to user-defined error indicators, such as the Kelly error indicator (Kronbichler et al. 2012) or norms of either temperature gradients or strain rate (or different combinations) (Burstedde et al. 2013). Such versatility allows us to explore different weak zone formulations that are important in models of subduction evolution.

The finite element method is based on the weak form of the equations, and results in finite-dimensional nonlinear equations. Here we describe in matrix form the equations, while highlighting the dependence of variables. We use Taylor–Hood elements, i.e., quadratic elements for temperature and velocity, and linear element for pressure. At time t^n, using the discrete temperature vector T^n, we compute the discrete velocity vector U^n and pressure vector P^n by solving the nonlinear Stokes equation

$$\begin{bmatrix} A(U^n, T^n, m) & B \\ B^\intercal & 0 \end{bmatrix} \begin{bmatrix} U^n \\ P^n \end{bmatrix} = \begin{bmatrix} FT^n \\ 0 \end{bmatrix}, \tag{4.4}$$

where m are the rheological parameters, and

$$
\begin{aligned}
A_{ij} &= \int 2\eta_{\text{eff}}(U^n, T^n, m) D(\phi_i^u) : D(\phi_j^u) d\Omega, \\
B_{ij} &= \int -(\nabla \cdot \phi_i^u)\phi_j^p d\Omega, \\
F_{ij} &= \int R_a \phi_i^u \cdot \left(\phi_j^T e_z\right) d\Omega,
\end{aligned}
$$

with $\phi_i^u, \phi_i^p, \phi_i^T$ being the shape functions for velocity, pressure, and temperature, respectively.

For time-stepping the energy equation, a second-order scheme is often preferred. Kronbichler et al. (2012) use a second-order accurate implicit/explicit scheme within the ASPECT code, which requires two previous timesteps' states to calculate a new timestep. For our inversion problem, we prefer a second order implicit Runge-Kutta method, because it requires only the state at one previous timestep, and the whole computation can start from one initial temperature. This implicit scheme is unconditionally stable, so we can use the same set of timesteps in the whole inversion, no matter how large the convecting velocity from current guess of temperature can be.

Following the Galerkin finite element method (Hughes 1987), the weak form for the energy equation is

$$
\int \left[\phi \left(\frac{\partial T}{\partial t} + \boldsymbol{u} \cdot \nabla T \right) + \nabla \phi \nabla T \right] d\Omega = 0,
$$

where ϕ is the test function for temperature. But as noted in previous studies, the Galerkin formulation is anti-diffusive, resulting in artifacts. Several methods exist to control these artifacts, for example, a streamline upwind Petrov-Galerkin formulation (SUPG) (Brooks and Hughes 1982), or an artificial diffusivity method as used in ASPECT (Kronbichler et al. 2012). We use SUPG here. Following SUPG method, we will change the temperature test function from ϕ to $\phi + \tau \boldsymbol{u} \cdot \nabla \phi$, with τ being the SUPG parameter defined as

$$
\tau = \begin{cases} -1 - 1/\text{Pe}, & \text{Pe} < -1, \\ 0, & -1 \leq \text{Pe} \leq 1, \\ 1 - 1/\text{Pe}, & \text{Pe} > 1, \end{cases} \tag{4.5}
$$

with $\mathrm{Pe} = uh_e/2\kappa$, the local Peclet number within the element with h_e representative of the element size, and κ the thermal diffusivity. Then we have

$$\int \left[(\phi + \tau \boldsymbol{u} \cdot \nabla \phi) \left(\frac{\partial T}{\partial t} + \boldsymbol{u} \cdot \nabla T \right) + \nabla \phi \nabla T \right] d\Omega = 0,$$

which expands to

$$\int \left[\phi \frac{\partial T}{\partial t} + (\tau \boldsymbol{u} \cdot \nabla \phi) \frac{\partial T}{\partial t} + \phi \boldsymbol{u} \cdot \nabla T + (\tau \boldsymbol{u} \cdot \nabla \phi) (\boldsymbol{u} \cdot \nabla T) + \nabla \phi \nabla T \right] d\Omega = 0.$$

After a FEM discretization in space of the above equation, we have in matrix form an ODE

$$M \frac{dT}{dt} + M^S(\boldsymbol{u}) \frac{dT}{dt} + C(\boldsymbol{u})T + C^S(\boldsymbol{u})T + KT = 0,$$

where

$$\begin{aligned}
M_{ij} &= \int \phi_i^T \phi_j^T d\Omega, \\
M_{ij}^S &= \int \tau \left(\boldsymbol{u} \cdot \nabla \phi_i^T \right) \phi_j^T d\Omega, \\
C_{ij} &= \int \phi_i^T \boldsymbol{u} \cdot \nabla \phi_j^T d\Omega, \\
C_{ij}^S &= \int \left(\tau \boldsymbol{u} \cdot \nabla \phi_i^T \right) \left(\boldsymbol{u} \cdot \nabla \phi_j^T \right) d\Omega, \\
K_{ij} &= \int \nabla \phi_i \cdot \nabla \phi_j d\Omega.
\end{aligned}$$

We use a Runge-Kutta scheme modified from Bonito et al. (2014) to solve this ODE. To march forward from t^n to t^{n+1}, we introduce an intermediate timestep $t^{h,n} = t_n + \frac{t^{n+1} - t^n}{2}$, and obtain the corresponding temperature $T^{h,n}$ from

$$M \frac{T^{h,n} - T^n}{t^{h,n} - t^n} + C(U^n)T^n + KT^{h,n} = 0, \tag{4.6}$$

where U^n is obtained through the solution of Eq. 4.4. Note that in this half time step marching, we do not use SUPG, and the convection term $C(U^n)T^n$ is explicit, while the diffusion term $KT^{h,n}$ is implicit. Then, we solve Stokes equation to obtain $U^{h,n}$, $P^{h,n}$ from $T^{h,n}$ by

$$\begin{bmatrix} A(U^{h,n}, T^{h,n}, m) & B \\ B^\intercal & 0 \end{bmatrix} \begin{bmatrix} U^{h,n} \\ P^{h,n} \end{bmatrix} = \begin{bmatrix} FT^{h,n} \\ 0 \end{bmatrix}. \tag{4.7}$$

Finally a full time step update is performed with the SUPG term, and implicit convection and diffusion term

$$M\frac{T^{n+1}-T^n}{t^{n+1}-t^n}+M^S(U^{h,n})\frac{T^{n+1}-T^n}{t^{n+1}-t^n}+C(U^{h,n})T^{n+1}+C^S(U^{h,n})T^{n+1}+KT^{n+1}=0. \tag{4.8}$$

The forward modeling Eqs.4.4 to 4.8 can be rewritten as

$$\begin{bmatrix} A(U^n,T^n,m) & B \\ B^\intercal & 0 \end{bmatrix}\begin{bmatrix} U^n \\ P^n \end{bmatrix}=\begin{bmatrix} FT^n \\ 0 \end{bmatrix}, \tag{4.9a}$$

$$M_a^nT^{h,n}=M_b^nT^n, \tag{4.9b}$$

$$\begin{bmatrix} A(U^{h,n},T^{h,n},m) & B \\ B^\intercal & 0 \end{bmatrix}\begin{bmatrix} U^{h,n} \\ P^{h,n} \end{bmatrix}=\begin{bmatrix} FT^{h,n} \\ 0 \end{bmatrix}, \tag{4.9c}$$

$$M_c^nT^{n+1}=M_d^nT^n, \tag{4.9d}$$

where

$$\begin{aligned} M_a^n &= \left(M+\frac{1}{2}\Delta t^nK\right),\\ M_b^n(U^n) &= \left(M-\frac{1}{2}\Delta t^nC(U^n)\right),\\ M_c^n(U^{h,n}) &= M+M^S(U^{h,n})+\Delta t^n\left[K+C(U^{h,n})+C^S(U^{h,n})\right],\\ M_d^n(U^{h,n}) &= M+M^S(U^{h,n}). \end{aligned}$$

Our numerical test indicates that the above scheme is indeed stable, and comparison with previous benchmark results (Blankenbach et al. 1989; Travis et al. 1990) indicates its accuracy; for example, for the time-dependent convection problem of a basally heated Rayleigh-Benard convection model, a Rayleigh number of 10^5, with constant viscosity within 2 by 1 domain), we have a difference of less than 0.3% with the values in Table 5 of Travis et al. (1990)).

4.5 The inverse problem

Substantial uncertainties exist for the current conditions and past history of the mantle. Under our model for mantle convection, the earlier temperature (initial condition) and the rheological parameters are arguably among the most uncertain. Starting from an unknown initial temperature T^0 and viscosity parameters m, the geodynamic system evolves forward by the above equations, generating observables such as surface velocity history $U^n_{\text{obs}} = U^n$ and present day temperature $T_{\text{obs}} =$

T^{n_F}. Our goal is to recover T^0 and m from these observations. We follow the "discretize-then-optimize" approach, in contrast to the "optimize-then-discretize" approach. As discussed in Giles and Pierce (2000), because the exact gradient of the discrete objective function is obtained, the "discretize-then-optimize" ensures the optimization process can converge fully. Also it allows for a gradient check using finite differences, ensuring the correctness of the implementation, as shown later.

We define the discretized cost function as

$$
\begin{aligned}
J(\boldsymbol{T}, \boldsymbol{U}, m) &= J_F(T^{n_F}) + J_S(\boldsymbol{U}) + J_R(T^0) \\
&= \frac{\beta_F}{2}(T^{n_F} - T_{\text{obs}})^\intercal M (T^{n_F} - T_{\text{obs}}) + \sum_{n=0}^{n_F} \frac{\beta_S}{2}(U^n - U^n_{\text{obs}})^\intercal O (U^n - U^n_{\text{obs}}) \\
&+ \frac{\beta_R}{2}\left(T^0 - T_0^{\text{mean}}\right)^\intercal K \left(T^0 - T_0^{\text{mean}}\right),
\end{aligned}
\tag{4.10}
$$

where $\boldsymbol{T} = [T^0, \cdots, T^{n_F}]$ and $\boldsymbol{U} = [U^0, \cdots, U^m]$, J_F, J_S, and J_R denote the final temperature misfit, surface velocity misfit, and regularization respectively, with β_F, β_S and β_R the hyper-parameters controlling the weight of the different terms. T^0, m are the parameters we can tune for this optimization problem, where other terms in $\boldsymbol{T}, \boldsymbol{U}$ are constrained by the forward modeling (Eq. 4.9). M is the mass matrix, the matrix O denotes an operator that extracts surface degrees of freedom from the full velocity, and the Laplacian matrix K in the regularization term expresses our preference for smoothing initial conditions. T_0^{mean} is a given prior guess on the initial condition. Note that in this problem, we use a constant timestep, and time integration in surface misfit is replaced with a summation, with Δt absorbed into β_S just for convenience. Since the three terms have different units and magnitudes, we normalize them and define a new set of hyper-parameters $\alpha_F, \alpha_S, \alpha_R$ as

$$
\begin{aligned}
\beta_S &= \frac{\alpha_S}{\frac{1}{2}\sum_{i=0}^{n_F-1}\left(U^i_{\text{obs}}\right)^2}, \\
\beta_F &= \frac{\alpha_F}{\frac{1}{2}\left(T_{\text{obs}} - T_0^{\text{mean}}\right)^\intercal M \left(T_{\text{obs}} - T_0^{\text{mean}}\right)}, \\
\beta_R &= \frac{\alpha_R}{\frac{1}{2}\left(T_{\text{obs}} - T_0^{\text{mean}}\right)^\intercal K \left(T_{\text{obs}} - T_0^{\text{mean}}\right)}.
\end{aligned}
$$

The optimization problem (Eq. 4.10) can incorporate other potential constraints, such as bounds on parameters, which often can be enforced in many optimization algorithms. Also for positive viscosity parameters of large amplitude range, such as prefactor C, we use $\ln(C)$ as the actual parameter in our inversion.

4.6 Adjoint equation

Many previous studies follow the "optimize-then-discretize" approach, in which the authors derive a PDE for the adjoint variable first, and then discretize the PDE. We use a "discretize-then-optimize", where the adjoint equation is derived in a fully discrete formulation. The derivation is straightforward, as long as we consider the nonlinear dependencies between variables. The derivation starts with defining a Lagrangian by considering the forward modeling PDE constraints

$$
\begin{aligned}
L(\boldsymbol{T}, \boldsymbol{U}, \boldsymbol{P}, \boldsymbol{\Lambda}, \boldsymbol{V}, \boldsymbol{Q}, m) = J
&+ \sum_{n=0}^{n_F} \begin{bmatrix} V^n \\ Q^n \end{bmatrix}^\intercal \left(\begin{bmatrix} A(U^n, T^n, m) & B \\ B^\intercal & 0 \end{bmatrix} \begin{bmatrix} U^n \\ P^n \end{bmatrix} - \begin{bmatrix} FT^n \\ 0 \end{bmatrix} \right) \\
&+ \sum_{n=0}^{n_F-1} \Lambda^{h,n} \left[M_a^n T^{h,n} - M_b^n(U^n) T^n \right] \qquad (4.11) \\
&+ \sum_{n=0}^{n_F-1} \begin{bmatrix} V^{h,n} \\ Q^{h,n} \end{bmatrix}^\intercal \left(\begin{bmatrix} A(U^{h,n}, T^{h,n}, m) & B \\ B^\intercal & 0 \end{bmatrix} \begin{bmatrix} U^{h,n} \\ P^{h,n} \end{bmatrix} - \begin{bmatrix} FT^{h,n} \\ 0 \end{bmatrix} \right) \\
&+ \sum_{n=0}^{n_F-1} \Lambda^{n+1} \left(M_c^n(U^{h,n}) T^{n+1} - M_d^n(U^{h,n}) T^n \right)
\end{aligned}
$$

where $\boldsymbol{V}, \boldsymbol{Q}, \boldsymbol{\Lambda}$ are discrete adjoint velocity, pressure, and temperature, with superscript indicating the timestep. Then

$$
\frac{\partial L}{\partial U^n} = \beta_S O(U^n - U_{\text{obs}}^n) + \left(\frac{\partial A U^n}{\partial U^n} \right)^\intercal V^n + B Q^n - \left(\frac{\partial M_b^n}{\partial U^n} T^n \right)^\intercal \Lambda^{h,n} 1_{n<n_F}, \tag{4.12a}
$$

$$
\frac{\partial L}{\partial P^n} = B^\intercal V^n, \tag{4.12b}
$$

$$
\begin{aligned}
\frac{\partial L}{\partial T^n} = \beta_F M (T^{n_F} - T_{\text{obs}}) 1_{n=n_F} + \left(\frac{\partial A}{\partial T^n} U^n - F \right)^\intercal V^n - \left(M_b^n \right)^\intercal \Lambda^{h,n} 1_{n<n_F} \qquad (4.12c) \\
- \left(M_d^n \right)^\intercal \Lambda^{n+1} 1_{n<n_F} + \left(M_c^{n-1} \right)^\intercal \Lambda^n 1_{n>0} + \beta_R K \left(T^n - T_0^{\text{mean}} \right) 1_{n=0},
\end{aligned}
$$

$$
\frac{\partial L}{\partial U^{h,n}} = \left(\frac{\partial A U^{h,n}}{\partial U^{h,n}} \right)^\intercal V^{h,n} + B Q^{h,n} + \left(\frac{\partial M_c^n}{\partial U^h} T^{n+1} - \frac{\partial M_d}{\partial U^h} T^n \right)^\intercal \Lambda^{n+1}, \tag{4.12d}
$$

$$
\frac{\partial L}{\partial P^h} = B^\intercal V^{h,n}, \tag{4.12e}
$$

$$
\frac{\partial L}{\partial T^{h,n}} = (M_a^n)^\intercal \Lambda^{h,n} + \left(\frac{\partial A}{\partial T^{h,n}} U^{h,n} - F \right)^\intercal V^{h,n}, \tag{4.12f}
$$

where 1 denotes the indicator function.

Setting the derivatives to zero, we obtain the discrete adjoint equations for adjoint vectors. Solving the above adjoint Stokes equation sequentially, we obtain V^{n_F}, Q^{n_F}, then Λ^{n_F}, then V^{h,n_F-1}, Q^{h,n_F-1}, then Λ^{h,n_F-1}, and so on, to $V^{h,0}, Q^{h,0}$ then $\Lambda^{h,0}$, finally V^0, Q^0. To summarize the adjoint equations

$$\begin{bmatrix} \frac{\partial AU^n}{\partial U^n} & B \\ B^\intercal & 0 \end{bmatrix}^\intercal \begin{bmatrix} V^n \\ Q^n \end{bmatrix} = \begin{bmatrix} -\beta_S O(U^n - U^n_{\text{obs}}) + \left(\frac{\partial M_b^n}{\partial U^n} T^n\right)^\intercal \Lambda^{h,n} 1_{n<n_F} \\ 0 \end{bmatrix}, \tag{4.13a}$$

$$\left(M_c^{n-1}\right)^\intercal \Lambda^n 1_{n>0} = -\beta_F M(T^{n_F} - T_{\text{obs}}) 1_{n=n_F} - \left(\frac{\partial A}{\partial T^n} U^n - F\right)^\intercal V^n \tag{4.13b}$$

$$+ \left(M_b^n\right)^\intercal \Lambda^{h,n} 1_{n<n_F} + \left(M_d^n\right)^\intercal \Lambda^{n+1} 1_{n<n_F}$$

$$- \beta_R K \left(T^n - T_0^{\text{mean}}\right) 1_{n=0},$$

$$\begin{bmatrix} \frac{\partial AU^{h,n}}{\partial U^{h,n}} & B \\ B^\intercal & 0 \end{bmatrix}^\intercal \begin{bmatrix} V^{h,n} \\ Q^{h,n} \end{bmatrix} = \begin{bmatrix} -\left(\frac{\partial M_c^n}{\partial U^h} T^{n+1} - \frac{\partial M_d}{\partial U^h} T^n\right)^\intercal \Lambda^{n+1} \\ 0 \end{bmatrix}, \tag{4.13c}$$

$$(M_a^n)^\intercal \Lambda^{h,n} = -\left(\frac{\partial A}{\partial T^{h,n}} U^{h,n} - F\right)^\intercal V^{h,n}. \tag{4.13d}$$

In above equation, the coupling between forward and adjoint variables is a crucial part of the adjoint theory, as noted by Horbach et al. (2014). Comparing the above adjoint Eq. 4.13 with forward Eq. 4.9, we can see that the adjoint equations uses the convection velocity from the forward solution, and the effective viscosity does not depend on adjoint variables, thus adjoint equations are linear. Finally the gradient with respect T^0 is obtained by evaluating Eq. 4.12c, and gradient with respect to m is obtained by

$$\begin{aligned} \frac{\partial J}{\partial m} &= \frac{\partial L}{\partial m} \\ &= \sum_{n=0}^{n_F} \left[\frac{\partial}{\partial m} A\left(U^n, T^n, m\right) U^n\right]^\intercal V^n + \left[\frac{\partial}{\partial m} A\left(U^{h,n}, T^{h,n}, m\right) U^{h,n}\right]^\intercal V^{h,n} 1_{n<n_F}. \end{aligned}$$

In the above formulas, many matrices do not need to be assembled explicitly, and only their products with vectors are required. Detailed expressions for the partial derivatives are shown in the Appendix.

4.7 Gradient verification

As shown above, the derivation of the expressions for computing gradient follows a systematic procedure. But the equations are complicated and their implementation

ϵ	$T^{\intercal}_{perturb}\frac{\partial J}{\partial T^0}$	$\frac{\partial J}{\partial C}$	$\frac{\partial J}{\partial n}$	$\frac{\partial J}{\partial E}$
1e-02	3.5220e-02	-9.2172e-03	1.9622e-02	4.2110e-03
1e-03	4.0388e-02	-8.9323e-03	2.1406e-02	4.2795e-03
1e-04	4.0888e-02	-8.9032e-03	2.1580e-02	4.2863e-03
Adjoint	4.0944e-02	-8.9000e-03	2.1600e-02	4.2871e-03

Table 4.1: Gradient test for cylindrical descent problem.

into numerical solution can be prone to mistakes. We have attempted to derive our gradients as accurately as possible by limiting the number of approximations made. However, there are two places where approximations are necessary. First, because of the $\min$ function in the viscosity law, gradients do not exist at the bound point, so we set the gradient to vanish once it has reached the bounds. Secondly, in Eq. 4.5, the parameter τ in the SUPG scheme is a function of U, but since the Peclet number $|Pe| \gg 1$, τ depends only weakly on U, so we discard $\partial\tau/\partial U$ terms. In addition, the numerical solving for linear and nonlinear systems using iterative methods also introduces errors. Consequently, it is essential that we demonstrate the correctness of the gradient obtained from adjoint modeling. The finite difference test is the most straightforward way to accomplish this.

From the adjoint modeling we obtain $\partial J/\partial m$ and $\partial J/\partial T^0$. We can choose a random perturbation field T_{perturb}, and compare the directional derivatives

$$\frac{J(T+\epsilon T_{\text{perturb}}, m) - J(T,m)}{\epsilon} \sim T^{\intercal}_{\text{perturb}}\frac{\partial J}{\partial T^0},$$
$$\frac{J(T, m+\epsilon e_i) - J(T,m)}{\epsilon} \sim \frac{\partial J}{\partial m_i}.$$

As we reduce ϵ, the difference between left and right in above equation should become progressively smaller. Table 4.1 shows a typical case, where we tested gradients for temperature and several viscosity parameters. Indeed, as we reducing ϵ, the finite difference directional derivatives are approaching the ones from adjoint calculation.

4.8 Preconditioned LBFGS inversion

In addition to gradients, efficient solution methods for large-scale minimization problems such as Eq. 4.10 ideally also incorporate second-order derivatives (i.e., Hessians) of the cost functional with respect to the parameters. While second-order directional derivatives can be obtained through the solution of appropriately modified state and adjoint equations (sometimes called incremental equations) (Rat-

naswamy et al. 2015; Borzì and Schulz 2012), second-order derivative information can also be approximated using gradients used during the optimization algorithm. The Broyden-Fletcher-Goldfarb-Shanno (BFGS) update formula and its limited-memory variant (LBFGS) are prominent examples for this approach (Nocedal and Wright 2006). We use the LBFGS method, which starts from a positive definite and symmetric initial inverse Hessian estimate R_0, and computes rank-2 updates for the inverse Hessian approximation in every iteration. The resulting approximation in the n-th step, R_n, can then be used to compute an approximate Newton direction by

$$x_{n+1} = x_n - \lambda R_n g_n,$$

where x_n is the current point, g_n the gradient at x_n, and λ the step size derived from a line search. To calculate $R_n g_n$, a two loop recursion can be used (see Algorithm 7.4 of Nocedal and Wright (2006)), which only requires the application of R_0 to vectors and does not require stores of the inverse Hessian approximation (which is usually a dense matrix), but only stores a fixed number of gradients that arose during the optimization. In finite-dimensional optimization, one commonly uses a scaled identity matrix γI for R_0 , with γ an appropriately computed scalar. If a better approximation of the inverse Hessian (or a part of the inverse Hessian) is available, then it should be used for R_0. While we do not compute the Hessian of the misfit part of the cost functional in our problem, we explicitly know the Hessian of the regularization term for the initial temperature, namely the scaled Laplace matrix K. While K is usually a better approximation to the true Hessian than the scaled identity matrix, incorporating K^{-1} in R_0 also smooths the update $R_n g_n$, and thus avoids mesh artifacts in the update direction. This modification often accelerates the convergence of the minimization algorithm, as is illustrated later. To summarize, we use the inverse Hessian initialization

$$R_0 = \begin{bmatrix} \gamma_1 I & 0 \\ 0 & \gamma_2 K^{-1} \end{bmatrix},$$

where $\gamma_1 I$ corresponding to scalar parameters and $\gamma_2 K^{-1}$ corresponding to temperature components. In our implementation, we choose $\gamma_1 = \gamma$, and γ_2 such that $||R_0 g_n||_2 = ||\gamma g_n||_2$.

4.9 Sinking Cylinder

Our first example is that of a sinking cold cylinder (a circle in two dimensions) embedded in a homogeneous temperature background. Although simplified from

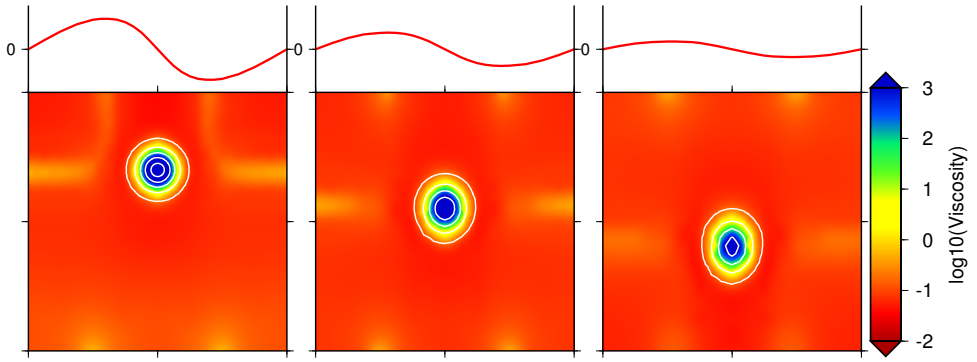

Figure 4.1: Forward simulation of the sinking cylinder model. The images show, from left to right, the effective viscosity (in log10 scale) at 0, 25, and 50 timesteps. Temperature contours for T=0.1, 0.3, 0.5, 0.7, and 0.9 are shown in white. The surface horizontal velocity is shown as a red curve (the scale does not correspond to physical dimensions and is thus ignored for simplicity).

the spatially and rheologically more complex subduction dynamics problem, the cylinder descent problem has many of the same characteristics. The initial temperature field is from a Gaussian function such that the temperature-induced variations in viscosity are smooth. We assume that the viscosity is temperature- and strain rate-dependent, with non-dimensional activation energy $E = 9$ and strain rate exponent $n = 2$, and we use a constant prefactor of $C = 1000$, as in Eq. 4.3. The Rayleigh number Ra is 10^6. In the forward model, the cylinder descends through the fluid layer with time while the surface velocity decreases (Fig. 4.1). From the computation, we record the horizontal surface velocity at each time step, and the temperature at the final time step as synthetic observational data.

Based on this observational data, we attempt to find the initial temperature and viscosity parameters. As an illustration of the method, we first conduct an inversion to recover the initial temperature, assuming viscosity parameters are known. Note that the effective viscosity is unknown due to the temperature and strain rate dependence of the viscosity law. As an initial guess for the inversion, we use the uniform temperature $T^0_{\text{guess}}(x) \equiv 1$, a quite uninformed guess. The pathway toward convergence is shown in Fig. 4.2. In the first row starting from the homogeneous guess T^0_{guess} in the first column, we obtain a final temperature T^{50} in the second column, which is unchanged from T^0 because the system is frozen at this guess. Then the third column shows the adjoint temperature Λ^{50}, indicative of the misfit between T^{50} and T^{50}_{data}. The fourth column shows Λ^1, the back propagated misfit to timestep 1 by solving adjoint equations. Because the adjoint variable convects using the forward modeling velocity, which is 0 in this case, Λ^1 coincides with Λ^{50}. The

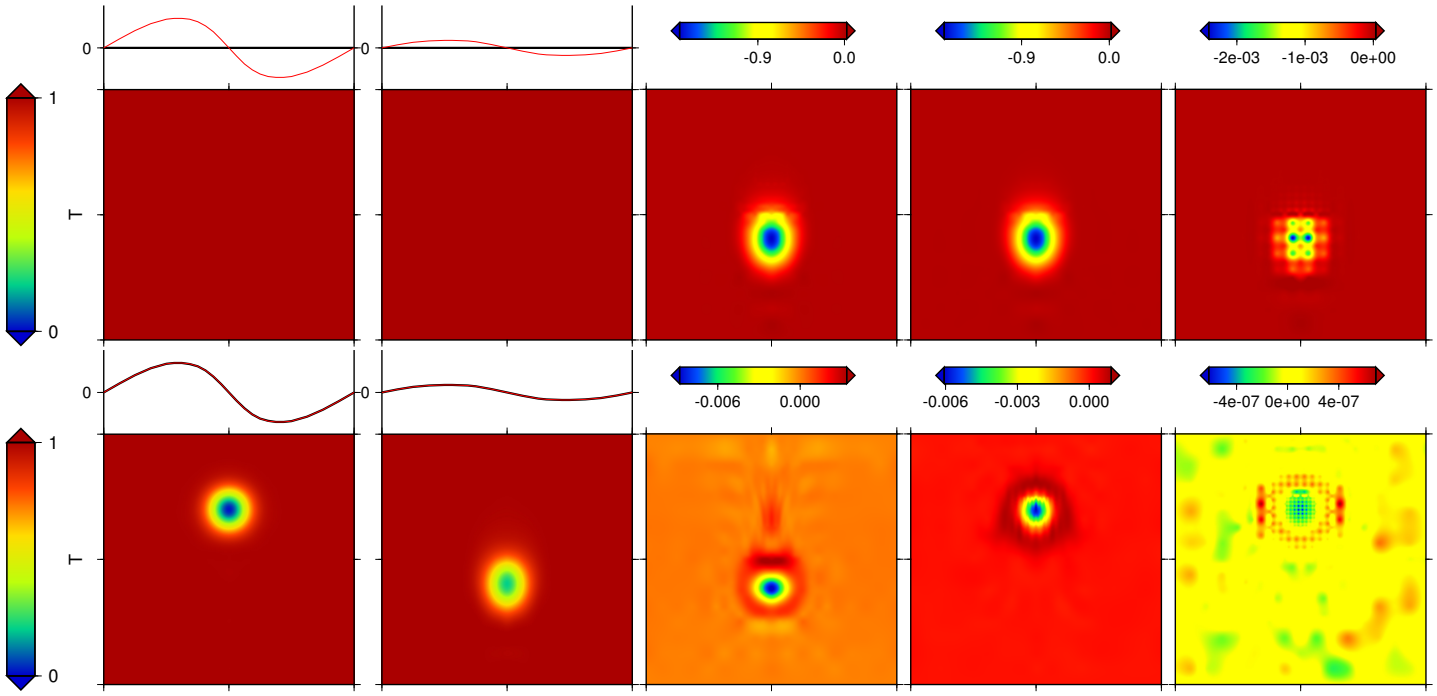

Figure 4.2: Inversion of the initial temperature for the falling cylinder problem. The two rows corresponding to the 1st, and 500th function evaluation. Five columns correspond to T^0, T^{50}, Λ^{50}, Λ^1, $\partial J/\partial T^0$ respectively. The curves above the first two columns show the surface velocity, with a red curve for the data, and a black curve for the model result from the current guess.

fifth column shows the discrete gradient $\partial J/\partial T^0$. Using this discrete gradient, we update our guess, and iterate the above process. In the second row, we show similar results after 500 function evaluations, where each function evaluation consists of a full forward and a full adjoint calculation. We can see now the recovered T^0, T^{50} and surface velocities are close to the true model, and also note that Λ^1 convects from Λ^{50} using the nearly correct backward velocity.

Note that the discrete gradients (fifth column, Fig. 4.2) show a distinctly mottled (or dotted) appearance. This mottled structure is related to the mesh. Since initial condition T^0 updates use this discrete adjoint, we also observe this mottled appearance in the reconstructed initial condition (Fig. 4.3), although eventually the mottled structure decays away.

Since this mottled structure is related to the mesh, if we apply M^{-1} or K^{-1} to the discrete adjoint, this mottled structure will vanish (Fig. 4.4). The preconditioned LBFGS described above does not introduce this mottled structure. Since the degree of smoothing may control the pathway and degree of convergence, we use a

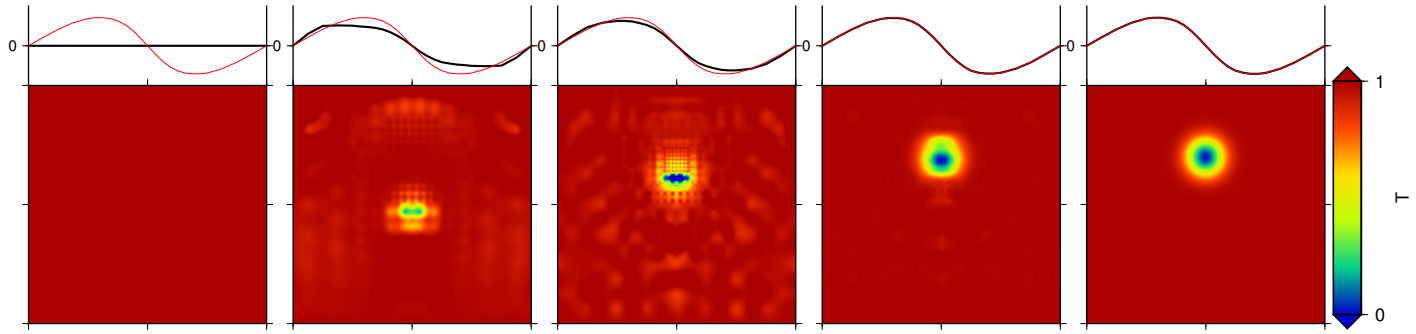

Figure 4.3: Reconstructed T^0 at 2, 20, 70, 200 and 500th function evaluation.

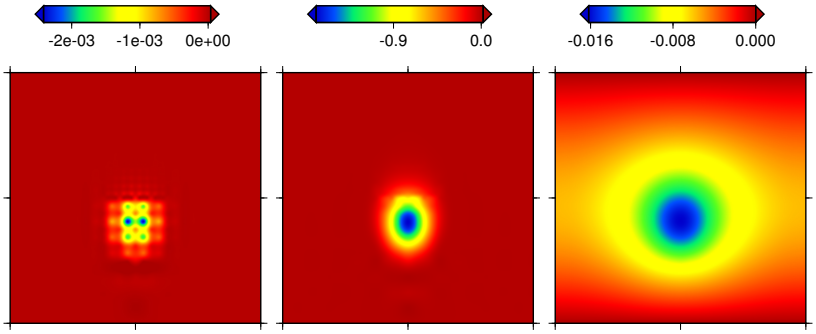

Figure 4.4: $\frac{\partial J}{\partial T^0}$, $M^{-1}\frac{\partial J}{\partial T^0}$, and $K^{-1}\frac{\partial J}{\partial T^0}$, showing how M^{-1} and K^{-1} remove the mesh effects.

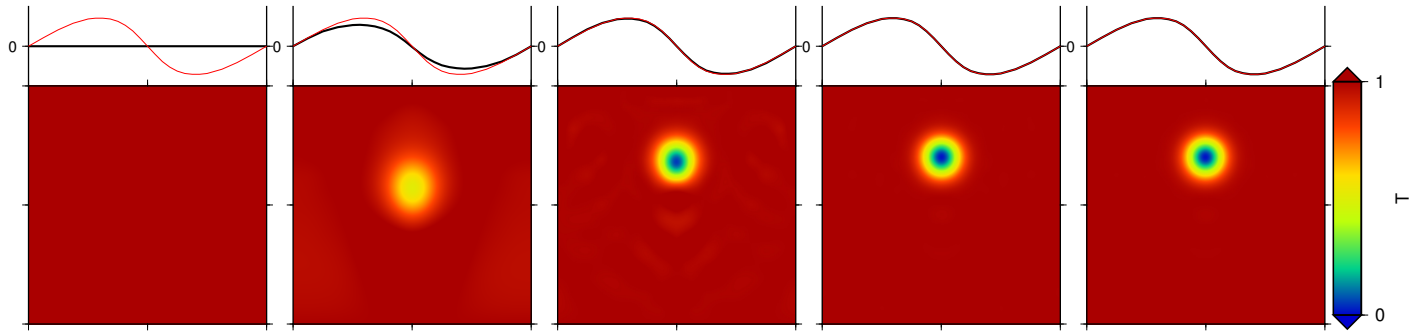

Figure 4.5: T^0 at 2, 20, 70, 200 and 500th function evaluation, use K^{-1} preconditioned LBFGS.

preconditioned LBFGS with a K^{-1} preconditioner. Essentially, this preconditioner enforces a smoothing update (Fig. 4.5).

For this problem, the LBFGS method with and without this preconditioner both converge, as demonstrated by the several orders of magnitude reduction in misfit and gradient (see Fig. 4.6). But the approach with the preconditioner achieves a faster convergence. Note that oscillations in the misfit and gradient norm curve are due to the line search in the LBFGS method.

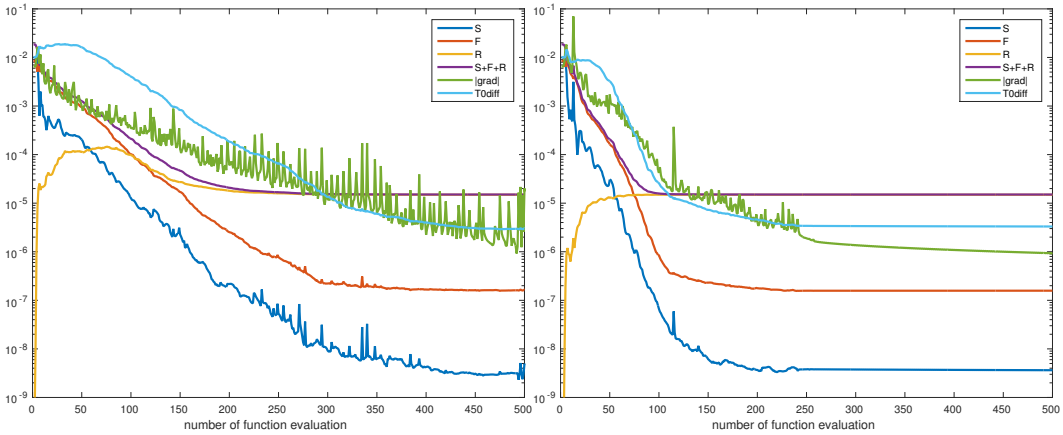

(a) LBFGS (b) LBFGS with preconditioner

Figure 4.6: Error reduction for cylinder model using LBFGS without (a) and with (b) preconditioner. The curves correspond to surface misfit J_S, final temperature misfit J_F, regularization term J_R , total cost $J = J_S + J_F + J_R$ and norm of the gradient $|\partial J/\partial T^0|$, and the recovered initial temperature misfit $(T^0_{guess} - T^0_{true})^\top M(T^0_{guess} - T^0_{true})$ respectively.

Instead of assuming that the parameters of the viscosity are known, as in the prior case, we now assume that they are unknown and recover them in our inversion. Instead of assuming known temperature and fitting a single velocity profile for a single time (i.e. the so-called instantaneous inversion) in Worthen et al. (2014) and Ratnaswamy et al. (2015), we incorporate the entire surface velocity data history and the final temperature. For the recovery of the viscosity parameters, we first conduct an inversion for the prefactor C and nonlinear exponent n, with true initial temperature and other parameters given. The recovery seems perfect in this case, where the error J_S and J_F decrease to almost 0, and C and n converge to the true values in less than 40 function evaluations (Fig. 4.7).

Having demonstrated recovery of the initial temperature assuming the constitutive parameters and recovery of the constitutive parameters assuming the initial temperature, we now attempt a joint inversion of the initial temperature and the two viscosity parameters, C and n (having true values of 1000 and 2, respectively) with the other parameter assumed to be known correctly. In the first case, starting from a guess with a constant temperature ($T^0_{\text{guess}} = 1$) and constitutive parameters $C_{\text{guess}} = 300$ and $n_{\text{guess}} = 2.5$, the inversion stops after 220 function evaluation, converging to $C = 993.0$ and $n = 1.996$. In the second case, starting from $T^0_{\text{guess}} = 1$ and $C_{\text{guess}} = 500$ and $n_{\text{guess}} = 2.5$, the inversion stops after 280 function evaluation, converging to $C = 1416.3$ and $n = 2.135$. The error reduction and inversion history

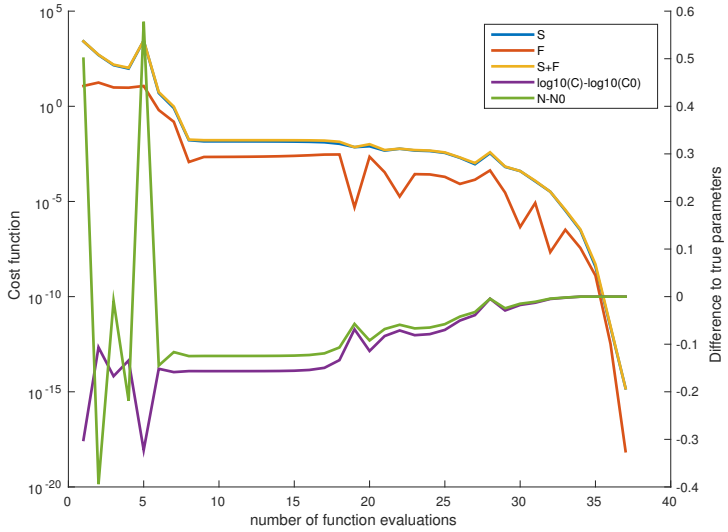

Figure 4.7: Error reduction and convergence of C and n for cylinder model. J_S, J_F and $J_S + J_F$ are shown in left axis, while $\log(C) - \log(C_0)$ and $n - n_0$ are shown in right axis, with C_0, n_0 are the true values of prefactor and nonlinear exponent.

for C and n differs for the two joint inversion cases (Fig. 4.8). Although the two cases start from similar guesses and have comparable order of their error reduction, they lead to two different recovered C and n. This suggests a strong trade off between C and n for this simple model setup. To show the two different recovered C and n fit the data equally well, we observe that the recovered temperature, surface velocity, and corresponding effective viscosity for the two cases are nearly identical (Fig. 4.9). We also compare the total viscous dissipation at initial step, defined as $\int 2\eta_{\text{eff}}(\boldsymbol{u}, T)D(\boldsymbol{u}) : D(\boldsymbol{u})d\Omega$, for these two cases. The first case have a dissipation of 1.883×10^8, the second case 1.886×10^8, and the true model 1.889×10^8, essentially identical within error.

To understand the differences occurring in the previous two cases, we explore the influence of the global parameters C and n in the inversion. We assume the initial temperature to be known, vary C and n, and calculate the forward solution and evaluate the cost function. To simplify further, we plot J_S for an instantaneous ($n_F = 0$) model (Fig. 4.10a and b). We can see a narrow flat valley of cost exists along a particular direction in the C, n plane, indicative of a strong trade-off in this direction. Similar results hold for J_F, and for time dependent model (e.g., $n_F = 50$). Note that because no noise is added to the observation, J_S is exactly 0 at the true parameter point. In real data cases, this is not likely to happen.

If we plot the convergence path for the C and n only inversion (Fig. 4.7) and two

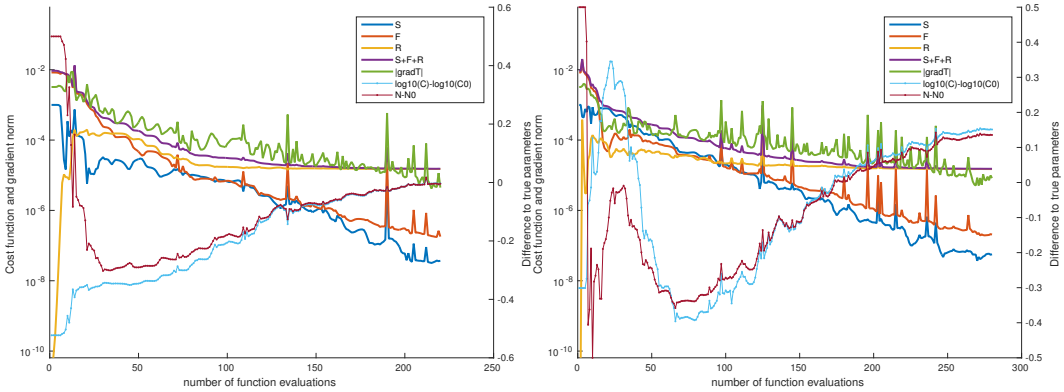

(a) Joint inversion case 1 (b) Joint inversion case 2

Figure 4.8: Error reduction and C, n recover history for two joint inversion cases with different initial guess. Legend meaning is the same as in Fig. 4.6 and Fig. 4.7. Note that error reduction is of similar order, while the recovered C and n follow different path.

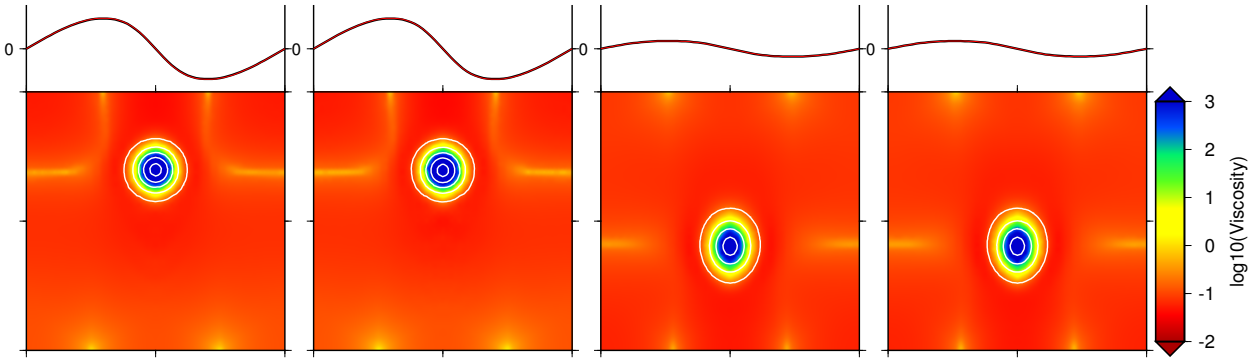

Figure 4.9: Recovered effective viscosity, temperature contour and surface velocity for two joint inversion cases. The 1st and 3rd plots correspond to 0 and 50 time step of the last function evaluation in case 1. The 2nd and 4th plots correspond to 0 and 50 time step of the last function evaluation in case 2.

T^0, C, n joint inversion (Fig. 4.8) along with this cost function value, we find that the optimization algorithm spends many iterations navigating within this "trade-off valley" (Fig. 4.10c). With initial temperature known, the iterations face into the narrow valley and find the true minimum (black curve). If the temperature also needs to be recovered, the trade-off valley changes with every time T^0_{guess} changes, making it difficult to find the true minimum.

In this cylinder model, the strong trade-off is partially due to the simplicity of this problem, where prefactor C and nonlinear exponent n seem to have similar influence on effective viscosity. In more complex model, for example if n is increased from 2 to 3, the role of C and n on effective viscosity will have more differences, and the

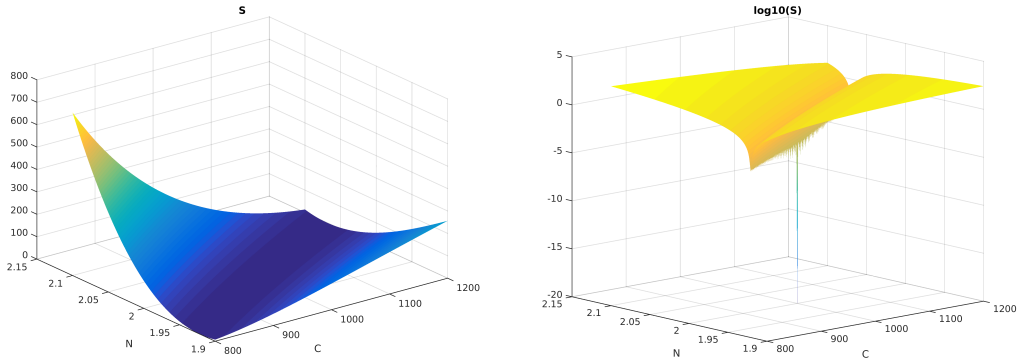

(a) (b)

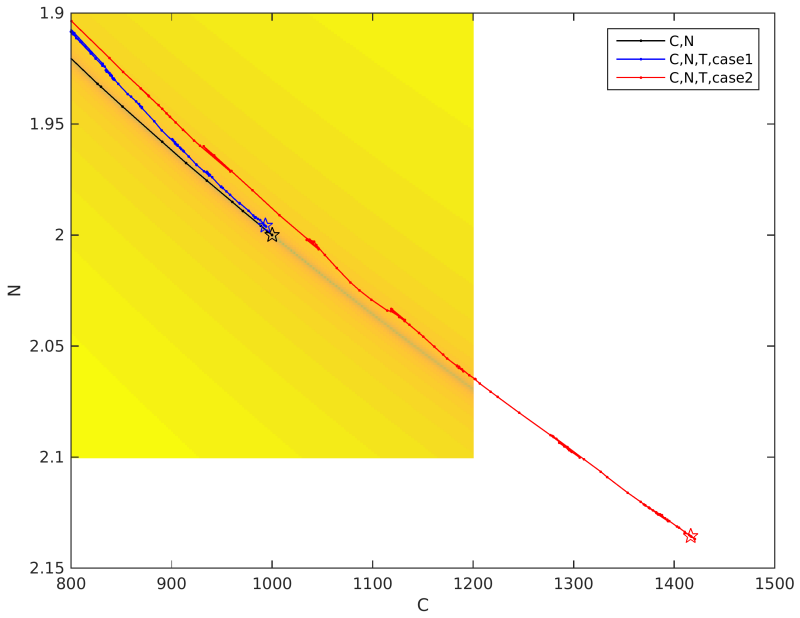

(c)

Figure 4.10: (a) J_S and (b) $\log_{10}(J_S)$ as a function of C, N, for a $n_F = 0$, known true T^0case. (c) Inversion pathes for C, n in three inversion cases, where the color image shows $\log_{10}(J_S)$. Black curve corresponds to C, n only inversion in Fig. 4.7. Blue and red curves correspond to two jointly inversion cases in Fig. 4.8 respectively.

trade-offs are likely to be less.

4.10 Subduction

Plate motions are intimately tied to subduction and changes in plate motion and thought to be at least partially, if not primarily, controlled by changes in subduction (including slab dip, the age of the subducting plate, and the depth of slab penetration) (Zhong and Gurnis 1995a; Billen 2008; Stadler et al. 2010; Gerya 2011). Consequently, we have a model setup in which changes in plate motion and subduction are important aspects of the dynamics, while being sufficiently compact that we can explore the forward and inverse problem without an overwhelming computational burden. We focus on an important component of the time-dependence of plate motions, namely the progressive migration of a mid-ocean ridge toward an oceanic trench, as occurred off the west coast of North America with the eastward motion of the Farallon-Pacific ridge toward the subduction below the continent during the Cenozoic (Atwater 1970). Burkett and Billen (2009) formulated convection models meant to study this process, specifically tailored to the Miocene evolution of Baja California in which the Farallon-Pacific ridge stalled before reaching the trench.

Within a domain of 2000 km$\times 1000$ km, we set a mid-ocean ridge 500 km to the left of a subducting slab with an initial dip of about 45° (see Fig. 4.11a). The thermal structure of the lithosphere is derived from a half-space cooling model, assuming that the plate age linearly increases from 0 Myr at ridge to 30 Myr at the trench and from the ridge to the left edge of domain. The upper plate is assumed to be initially 30 Myr. The initial slab was created by assuming its temperature gradually warms with depth, in which a weak zone curves around along the top of the thermal slab similar to the implementation in Ratnaswamy et al. (2015). The viscosity in the upper mantle is non-Newtonian, with $n_1 = 3$, while in the lower mantle it is Newtonian, $n_2 = 1$. The temperature dependence of viscosity is controlled by a non-dimensional activation energy with $E = 9$ through the whole domain. The prefactor is $C_1 = 3 \times 10^4$ in upper mantle (<410 km), $C_2 = 6 \times 10^4$ in the transition zone (410 to 660 km), and $C_3 = 2 \times 10^3$ in lower mantle (>660 km).

As expected from similar published models (Burkett and Billen 2009), the center oceanic plate moves to the right with a velocity of 55 to 60 mm/yr, initially (see Fig. 4.11a). The large induced shear in the upper mantle below the oceanic lithosphere and around the slab lowers the effective viscosity to between $\sim 10^{18}$ and $\sim 10^{19}$ Pa-s. Initially the slab falls within the upper mantle and with a gap between

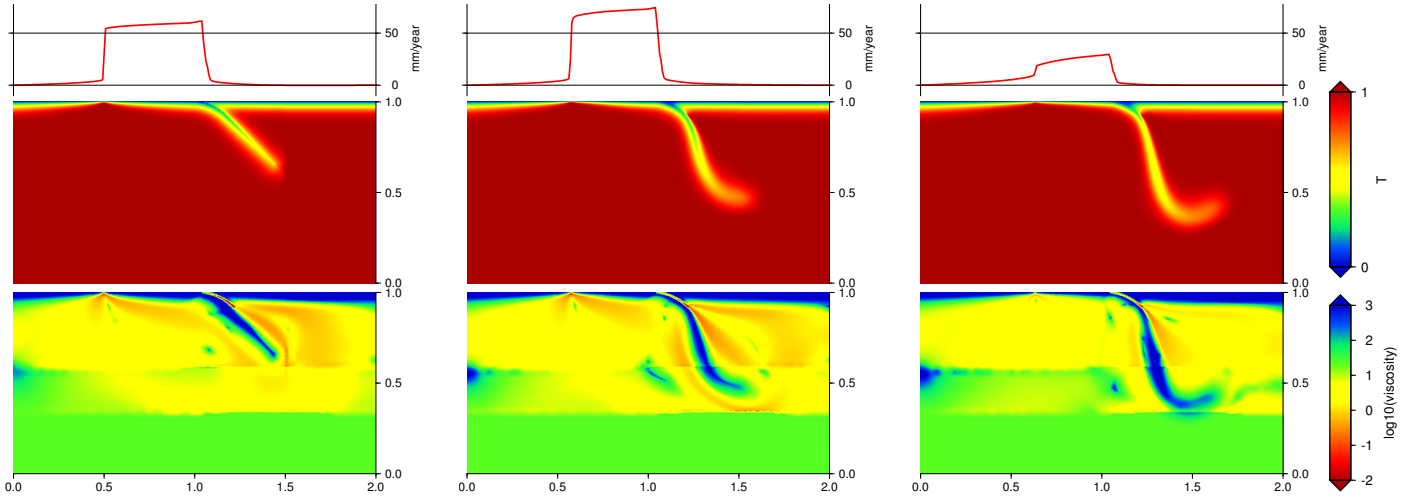

(a) (b) (c)

Figure 4.11: Subduction forward modeling at 0, 25, and 50th timestep, corresponding to 0 Myr, 3.2 Myr, and 6.4 Myr respectively. In each time step, we show the surface velocity, the temperature field, and the effective viscosity. Note that viscosity is normalized by a reference value of 10^{20} Pa·s.

the base of the slab and the top of the high viscosity lower mantle, the plate velocity increases to just over 70 mm/yr during a 3.2 Myr time period (Fig. 4.11b). The slab descends nearly vertically, and since the weak zone for the plate interface does not move, the slab dip increases as the slab descends, and the base of the slab bends as it starts to sense the high viscosity lower mantle. During this interaction with the lower mantle, slab descent slows and the subducting plate velocity decreases to about 2-3 cm/yr at 6.4 Myr (Fig. 4.11c). The slab has changed from its initial configuration in terms of its dip, depth of penetration, and morphology. This final thermal structure (Fig. 4.11c) is now one of the data to be used in the inversion.

As in the cylinder model, we first conduct a initial temperature only inversion given, assuming that the true viscosity parameters are known. During the inversion, we choose a half space cooling model as the first guess of the initial temperature. Here, we just use the true cooling age for simplicity. The cooling age in practice can be constructed from surface velocity history, as in many plate reconstruction models. Compared to the previous cylinder sinking problem, the subduction inversion problem is substantially more difficult, presumably because the larger viscosity contrasts near the ridge and trench and associated mesh refinements there. For example, we computed cases with the LBFGS algorithm without a preconditioner for this initial condition only inversion; the progress of the inversion was slow, and a line

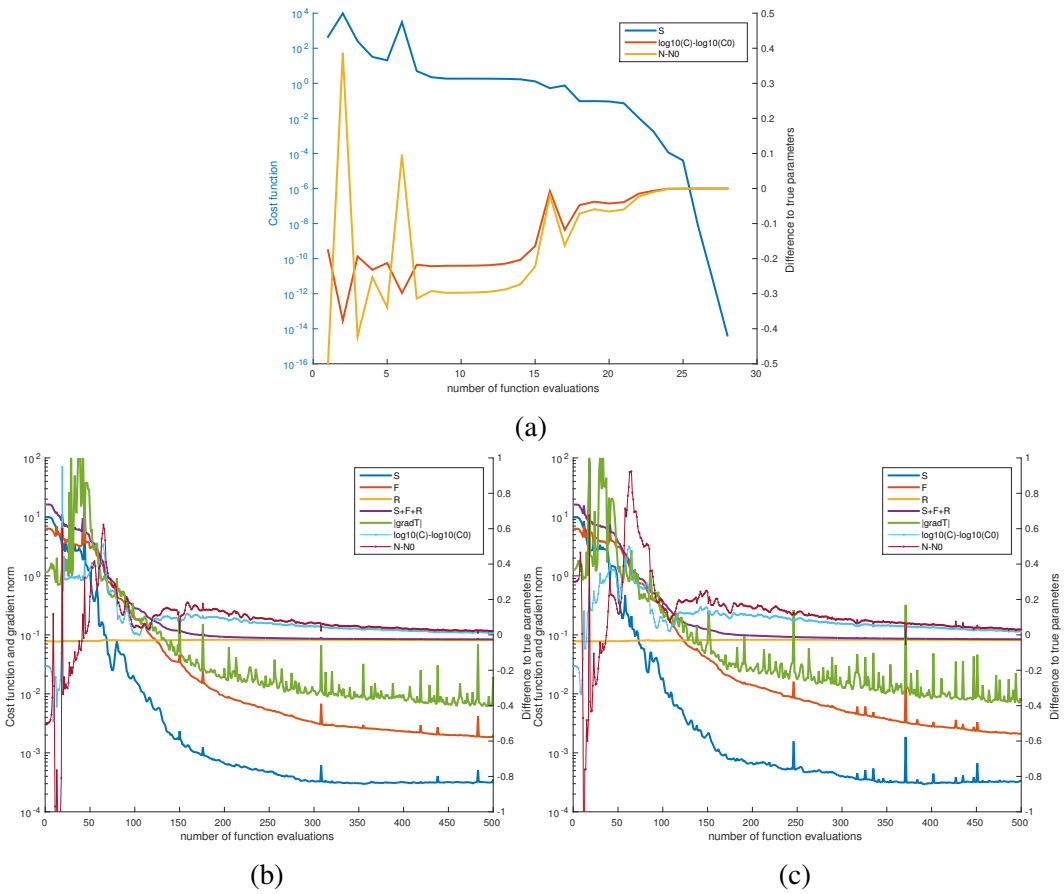

Figure 4.12: Error reduction and C_1 and n_1 recovery pathes for subduction inversions: (a) Inversion of C_1, n_1 with initial temperature and other parameters known; (b) Case 1 and (c) Case 2 for joint inversion of T^0, C_1, n_1 given other parameters.

search in the LBFGS algorithm failed before it could make a substantial error reduction. However, when we switch to the preconditioned LBFGS, the inversion greatly improves. The misfit $J_S$and J_F achieve 4 order of magnitude of error reduction, indicating fitting of the data is good. The recovered initial temperature is also near that of the true model.

We then conduct a two parameters inversion, the prefactor C_1 in the upper 410km, and nonlinear exponent n_1 in the upper mantle, with initial temperature and other parameters known correctly. The results are good, as expected from cylinder model (Fig. 4.12a).

Finally, we conduct a joint inversion of T^0, C_1, n_1, starting from two sets of different guesses. In both cases, the starting guess for initial temperature is still the half space cooling model mentioned before. In the first joint inversion case, we choose a guess of $C_1 = 2\times10^4$ and $n_1 = 2.5$; in the second case, we choose a guess of $C_1 = 2\times10^4$

	True C_1, n_1	Init guess C_1, n_1	# of fvals	Recovered C_1, n_1
C_1, n_1only inversion	$3 \times 10^4,\ 3$	$(2 \times 10^4,\ 2.5)$	28	$(3.0000 \times 10^4,\ 3.000)$
T^0, C_1, n_1inversion case 1	$3 \times 10^4,\ 3$	$(2 \times 10^4,\ 2.5)$	500	$(3.0757 \times 10^4,\ 3.020)$
T^0, C_1, n_1inversion case 2	$3 \times 10^4,\ 3$	$(2 \times 10^4,\ 3.3)$	500	$(3.1383 \times 10^4,\ 3.030)$

Table 4.2: Summary of recovered C_1, n_1 for three cases in Fig. 4.12.

and $n_1 = 3.3$. For recovered C_1 and n_1, both cases show good convergence to true value (Fig. 4.12b and c), although not exactly reach the true value due to trade off and small error in recovered initial temperature (see summary in Table 4.2).

We plot the recovery process of surface velocity, temperature, and viscosity for the first joint inversion case in Fig. 4.13 (the second joint inversion case is similar). The initial guess (1st function evaluation) does not fit the surface velocity and final temperature. After 50 function evaluations, the shape of a subducted slab appears from the earlier blurry cool region, while the fit to surface velocity and final temperature improves. Finally, after 500 function evaluations, the fit to data becomes quite good, and the recovered initial temperature is also near the true model.

4.11 Discussion and summary

Our results indicate that, given scalar viscosity parameters in the constitutive relation (note that the effective viscosity itself is still unknown because of the temperature and strain-rate dependence of viscosity, in contrast with previous studies), by fitting the final temperature and surface velocity history, the initial condition of our model can be recovered well, even starting from a quite uninformed initial guess. This confirms the finding in Horbach et al. (2014), where they notice a strong global minimum exists for initial condition inversion problem. We then demonstrated by giving the true initial temperature, the two viscosity parameters (prefactor in the viscosity law and the non-linear exponent) we considered can converge to the true value, even under quite strong "trade off" as shown in the deep flat valley of the cost function. Our joint inversion of initial temperature and viscosity parameters shows that, while initial condition and effective viscosity can be reasonably recovered, the viscosity parameters themselves may fail to converge to true values under "trade off". We think this is due to the ill-posedness of the inversion problem. Further study, such as calculation of Hessian, or using a Bayesian framework by considering prior information would help to evaluate the trade off, as in Ratnaswamy et al. (2015).

In our tests, we conduct so called "inversion crime" because we use the same code to generate observations as we do for the inversion, while adding no noise to the

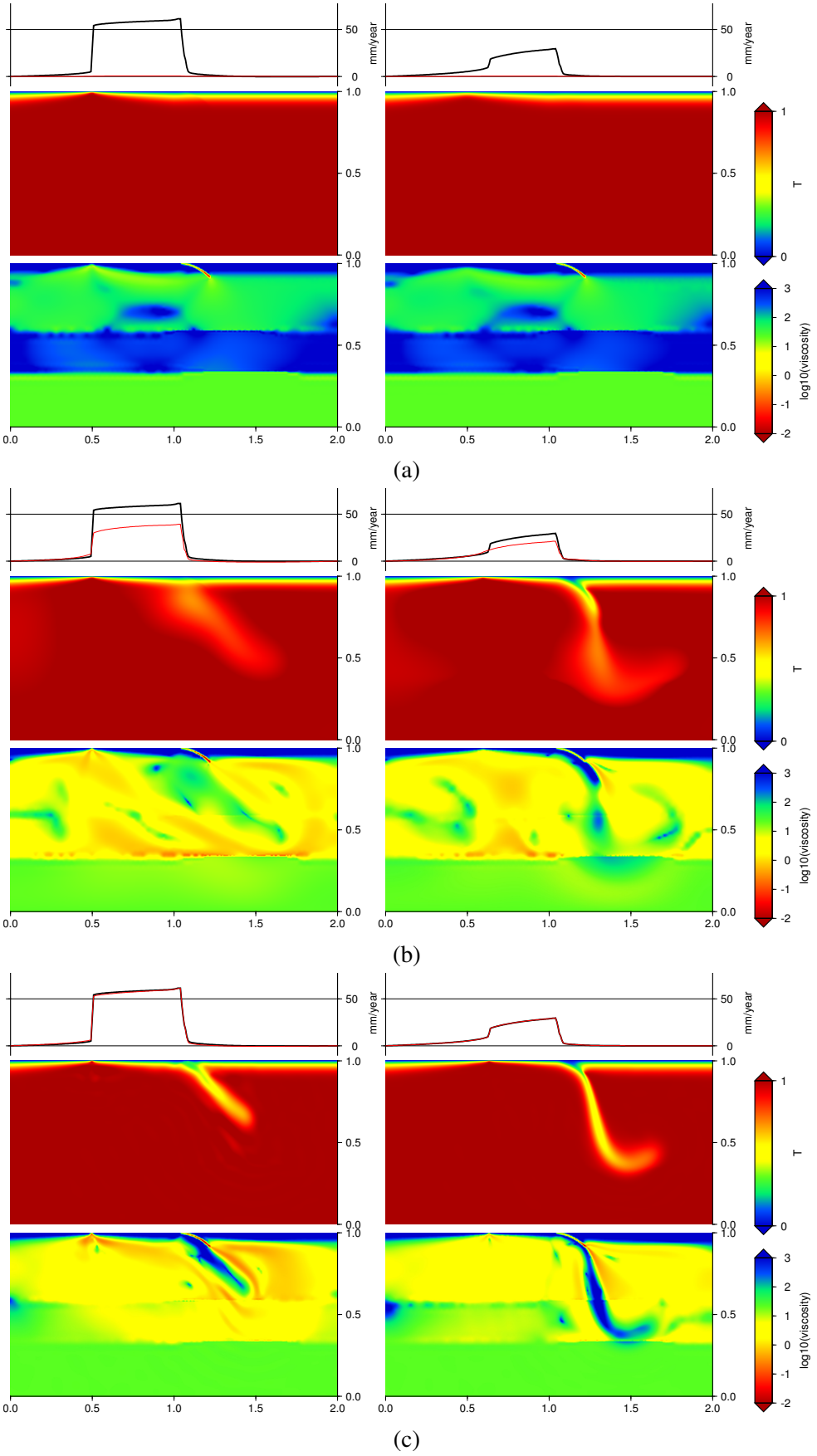

Figure 4.13: T^0, C_1, n_1 inversion with preconditioned LBFGS. The rows correspond to 1, 50, and 500th function evaluation, with left column correspond to 0th time step and right column correspond to 50th time step.

observations. Thus our tests is mainly used to validate the correctness of our implementation, and to develop better optimization schemes. But the subduction model we considered can be immediately extended to real data case. In the work by Burkett and Billen (2009), they studied the ridge-trench interaction in Baja California, and recovered subduction and detachment history of the slab, by computing many forward cases that explore the effects of many parameters, such as subducted slab length, distance of the ridge from the trench, shear zone strength and yield stress. It will be helpful to to determine the ability to recover these parameters using an adjoint inversion. For example, the inversion may produce an initial temperature condition where subducted slab length and distance of the ridge can be measured directly, and viscosity parameters involving shear zone strength and yield stress automatically.

Many works still need to be done before the inversion approach described here can be used in large scale three dimensional inversion. Firstly, a good initial guess of temperature will accelerate the optimization. Many methods, for example, simple backward integration (Liu and Gurnis 2008) and data assimilation (Bower et al. 2015), can potentially provide a better guess than the half space cooling guess we used here. Secondly, second order methods, at least just for scalar viscosity parameters (e.g., Ratnaswamy et al. 2015), can also speed up the optimization. Finally, there are also several variants to our direct joint inversion to be tested. For example, we may first recover the viscosity parameters just using present day observation as in Ratnaswamy et al. (2015), then constrain the initial temperature assuming these recovered viscosity parameters. We can also do an stage-wise inversion as in Ismail-Zadeh et al. (2004), where instead of directly recovering temperature in distinct past in one inversion, we conduct many small time-span inversions to recovered temperature. Although not exactly equivalent to inversion discussed here, these two variants may potentially speed up the recovery.

Acknowledgements

DL and MG were supported by the National Science Foundation under EAR-1247022. We would like to thank Prof. Mark Simons at Caltech for comments and suggestions.

Appendix A. Calculation of $\frac{\partial(AU)}{\partial U}$

This matrix G is used in solving the nonlinear Stokes equation in forward modeling and adjoint modeling. It can be written as

$$\begin{aligned}\left[\frac{\partial AU}{\partial U}\right]_{ij} &= \frac{\partial A_{ik}U_k}{\partial U_j} \\ &= A_{ij} + \frac{\partial A_{ik}}{\partial U_j}U_k \\ &= A_{ij} + \int 2\frac{\partial \eta_{\text{eff}}}{\partial U_j} D(\phi_i^u) : D(\phi_k^u U_k) d\Omega \\ &= A_{ij} + \int 2\frac{\partial \eta_{\text{eff}}}{\partial U_j} D(\phi_i^u) : D(u) d\Omega,\end{aligned}$$

where $\boldsymbol{u} = \phi_k^u U_k$ is the continuous function from discrete U.

Because $\eta_{\text{eff}} = \eta_{\min} + \min\left(\frac{\sigma_{\text{yield}}}{2\sqrt{\varepsilon_{\text{II}}}}, W\min\left(\eta_{\max}, \eta\right)\right)$, η_{eff} can only has three possible cases, and ignoring the discontinuous point where gradient doesn't exist, the gradient is

$$\frac{\partial \eta_{\text{eff}}}{\partial U_j} = \begin{cases} \frac{1-n}{2n}\frac{\eta_{\text{eff}}-\eta_{\min}}{\varepsilon_{\text{II}}}\left(D(\boldsymbol{u}) : D(\phi_j^u)\right) & , \eta_{\text{eff}} = \eta_{\min} + W\eta; \\ 0 & , \eta_{\text{eff}} = \eta_{\min} + W\eta_{\max}; \\ -\frac{1}{2}\frac{\eta_{\text{eff}}-\eta_{\min}}{\varepsilon_{\text{II}}}\left(D(\boldsymbol{u}) : D(\phi_j^u)\right) & , \eta_{\text{eff}} = \eta_{\min} + \frac{\sigma_{\text{yield}}}{2\sqrt{\varepsilon_{\text{II}}}}. \end{cases}$$

Appendix B. Calculation of $\left(\frac{\partial AU}{\partial T}\right)^{\mathsf{T}} V$,$\left(\frac{\partial M^S T}{\partial U}\right)^{\mathsf{T}} \Lambda$, $\left(\frac{\partial CT}{\partial U}\right)^{\mathsf{T}} \Lambda$,$\left(\frac{\partial C^S T}{\partial U}\right)^{\mathsf{T}} \Lambda$

These terms exist in the discrete adjoint equation. Let $\boldsymbol{v}, \lambda, \boldsymbol{u}, \tilde{T}$ be the continuous function corresponding to discrete V, Λ, U, T, then

$$\begin{aligned}\left[\left(\frac{\partial AU}{\partial T}\right)^{\mathsf{T}} V\right]_k &= V_i \frac{\partial A_{ij}U_j}{\partial T_k} \\ &= V_i \frac{\partial A_{ij}U_j}{\partial \tilde{T}}\frac{\partial \tilde{T}}{T_k} \\ &= V_i \frac{\partial\left[\int 2\eta_{\text{eff}} D(\phi_i^u) : D(\phi_j^u) d\Omega\right] U_j}{\partial \tilde{T}}\phi_k^T \\ &= \int 2\frac{\partial \eta_{\text{eff}}}{\partial \tilde{T}} D(\phi_i^u V_i) : D(\phi_j^u U_j)\phi_k^T d\Omega \\ &= \int 2\frac{\partial \eta_{\text{eff}}}{\partial \tilde{T}} D(\boldsymbol{v}) : D(\boldsymbol{u})\phi_k^T d\Omega,\end{aligned}$$

where

$$\frac{\partial \eta_{\text{eff}}}{\partial \tilde{T}} = \begin{cases} -EW\eta & , \eta_{\text{eff}} = \eta_{\min} + W\eta; \\ 0 & , \eta_{\text{eff}} = \eta_{\min} + W\eta_{\max}; \\ 0 & , \eta_{\text{eff}} = \eta_{\min} + \frac{\sigma_{\text{yield}}}{2\sqrt{\varepsilon_{\text{II}}}}. \end{cases}$$

Also

$$\begin{aligned}\left[\left(\frac{\partial M^S T}{\partial U}\right)^{\mathsf{T}}\Lambda\right]_k &= \Lambda_i \frac{\partial M^S_{ij} T_j}{\partial U_k} \\ &= \Lambda_i \frac{\partial\left[\int \tau\left(\boldsymbol{u}\cdot\nabla\phi_i^T\right)\phi_j^T d\Omega\right]}{\partial U_k} T_j \\ &= \int \tau\left(\phi_k^u\cdot\nabla\lambda\right)\tilde{T}d\Omega,\end{aligned}$$

and

$$\begin{aligned}\left[\left(\frac{\partial C T}{\partial U}\right)^{\mathsf{T}}\Lambda\right]_k &= \Lambda_i \frac{\partial C_{ij} T_j}{\partial U_k} \\ &= \Lambda_i \frac{\partial\left[\int \phi_i^T \boldsymbol{u}\cdot\nabla\phi_j^T d\Omega\right]}{\partial U_k} T_j \\ &= \int \lambda\phi_k^u\cdot\nabla\tilde{T}d\Omega,\end{aligned}$$

and

$$\begin{aligned}\left[\left(\frac{\partial C^S T}{\partial U}\right)^{\mathsf{T}}\Lambda\right]_k &= \Lambda_i \frac{\partial C^S_{ij} T_j}{\partial U_k} \\ &= \Lambda_i \frac{\partial\left[\left(\tau\boldsymbol{u}\cdot\nabla\phi_i^T\right)\left(\boldsymbol{u}\cdot\nabla\phi_j^T\right)\right]}{\partial U_k} T_j \\ &= \int \tau\left(\lambda\phi_k^u\cdot\nabla\tilde{T}+\tilde{T}\phi_k^u\cdot\nabla\lambda\right)d\Omega.\end{aligned}$$

Appendix C. The gradient $\frac{\partial A}{\partial m}$

For $m = C,\ E,\ n$, we have

$$\left[\begin{array}{ccc}\frac{\partial\eta_{\text{eff}}}{\partial C} & \frac{\partial\eta_{\text{eff}}}{\partial E} & \frac{\partial\eta_{\text{eff}}}{\partial n}\end{array}\right] = \begin{cases}\left[\begin{array}{ccc} W\frac{\eta}{C}, & (0.5-T)W\eta, & -\frac{\ln\epsilon_{\text{II}}}{2n^2}W\eta\end{array}\right] & ,\eta_{\text{eff}} = \eta_{\min} + W\eta; \\ 0 & ,\eta_{\text{eff}} = \eta_{\min} + W\eta_{\max}; \\ 0 & ,\eta_{\text{eff}} = \eta_{\min} + \frac{\sigma_{\text{yield}}}{2\sqrt{\varepsilon_{\text{II}}}},\end{cases}$$

and for $m = \ln C$, then $C = e^m$, and

$$\frac{\partial\eta_{\text{eff}}}{\partial m} = \frac{\partial\eta_{\text{eff}}}{\partial C}\frac{\partial C}{\partial m} = \frac{\partial\eta_{\text{eff}}}{\partial C}C,$$

then finally

$$\left(\frac{\partial A}{\partial m}\right)_{ij} = \int 2\frac{\partial\eta_{\text{eff}}}{\partial m}D(\phi_i^u) : D(\phi_j^u)d\Omega.$$

References

Atwater, T. (1970). "Implications of Plate Tectonics for the Cenozoic Tectonic Evolution of Western North America". In: *Geological Society of America Bulletin* 81.December, pp. 3513–3536. ISSN: 00167606. DOI: 10.1130/0016-7606(1970)81 (cit. on p. 108).

Bangerth, W., R. Hartmann, and G. Kanschat (2007). "deal.II—A general-purpose object-oriented finite element library". In: *ACM Transactions on Mathematical Software* 33.4, 24–es. ISSN: 00983500. DOI: 10.1145/1268776.1268779 (cit. on p. 92).

Baumann, T.S. and Boris J.P. Kaus (2015). "Geodynamic inversion to constrain the non-linear rheology of the lithosphere". In: *Geophysical Journal International* 202.2, pp. 1289–1316. ISSN: 0956-540X. DOI: 10.1093/gji/ggv201 (cit. on p. 88).

Billen, Magali I. (2008). "Modeling the Dynamics of Subducting Slabs". In: *Annual Review of Earth and Planetary Sciences* 36.1, pp. 325–356. ISSN: 0084-6597. DOI: 10.1146/annurev.earth.36.031207.124129 (cit. on pp. 88, 108).

Billen, Magali I. and Greg Hirth (2007). "Rheologic controls on slab dynamics". In: *Geochemistry, Geophysics, Geosystems* 8.8. ISSN: 15252027. DOI: 10.1029/2007GC001597 (cit. on p. 88).

Blankenbach, B. et al. (1989). "A benchmark comparison for mantle convection codes". In: *Geophysical Journal International* 98.1, pp. 23–38. ISSN: 0956540X. DOI: 10.1111/j.1365-246X.1989.tb05511.x (cit. on p. 95).

Bonito, A, J L Guermond, and B Popov (2014). "Stability Analysis of Explicit Entropy Viscosity Methods for Non-Linear Scalar Conservation Equations". In: *Mathematics of Computation* 83.287, pp. 1039–1062. ISSN: 0025-5718. DOI: 10.1090/S0025-5718-2013-02771-8 (cit. on p. 94).

Borzì, a. and V. Schulz (2012). *Computational Optimization of Systems Governed by Partial Differential Equations*, p. 296. ISBN: 9781611972054. DOI: 10.1137/1.9781611972054 (cit. on p. 100).

Bower, Dan J., Michael Gurnis, and Nicolas Flament (2015). "Assimilating lithosphere and slab history in 4-D Earth models". In: *Physics of the Earth and Planetary Interiors* 238, pp. 8–22. ISSN: 00319201. DOI: 10.1016/j.pepi.2014.10.013 (cit. on pp. 88, 113).

Brooks, Alexander N. and Thomas J R Hughes (1982). "Streamline upwind/Petrov-Galerkin formulations for convection dominated flows with particular emphasis on the incompressible Navier-Stokes equations". In: *Computer Methods in Applied Mechanics and Engineering* 32.1-3, pp. 199–259. ISSN: 00457825. DOI: 10.1016/0045-7825(82)90071-8 (cit. on p. 93).

Bunge, Hans Peter, C. R. Hagelberg, and B. J. Travis (2003). "Mantle circulation models with variational data assimilation: Inferring past mantle flow and structure from plate motion histories and seismic tomography". In: *Geophysical Journal International* 152.2, pp. 280–301. ISSN: 0956540X. DOI: 10.1046/j.1365-246X.2003.01823.x (cit. on pp. 88, 89).

Bunge, Hans-peter et al. (2009). "Time Scales and Heterogeneous Structure in Geodynamic Earth Models Time Scales and Heterogeneous Structure in Geodynamic Earth Models". In: *Science* 91.1998, pp. 91–95. ISSN: 00368075. DOI: 10.1126/science.280.5360.91 (cit. on p. 88).

Burkett, Erin R. and Magali I. Billen (2009). "Dynamics and implications of slab detachment due to ridge-trench collision". In: *Journal of Geophysical Research: Solid Earth* 114.12, B12402. ISSN: 21699356. DOI: 10.1029/2009JB006402 (cit. on pp. 88, 108, 113).

Burstedde, Carsten, Lucas C. Wilcox, and Omar Ghattas (2011). "p4est : Scalable Algorithms for Parallel Adaptive Mesh Refinement on Forests of Octrees". In: *SIAM Journal on Scientific Computing* 33.3, pp. 1103–1133. ISSN: 1064-8275. DOI: 10.1137/100791634 (cit. on p. 92).

Burstedde, Carsten et al. (2013). "Large-scale adaptive mantle convection simulation". In: *Geophysical Journal International* 192.3, pp. 889–906. ISSN: 0956540X. DOI: 10.1093/gji/ggs070 (cit. on p. 92).

Davies, Geoffrey F. (1999). *Dynamic Earth: Plates, Plumes and Mantle Convection*. Cambridge University Press, p. 472. ISBN: 9780521599337. DOI: 10.1785/gssrl.71.5.596 (cit. on p. 87).

Garel, F. et al. (2014). "Interaction of subducted slabs with the mantle transition-zone: A regime diagram from 2-D thermo-mechanical models with a mobile trench and an overriding plate". In: *Geochemistry, Geophysics, Geosystems* 15.5, pp. 1739–1765. ISSN: 15252027. DOI: 10.1002/2014GC005257 (cit. on pp. 88, 89).

Gerya, Taras (2011). "Future directions in subduction modeling". In: *Journal of Geodynamics* 52.5, pp. 344–378. ISSN: 02643707. DOI: 10.1016/j.jog.2011.06.005 (cit. on pp. 88, 108).

Giles, Michael B. and Niles A. Pierce (2000). "An introduction to the adjoint approach to design". In: *Flow, Turbulence and Combustion* 65.3-4, pp. 393–415. ISSN: 13866184. DOI: 10.1023/A:1011430410075 (cit. on p. 96).

Horbach, André, Hans Peter Bunge, and Jens Oeser (2014). "The adjoint method in geodynamics: derivation from a general operator formulation and application to the initial condition problem in a high resolution mantle circulation model". In: *GEM - International Journal on Geomathematics* 5.2, pp. 163–194. ISSN: 18692680. DOI: 10.1007/s13137-014-0061-5 (cit. on pp. 88, 89, 98, 111).

Hughes (1987). *The finite element method: linear static and dynamic finite element analysis*. Courier Corporation. ISBN: 013317025X,9780133170252 (cit. on p. 93).

Ismail-Zadeh, Alik et al. (2004). “Inverse problem of thermal convection: Numerical approach and application to mantle plume restoration”. In: *Physics of the Earth and Planetary Interiors* 145.1-4, pp. 99–114. ISSN: 00319201. DOI: 10.1016/j.pepi.2004.03.006 (cit. on p. 113).

Kronbichler, Martin, Timo Heister, and Wolfgang Bangerth (2012). “High accuracy mantle convection simulation through modern numerical methods”. In: *Geophysical Journal International* 191.1, pp. 12–29. ISSN: 0956540X. DOI: 10.1111/j.1365-246X.2012.05609.x (cit. on pp. 92, 93).

Lenardic, A., L.-N. Moresi, and H. Muhlhaus (2003). “Longevity and stability of cratonic lithosphere: Insights from numerical simulations of coupled mantle convection and continental tectonics”. In: *Journal of Geophysical Research* 108.B6, pp. 1–15. ISSN: 0148-0227. DOI: 10.1029/2002JB001859 (cit. on p. 88).

Liu, Lijun and Michael Gurnis (2008). “Simultaneous inversion of mantle properties and initial conditions using an adjoint of mantle convection”. In: *Journal of Geophysical Research: Solid Earth* 113.8, pp. 1–17. ISSN: 21699356. DOI: 10.1029/2007JB005594 (cit. on pp. 89, 113).

Liu, Lijun, Sonja Spasojevic, and Michael Gurnis (2008). “Reconstructing Farallon plate subduction beneath North America back to the Late Cretaceous.” In: *Science (New York, N.Y.)* 322.5903, pp. 934–938. ISSN: 0036-8075. DOI: 10.1126/science.1162921 (cit. on p. 88).

Mckenzie, D. P., J. M. Roberts, and N. O. Weiss (1974). “Convection in the earth’s mantle: towards a numerical simulation”. In: *Journal of Fluid Mechanics* 62, p. 465. ISSN: 0022-1120. DOI: 10.1017/S0022112074000784 (cit. on p. 88).

Moresi, L, M Gurnis, and S J Zhong (2000). “Plate tectonics and convection in the Earth’s mantle: Toward a numerical simulation”. In: *Computing in Science & Engineering* 2.3, pp. 22–33. ISSN: 15219615. DOI: 10.1109/5992.841793 (cit. on p. 92).

Moucha, R and A M Forte (2011). “Changes in African topography driven by mantle convection”. In: *Nature Geoscience* 4.10, pp. 707–712. ISSN: 1752-0894. DOI: 10.1038/ngeo1235 (cit. on p. 88).

Moucha, R. et al. (2007). “Lateral variations in mantle rheology: Implications for convection related surface observables and inferred viscosity models”. In: *Geophysical Journal International* 169.1, pp. 113–135. ISSN: 0956540X. DOI: 10.1111/j.1365-246X.2006.03225.x (cit. on p. 88).

Nocedal, J. and S. Wright (2006). *Numerical Optimization*, XXII, 664 s. 85 illus. ISBN: 0387303030. DOI: 10.1007/978-3-540-35447-5 (cit. on p. 100).

Ranalli, Giorgio and S.-I. Karato (1995). *Rheology of the Earth*. Vol. 269. 3-4. Springer Science & Business Media, p. 413. ISBN: 0412546701. DOI: 10.1016/S0040-1951(96)00042-X (cit. on p. 91).

Ratnaswamy, V., G. Stadler, and M. Gurnis (2015). "Adjoint-based estimation of plate coupling in a non-linear mantle flow model: theory and examples". In: *Geophysical Journal International* 202.2, pp. 768–786. ISSN: 0956-540X. DOI: 10.1093/gji/ggv166 (cit. on pp. 89, 99, 104, 108, 111, 113).

Seton, M. et al. (2012). "Global continental and ocean basin reconstructions since 200Ma". In: *Earth-Science Reviews* 113.3-4, pp. 212–270. ISSN: 00128252. DOI: 10.1016/j.earscirev.2012.03.002 (cit. on p. 88).

Spasojevic, Sonja, Lijun Liu, and Michael Gurnis (2009). "Adjoint models of mantle convection with seismic, plate motion, and stratigraphic constraints: North America since the Late Cretaceous". In: *Geochemistry, Geophysics, Geosystems* 10.5. ISSN: 15252027. DOI: 10.1029/2008GC002345 (cit. on pp. 88, 89).

Stadler, Georg et al. (2010). "The dynamics of plate tectonics and mantle flow: from local to global scales." In: *Science (New York, N.Y.)* 329.5995, pp. 1033–1038. ISSN: 1095-9203. DOI: 10.1126/science.1191223 (cit. on pp. 88, 108).

Travis, B. J. et al. (1990). "A benchmark comparison of numerical methods for infinite Prandtl number thermal convection in two-dimensional Cartesian geometry". In: *Geophysical & Astrophysical Fluid Dynamics* 55, pp. 137–160. ISSN: 0309-1929. DOI: 10.1080/03091929008204111 (cit. on p. 95).

Worthen, Jennifer et al. (2014). "Towards adjoint-based inversion for rheological parameters in nonlinear viscous mantle flow". In: *Physics of the Earth and Planetary Interiors* 234, pp. 23–34. ISSN: 00319201. DOI: 10.1016/j.pepi.2014.06.006 (cit. on pp. 89, 104).

Yang, Ting and Michael Gurnis (2016). "Dynamic topography, gravity and the role of lateral viscosity variations from inversion of global mantle flow". In: *Geophysical Journal International* submitted, pp. 1–51 (cit. on p. 88).

Zhong, S and M Gurnis (1995a). "Mantle convection with plates and mobile, faulted plate margins." In: *Science* 267.5199, pp. 838–843. ISSN: 0036-8075. DOI: 10.1126/science.267.5199.838 (cit. on p. 108).

Zhong, Shjjie and Michael Gurnis (1995b). "Towards a realistic simulation of plate margins in mantle convection". In: *Geophysical Research Letters* 22.8, pp. 981–984. ISSN: 00948276. DOI: 10.1029/95GL00782 (cit. on p. 89).